

Newly Evaluated Neutron Reaction Data on Chromium Isotopes

G.P.A. Nobre,^{1,*} M.T. Pigni,² D.A. Brown,¹ R. Capote,³ A. Trkov,⁴ K.H. Guber,²
R. Arcilla,¹ J. Gutierrez,⁵ A. Cuadra,^{1,6} G. Arbanas,² B. Kos,⁴ D. Bernard,⁷ and P. Leconte⁷

¹*National Nuclear Data Center, Brookhaven National Laboratory, Upton, NY 11973, USA*

²*Oak Ridge National Laboratory, Oak Ridge, TN 37831, USA*

³*NAPC–Nuclear Data Section, International Atomic Energy Agency, A-1040 Vienna, Austria*

⁴*Jozef Stefan Institute, Jamova 39, 1000 Ljubljana, Slovenia*

⁵*Gonzaga University, Spokane, WA, USA*

⁶*Nuclear Systems & Structural Analysis Group, Brookhaven National Laboratory, Upton, NY 11973, USA*

⁷*CEA/DEN/CAD/DER/SPRC/Laboratoire d'Études de Physique Centre de Cadarache,
Bâtiment 230, F-13108 Saint-Paul-Lez-Durance, France*

(Dated: August 8, 2024)

Neutron reaction data for the set of major chromium isotopes were reevaluated from the thermal energy range up to 20 MeV. In the low energy region, updates to the thermal values together with an improved R -matrix analysis of the resonance parameters characterizing the cluster of large s -wave resonances for $^{50,53}\text{Cr}$ isotopes were performed. In the intermediate and high energy range up to 20 MeV, the evaluation methodology used statistical nuclear reaction models implemented in the EMPIRE code within the Hauser-Feshbach framework to evaluate the reaction cross sections and angular distributions. Exceptionally, experimental data were used to evaluate relevant cross sections above the resonance region up to 5 MeV in the major ^{52}Cr isotope. Evaluations were benchmarked with Monte Carlo simulations of a small suite of critical assemblies highly sensitive to Chromium data, and with the Oktavian shielding benchmark to judge deep penetration performance with a 14-MeV D-T neutron source. A significant improvement in performance is demonstrated compared to existing evaluations.

CONTENTS

I. Introduction	2	2. Elastic Cross Sections	21
II. Resolved Resonance Region	4	3. Inelastic Cross Sections	21
A. Background	4	4. Capture Cross Sections	22
B. Estimation of Multiple-Scattering Corrections	5	5. $(n, 2n)$ Cross Sections	22
1. Finite size and infinite-slab approximation	5	6. (n, p) Cross Sections	22
2. Experimental corrections estimated by the MCNP	6	B. Elastic and Inelastic Angular Distributions	24
C. Results	7	C. Energy Spectra	25
D. Direct-Semidirect (DSD) neutron capture cross sections	10	D. Double Differential Cross Sections	25
E. Angular distributions in the RRR	12	1. Neutron Double-Differential Spectra	27
III. Experimental Constraints on Fast-region Fluctuations	14	2. γ Spectra	28
IV. Evaluated Results in the Fast Range	19	V. Validation	29
A. Cross Sections	19	A. Criticality Benchmarks	29
1. Total Cross Sections	19	B. D-T Neutron Leakage Experiments	30
		C. CEA Pile-oscillation Experiments in MINERVE Reactor	31
		VI. Conclusions and Recommendations	34
		Acknowledgments	35
		References	35

* Corresponding author: gnobre@bnl.gov

I. INTRODUCTION

Chromium is a tarnish-resistant metal with a high melting point commonly alloyed with iron and other materials to produce stainless steel. In nuclear fission and fusion applications, the need to increase thermal efficiency led to the development of martensitic steels that, containing small amounts of Cr (10-16%) and Mo (<1%), are characterized by an excellent resistance to thermal stresses [1]. Tempered martensite gives steel good hardness and high toughness. Chromium has also been recently proposed as a coating on zircaloy to improve the oxidation resistance of the cladding, and as dopant in UO_2 to improve the fuel's corrosion and fragmentation characteristics [2].

Naturally occurring chromium $^{\text{nat}}\text{Cr}$ consists of three stable isotopes $^{52,53,54}\text{Cr}$ plus an extremely long-lived isotope ^{50}Cr (half-life $>1.8 \times 10^{17}$ y). Having proton number $Z=24$, these isotopes are very close to the $N=28$ neutron shell closure, the major isotope ^{52}Cr being “magic”, with $N=28$ exactly. Therefore, like other nuclei in the same mass region, chromium isotopes have very low level densities and a propensity for low-lying unnatural parity states. The low level density manifests itself as non-statistical fluctuations of neutron cross sections at low energies, enhancing the role of the neutron capture by the first resonance levels of the odd isotopes [3] but also causing the resonance fluctuations to extend to higher energies ($\gtrsim 1$ MeV), well into the energy range typical of fission neutron spectra. As expected, these fluctuations can be impactful on the neutron flux in many applications and also affect the neutron leakage.

The evaluated data for the chromium isotopes released in the ENDF/B-VIII.0 library followed recent measurements [4] and evaluation efforts [5] in support of the U.S. Department of Energy (DOE) Nuclear Criticality Safety Program (NCSP) with particular focus in the resolved resonance region. In the intermediate and high energy region, although the recent work by Pereslvtsev [6] is currently included in the JEFF-3.3 library [7], ENDF/B-VIII.0 library [8] still relies on the work performed in 1997 by Chiba and released in the ENDF/B-VI.1 library [9, 10], which was extended to 200 MeV. The current evaluation is limited to 20 MeV. Besides the dated and somewhat limited evaluation work on the chromium isotopes, the most evident problem common to all released nuclear data libraries is related to the poor description of the cluster of large s -wave resonances that primarily characterize the neutron capture on the ^{53}Cr isotope, which dominates the neutron capture on natural chromium near 5 keV of the neutron incident energy.

A special set of criticality experiments (k_∞), highly sensitive to structural materials, was carried out at IPPE (Institute of Physics and Power Engineering), Obninsk, Russia and are designed as KBR assemblies. Those experiments were testing zirconium, molybdenum, chromium, and stainless steel in fast neu-

tron flux assemblies driven by highly enriched uranium (HEU). Large discrepancies of several percent (1 % is equal to 1000 pcm) between calculated and measured reactivity were found when the ENDF/B-VII.1 (or ENDF/B-VIII.0) library was used. The largest disagreement of 11 % in the most chromium-sensitive experiment, KBR-15, (HEU-MET INTER-015 in ICBESP notation [11]) was traced to heavily underestimated neutron capture on natural chromium in the keV region [12]. Those authors attempted to address the issue [12] within the BROND-3.1 library [13] by fitting the $^{53}\text{Cr}(n, \gamma)$ cross sections published by Guber [4] at the NDST 2010 conference. The digitized capture yield data in EXFOR were interpreted as cross section data, therefore, neglecting important corrections such as multiple scattering and self-shielding effects, which may reach 80% in the keV region. Data were fitted by adjusting the bound resonance levels and the widths of a few low-lying resonances but, in doing that, the value of the measured thermal capture cross section was greatly overestimated. Despite the incorrect interpretation of the measured capture yield as cross sections, the BROND-3.1 evaluation showed a significantly improved performance for the KBR cases, particularly due to the large increase of capture cross sections in the energy region of the cluster of s -wave resonances between 1–10 keV. However, this improvement in integral performance could not be understood because the digitized data taken from [4] were, later on, found to be affected by a mistake in calculating the density of the Cr_2O_3 sample used in the measurement. In fact, after the correction of Guber *et al.*, the $^{53}\text{Cr}(n, \gamma)$ capture yield available in the EXFOR library (EXFOR subentry 14324006) is decreased by a factor of two with respect to the data published in Ref. [4]. Unfortunately, these corrected Guber *et al.* data are very discrepant from earlier comprehensive Stieglitz *et al.* measurements on enriched chromium isotopes undertaken at RPI in the 1970's and reported in the EXFOR library, especially regarding the normalization. Reasons for such differences are still not understood.

Although there are differences in the enrichment and geometry of the oxide sample between the experiments of Stieglitz *et al.* and Guber *et al.*, these are not sufficient to explain the large discrepancies of the reported $^{53}\text{Cr}(n, \gamma)$ cross sections as shown in Fig. 1. Here, the cross sections reconstructed from ENDF/B-VIII.0 resonance parameters and including multiple-scattering and self-shielding corrections based on the experimental configuration of Guber *et al.*, *i.e.*, thickness, isotopic abundances, and sample geometry, are also shown in blue for the finite size case and in yellow for the infinite-slab approximation case. Differently from the infinite slab approximation, when finite-sized corrections are included, the geometric properties of the sample are used to calculate the multiple scattering corrections. Quantities such as the estimated mean-free-path for a given incident neutron energy or Monte Carlo simulations for given sample properties can be used as independent ways to determine the accuracy of the multiple scattering corrections cal-

culated in the finite or infinite approximation. It is also visible in Fig. 1, in the energy below 2.5 keV, resonance-like data points in the of Stieglitz *et al.* that are not visible in the data of Guber *et al.* This discrepancy was not investigated in the present work.

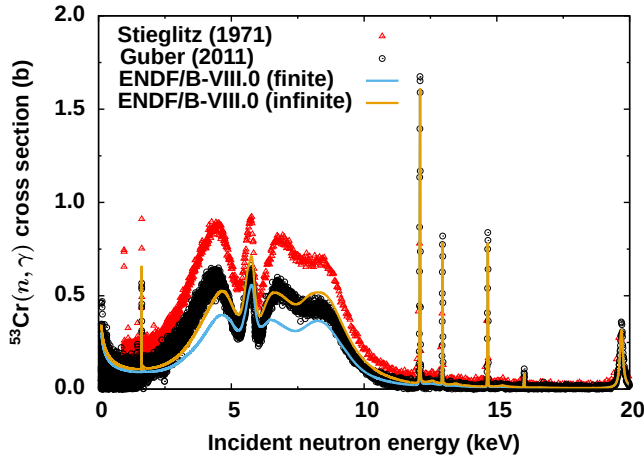


FIG. 1. (color online) $^{53}\text{Cr}(n, \gamma)$ cross sections from Guber *et al.* [4] and Stieglitz *et al.* [14] as reported in the EXFOR library and (in blue and yellow solid lines) the cross sections reconstructed from ENDF/B-VIII.0 resonance parameters including multiple-scattering and self-shielding corrections based on the experimental configuration of Guber *et al.*

The present work is an attempt to, first, resolve the discrepancy between the measured capture data, second, understand the large discrepancy in quantifying multiple scattering corrections in finite and infinite approximation and, finally, derive a consistent set of resonance parameters (energy, capture, and neutron widths) based on a fitting procedure including appropriate experimental corrections. The ultimate goal is to improve the agreement with the KBR integral test cases and other criticality and shielding experiments highly-sensitive to chromium.

At higher energies, the ^{52}Cr total cross section from ENDF/B-VIII.0 is larger than Carlton *et al.* data in EXFOR 13840002 subentry [15] above 4 MeV. However, Carlton data are discrepant in normalization¹ with all other datasets in the energy region from ~ 5 up to 10 MeV as shown in Fig. 2. Higher-energy fluctuations extend up to around 10 MeV in the total and may extend up to 5 MeV in elastic and inelastic cross sections, angular distributions, and partial gamma production cross sections. Those fluctuations have to be considered in the evaluations at least up to 6 MeV based on measured data. Additionally, Hauser-Feshbach calculations have to agree with averaged cross-section data. Finally we note that the angular distributions in all Cr isotopes are a copy

¹ Carlton data also show a discontinuity around 4 MeV as discussed in Sec. III.

of the ENDF/B-V ^{nat}Cr angular distribution [16], which were fitted to available experimental data.

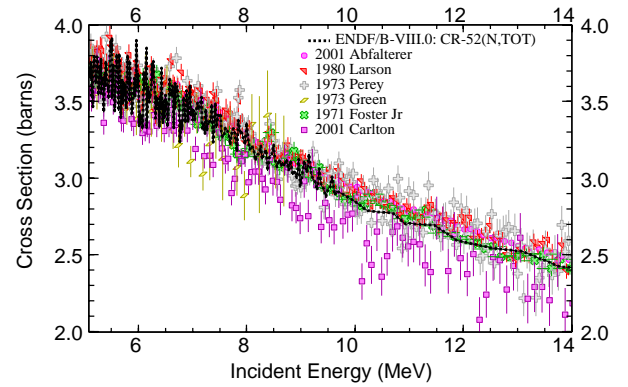


FIG. 2. (color online) Normalization problems in ^{52}Cr total cross section data by Carlton *et al.* data [15]. The other datasets are taken from EXFOR.

As mentioned above, just as chromium can mask problems with iron, iron can also mask problems with chromium. It behooves us to understand (and address) the shortcomings in iron. We first note the biggest ^{56}Fe shortcoming, already noted in the CIELO iron paper [17]: the evaluated inelastic cross section based on available experimental data is too high, leading to an elastic scattering cross section that is too low. This causes the fast neutron leakage spectrum from 2 up to 10 MeV to be too low in the integral testing used for CIELO. A recent experiment by Pirovano *et al.* [18] further supports this observation. Next we note that deep penetration (leakage) experiments indicate that the cross-section “valleys” in between resonances are too low and that direct capture needs to be included in the evaluation [17]. Revising the direct capture may also help resolve the discrepancy with Firestone *et al.*’s evaluation of the thermal capture cross section [19]. Finally we note that at high energies (> 40 MeV) shielding experiments reported by Konno *et al.* indicate that further corrections are needed [20, 21].

Despite chromium’s ubiquity in steel alloys, there is only one integral criticality test that we are aware of that explicitly targets chromium: the KBR-15 assembly discussed above. There are of course several other criticality tests with high stainless steel content and a sizable sensitivity to chromium including the PUMET-INT-002 test noted in the iron CIELO paper [17]. CEA/DEN/CAD/DER/SPRC/Laboratoire d’Études de Physique in Cadarache, France also included the study of chromium within their comprehensive experimental program on structural, moderating, and absorbing materials entitled MAESTRO [22], particularly in MAESTRO phase III (2013/14). The MAESTRO programme relies on pile-oscillation measurements in the MINERVE reactor and a very careful modeling of the experimental setup allowing for benchmark quality of derived results.

The organization of this paper is as follows. First we

describe improvements to the resonance evaluations in all of the chromium isotopes. Following this, we detail the determination of the total cross section and validation of the optical model used in the evaluation. With this in hand, we turn to the main business of evaluating the fast regions of the chromium isotopes. This discussion will include a careful consideration of the level densities involved and the detailed tuning of the Hauser-Feshbach calculations to experimental data. A comprehensive comparison of available experimental data including cross sections, angular distributions, neutron and gamma emission spectra, and double differential cross sections are presented. We conclude with a discussion of the validation of the evaluations using both criticality and shielding benchmarks, as well as pile-oscillation measurements in the MINERVE reactor.

II. RESOLVED RESONANCE REGION

A. Background

In the low-energy neutron range from a few keVs up to a few tens of keV, structural materials such as chromium and vanadium are characterized by clusters of s -wave resonances with large neutron and capture widths. Due to the finite size of sample thickness used in capture yield measurements, the measured cluster of s -wave resonances is associated with strong multiple scattering interactions as well as self-shielding and neutron sensitivity effects. In the specific case of $^{53}\text{Cr}(n, \gamma)$, the four energy levels between 4 and 10 keV are clearly an example for which the multiple-scattering interaction of the incident neutrons has the effect of greatly enhancing the number of measured counts. Although the self-shielding effects tend to reduce the measured counts, the overall result is that the observed capture widths are largely overestimated. Therefore, to properly evaluate the resonance capture widths for these levels, it is of fundamental importance to account for these experimental effects in the fitting evaluation procedure. Most often used in the fit of measured capture yield data, methods of calculation to correct the theoretical cross sections or yield for both self-shielding and multiple scattering effects are implemented in the R -matrix code SAMMY. Other input options of the code are the geometric characteristic of the sample such as thickness, given in atom/barn (a/b) or in cm, and its height, given in cm, as well as the type of normalization of the fitted data. The latter represents another important point of discussion in the fitting procedure of the measured capture data aimed to derive the resonance parameters such as energies and related widths. In this regard, the measured capture cross sections (in barns) are often reported in literature as the neutron capture yield (a dimensionless quantity) multiplied by the inverse of the sample thickness. This type of normalization can be understood by the relationship between the (self-shielded) neutron cap-

ture yield and the total and capture cross section,

$$Y = (1 - e^{-n\sigma_t}) \frac{\sigma_\gamma}{\sigma_t} \approx n \sigma_\gamma, \quad (1)$$

in the limit the sample thickness n is very thin such as the quantity $n\sigma_t \ll 1$. Under this assumption, the capture cross sections are determined in shape by the measured energy-dependent neutron yield data and in magnitude by the sample thickness. However, for the measured $^{53}\text{Cr}(n, \gamma)$ cross sections, the thickness normalization as reported by Stieglitz [14] and Guber [4] seems to be the incorrect choice. In fact, a simple comparison of the capture cross sections normalized by the constant value $1/n$ and by the shape normalization $\sigma_t(1 - e^{-n\sigma_t})^{-1}$ defined by the energy dependent total cross section as well as the thickness, shows remarkable differences as displayed in Figs. 3–4. This can be explained by the fact, although the thickness for both experiments is relatively thin, the ^{53}Cr total cross sections are such that the condition $n\sigma_t \ll 1$ is not met. For this reason, the $^{53}\text{Cr}(n, \gamma)$ cross sections from Stieglitz *et al.* and Guber *et al.* were not used in the fitting procedure. Instead, the related neutron capture yields were used and the set of resonance parameters was derived by the simultaneous fit of the neutron capture yields and transmission data in the same energy range.

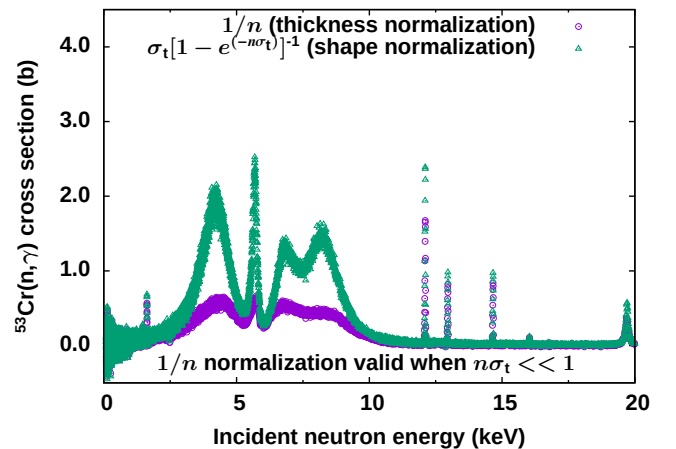


FIG. 3. (color online) $^{53}\text{Cr}(n, \gamma)$ cross sections from Guber *et al.* [4] obtained by normalizing the neutron capture yield Y by the inverse of the sample thickness (in purple) and a shape normalization (in green).

In addition to the normalization of the capture cross sections, another relevant point of discussion is the discrepancy between measured data from Stieglitz *et al.* and Guber *et al.* as clearly shown in Figs. 3–4. With a slight deviation in shape below 1 keV, the two measured capture yield data sets differ by a constant value of about 50% in the energy region of the cluster of s -wave resonances between 1–10 keV. Although a re-analysis of the thickness value of data from Guber *et al.* showed the reported value of the thickness, $n=0.0137$ a/b, should be reduced

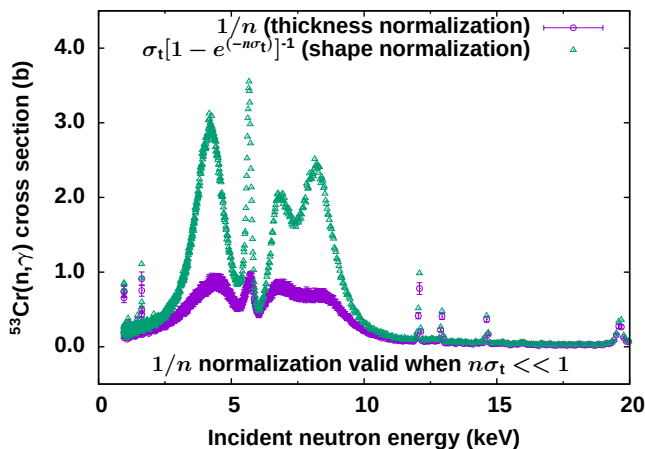


FIG. 4. (color online) $^{53}\text{Cr}(n, \gamma)$ cross sections from Stieglitz *et al.* [14] obtained by normalizing the neutron capture yield Y by the inverse of the sample thickness (in purple) and a shape normalization (in green).

by 3%, for an updated value of $n=0.0133$ a/b, there is no clear explanation of the large difference between the two data sets. An indirect proof that ^{53}Cr yield data from Stieglitz *et al.* are correct is their consistency with capture yield data measured for a natural sample. The capture widths obtained by the fit of the natural yield data consistently reproduced the yield data from Stieglitz *et al.* for the enriched ^{53}Cr sample. Moreover, mainly due to the large capture width of the resonance level at 4.1 keV, it is clear that, although the cluster of s -wave resonances is in the keV region, its contribution to the evaluation of the capture cross sections in thermal energy range is not negligible.

In the next subsection the results of the evaluation procedure of the two isotopes $^{50,53}\text{Cr}$ will be discussed in details.

B. Estimation of Multiple-Scattering Corrections

1. Finite size and infinite-slab approximation

In addition to intrinsic properties of the sample (density and weight), the sample's geometric configuration (thickness, height or radius) in relation to the beam size plays an important role in the quantification of the multiple scattering corrections. In fact, the use of either the finite size sample or infinite-slab approximation can lead to large differences in the calculated neutron capture yield as shown in Figs 5–7. These discrepancies can be more or less remarkable depending on the experimental configuration of the sample. In Fig. 5 the discrepancy for the measurement on the metal natural sample is of the order of 15% differently from the other two measurements for oxide enriched sample shown in Figs 6–7 for which the

discrepancy is about 30%. As expected, the impact of the finite size or infinite slab approximation on the metal natural sample calculations is relatively small compared to the oxide cases since its a thinner sample configuration. Another way to calculate the neutron capture yield

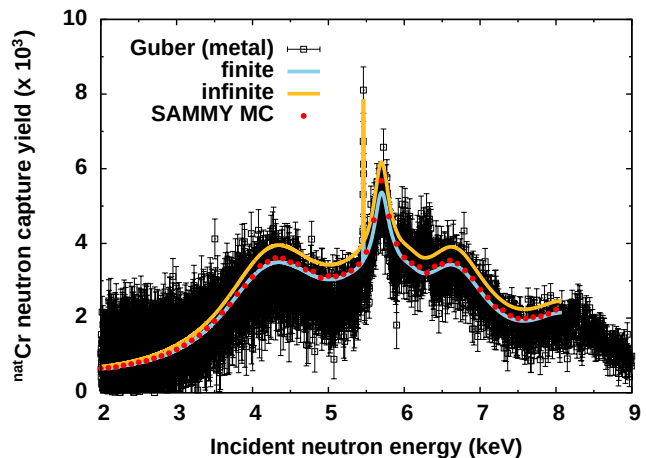


FIG. 5. (color online) $^{\text{nat}}\text{Cr}$ neutron capture yield calculated for a finite size sample (in light blue) and in infinite-slab approximation (in yellow) compared to Monte Carlo simulations (in red) performed by SAMMY. The calculations used the sample configuration of the metal natural sample of Guber *et al.*

is to perform Monte Carlo simulations including the same experimental configurations for a defined set of resonance parameters. Plotted in red dots, these simulations agree nicely with the finite size approximation in the case of the metal natural sample as shown in Fig 5. However, for both oxide enriched samples, it is clearly difficult to determine if either the finite size sample or infinite slab approximation are the suitable option. For this reason, the data set measured on the natural metal sample was selected and used in the fit with finite size sample option. The sample characteristic used in the Monte Carlo simulations are reported in Table I in which the beam size is assumed for all measurements equals to the size of the sample. Due to edge effects this parameter can have a big impact on the Monte Carlo calculations. Moreover, the plotted yields calculated in finite size or infinite slab approximation as well as the Monte Carlo simulations were performed by using the set of resonance parameters obtained from the fit of the natural data as shown in Fig. 5. The comparison of the calculated yields with measured data from Guber *et al.* and Stieglitz *et al.* displayed in Figs 6–7, respectively, shows that the magnitude of data from Stieglitz *et al.* is definitely more consistent with the measurements on the metal sample. Although additional investigation on the agreement between Monte Carlo and analytical calculations for the multiple scattering corrections is needed, this analysis suggests that enriched data measured on oxide sample by Guber *et al.* are affected by a normalization issue.

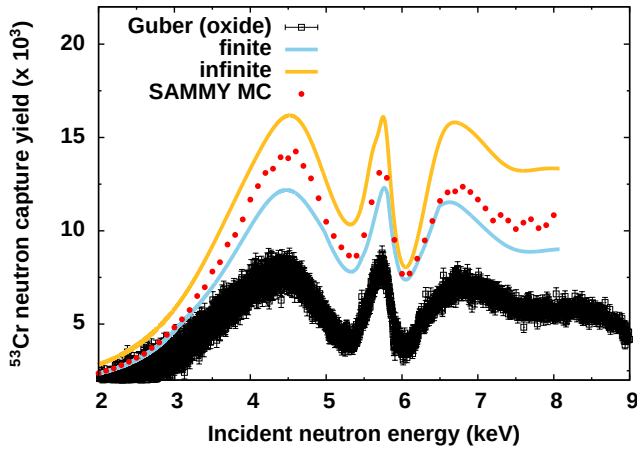


FIG. 6. (color online) ^{53}Cr neutron capture yield calculated for a finite size sample (in light blue) and in infinite-slab approximation (in yellow) compared to Monte Carlo simulations (in red) performed by SAMMY. The calculations used the sample configuration of the oxide enriched sample from Guber *et al.*

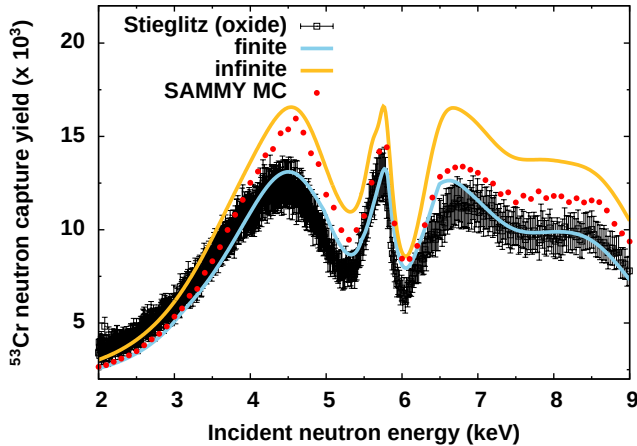


FIG. 7. (color online) ^{53}Cr neutron capture yield calculated for a finite size sample (in light blue) and in infinite-slab approximation (in yellow) compared to Monte Carlo simulations (in red) performed by SAMMY. The calculations used the sample configuration of the oxide enriched sample from Stieglitz *et al.*

Similarly to the oxide configurations related to the ^{53}Cr isotope, Figure 8 shows the Monte Carlo simulations for the ^{50}Cr , which are found in the middle of the finite size and infinite slab approximation calculations. Since the thickness is slightly thinner than the ^{53}Cr oxide sample, the Monte Carlo results tend to be close to the infinite slab approximation. The fit for this set of data was performed with finite size approximation and, for future updates, the plan is, first, to resolve the discrepancy between Monte Carlo simulations and the analytical treat-

TABLE I. $^{50,53}\text{Cr}$ sample characteristics for both natural metal and oxide enriched samples used in the calculations and Monte Carlo simulations.

Sample	Thickness a/b	Radius cm	Beam height cm
^{50}Cr [14]	0.0088	0.914	3.17
$^{\text{nat}}\text{Cr}$ [4]	0.0263	0.318	1.27
^{53}Cr [4]	0.0133	0.978	2.03 ^(a)
^{53}Cr [14]	0.0142	1.234	3.17

(^a) This is the effective radius calculated from the area $A = 2 \times 6.844 \text{ cm}^2$ of the $2.54 \times 5.08 \text{ cm}$ (or 1×2 inches) rectangular sample formed by two 1-inch square samples placed one over the other.

ment of the multiple scattering corrections, and second, to derive the proper set of parameters.

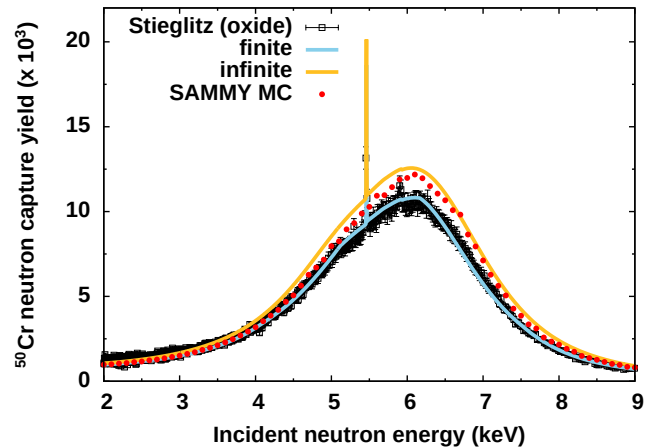


FIG. 8. (color online) ^{50}Cr neutron capture yield calculated for a finite size sample (in light blue) and in infinite-slab approximation (in yellow) compared to Monte Carlo simulations (in red) performed by SAMMY. The calculations used the sample configuration of the oxide enriched sample from Stieglitz *et al.* and scaled by a factor 0.92.

2. Experimental corrections estimated by the MCNP

Independently from the efforts to understand the Guber and Stieglitz data, simplified MCNP6.2 [23, 24] models of the ^{53}Cr capture experiments were developed to assess the multiple scattering cross sections and potentially compare MCNP and SAMMY implementations. Note that the models were not intended to fully represent the experiments or replicate their results, rather to understand the magnitude of the multiple scattering correction and its dependence on energy and sample thickness for geometries representative of both experiments. The results obtained did not appear sensitive to sam-

ple geometry other than thickness, and the discussion and results shown below focus on the results of the simplified ORELA model used in Guber et al experiment. The model included a disc-shaped uniform source sufficiently large ($r=6\text{cm}$) to fully illuminate the enriched chromium sample described in [4]. To study the dependence of the multiple scattering correction on sample thickness, the mono-energetic source neutrons were assumed to have energies uniformly distributed between 4 and 10 keV. In both cases, the neutrons were assumed to be mono-directional and perpendicular to the sample, which allowed to limit the size of the model. Note that this assumption is a good approximation of the typical experimental situation as the source of neutrons is more than 40 meters away from the sample in the closest setup. The rectangular sample size was, as described in [4], 2.54 cm by 5.08 cm long (1" by 2") with nominal thickness $t_n = 0.98$ cm. The studied thickness varied from 0.01 up to 3 cm following the estimated mean-free path of 5 keV neutrons in the chromium oxide. No attempt was made to model the C6D6 detector, rather appropriately tagged photon current tallies were implemented on various relevant surfaces.

The results are shown in Fig. 9 for different sample thicknesses. For the nominal sample thickness, the multiple scattering correction, defined as the number of photons having undergone more than one collision (including the collisions of the photon's parent neutron), divided by the total number of photons, is 69%; for thicker samples, the multiple scattering correction can reach up to 80%; as expected, the correction asymptotically approaches 0 for extremely thin samples (for 0.01 cm, the correction is 2%). It should be noted that the narrow uncertainty bars shown on the plot correspond to the statistical uncertainty only, and do not account for other sources of systematic uncertainties in the estimation of the effect of multiple scattering, such as the inclusion of non-capture photons, background, etc. Those effects, however, are expected to be orders of magnitude lower than the multiple scattering and capture phenomena under study. The energy dependence of the correction is shown in Fig. 10 (blue line). The correction exhibits peaks at energies slightly shifted to the right from the resonance energies shown in Table II, because of the interplay of the contributions shown in orange (MS correction = $100 \times (\text{Total} - \text{First}) / \text{Total}$). Note that the number of first collision photon creation events (labeled "First") only reflects the largest resonance at approximately 5.7 keV, due to the energy grid chosen for the study and the narrowness of the resonances, while the total number of photon creation events (labeled "Total") shows all four resonances, slightly shifted to higher energies, since the neutrons emitted from the source have the opportunity to downscatter into the resonances. An additional sensitivity was performed to the finite vs infinite sample approximations discussed in the previous section. As seen in Fig. 11, the multiple scattering corrections for the finite and infinite sample approximations differ basically by a normalization fac-

tor, with a stronger correction resulting for the infinite sample.

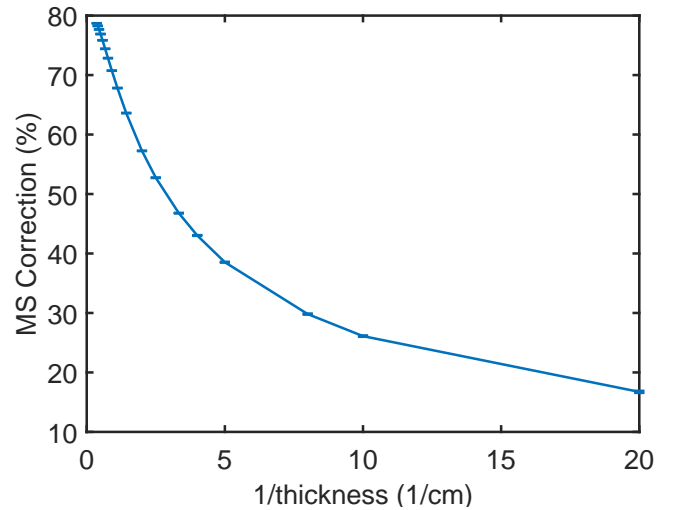


FIG. 9. (color online) Multiple scattering correction dependence on sample thickness from simplified MCNP6 model.

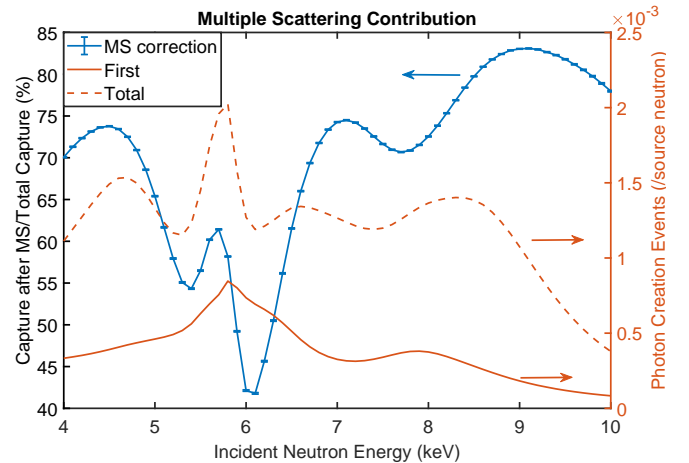


FIG. 10. (color online) Multiple scattering correction dependency on energy from simplified MCNP6 model.

C. Results

The evaluation of the total and capture cross sections of the $^{50,53}\text{Cr}$ isotopes was performed with particular focus on the cluster of s -wave resonances as well as the related thermal values in the attempt to address the inconsistencies of the measured data sets and the large discrepancies with the evaluated data reported in the ENDF/B-VIII.0 library.

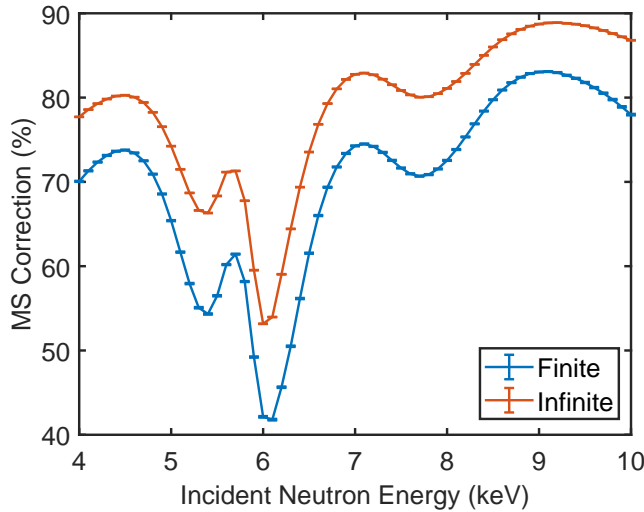


FIG. 11. (color online) Multiple scattering correction comparison, finite vs. infinite sample sensitivity.

The simultaneous fit of neutron capture yields and transmission data showed that, in addition to the large discrepancy between measured capture yield data by Stieglitz *et al.* and Guber *et al.*, as explained in section II A, there is no perfect compatibility among available transmission data in the alignment of the energy levels measured in the s -wave cluster energy region for the ^{53}Cr isotope. Although a shift in the alignment between the energy levels for transmission and capture yield data is expected because of the effect of the strong multiple scattering and self-shielding corrections in the capture yield data (clearly visible in Figs 3–4), this misalignment seems too remarked and an optimal fit between transmission and capture data could not be achieved.

Following the analysis described in II B 1, the strategy adopted in the evaluation procedure was the simultaneous fit of transmission and capture yield data measured on the natural sample performed at ORELA [4]. The capture resonance widths fitted to neutron capture yield data on natural sample indirectly inferred the proper magnitude of the $^{53}\text{Cr}(n, \gamma)$ cross sections. This was possible also because the cluster of s -wave resonances is populated only by levels of the two analyzed isotopes, $^{50,53}\text{Cr}$. On the other side, the simultaneous fit together with thin- and thick-target transmission data measured on natural sample still revealed the issue with the level misalignment most evident for the resonance energy level at 4.1 keV as shown in Figs 12–14. Here, in addition to the current evaluation (in black solid line), the yield and transmission data calculated from the resonance parameters reported in the ENDF/B-VIII.0 library are shown by light blue lines.

In the case of neutron capture yield calculations as well as the related fitting procedure, the finite size option in the SAMMY code was adopted. By using the set

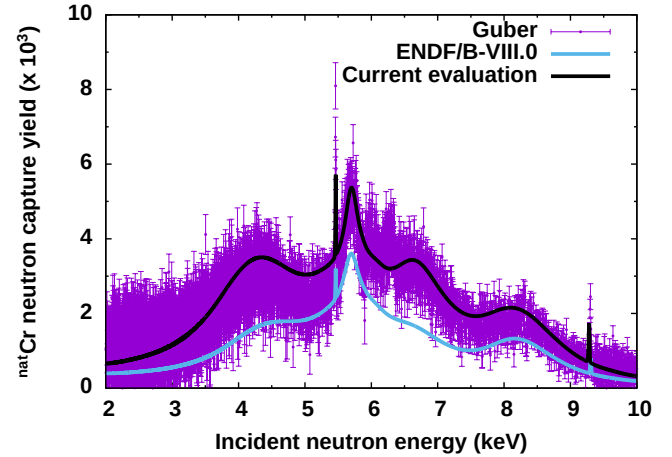


FIG. 12. (color online) Measured [4] and calculated ^{nat}Cr neutron capture yield data. The neutron capture yield shown for all cases was calculated in finite size approximation.

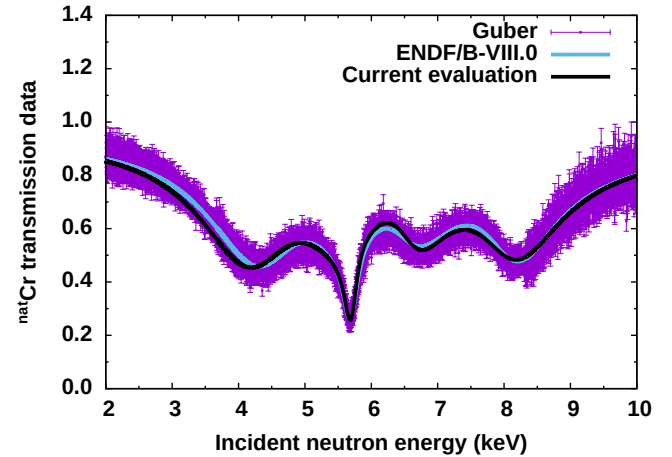


FIG. 13. (color online) Measured [4] and calculated ^{nat}Cr thin-target transmission data.

of resonance parameters fitted to the natural measured data, it could be possible to compare the calculated yield data to the measurements of Stieglitz *et al.* and Guber *et al.* performed with enriched ^{53}Cr sample. However, due to the discrepancies for both oxide sample configurations between Monte Carlo simulations and analytical approximations, the related measured data were excluded from the fit of the resonance widths.

Table II reports the $n+^{53}\text{Cr}$ energy levels and related capture and neutron widths for selected nuclear data libraries and Reich-Moore R -matrix analyses. As expected, ENDF/B-VIII.0 values of the resonance capture widths are systematically smaller than other sets. As shown in Fig.1, we can only guess these values were fitted in infinite slab approximation to data from Guber *et al.* measured on the enriched oxide sample although the

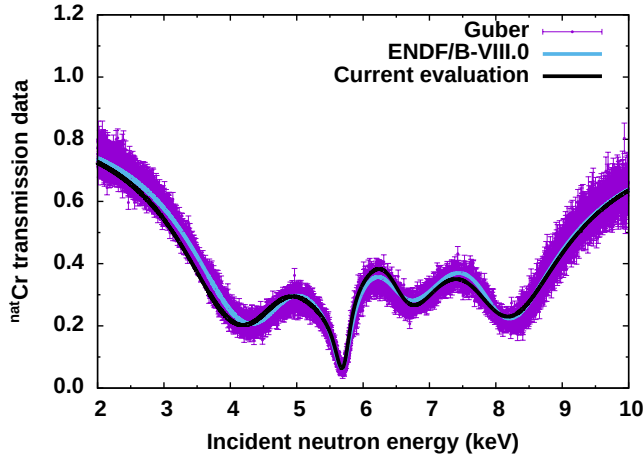


FIG. 14. (color online) Measured [4] and calculated ^{nat}Cr thick-target transmission data.

TABLE II. ^{53}Cr energy levels and related capture and neutron widths reported in selected nuclear data libraries and R -matrix analyses.

	E (keV)	Γ_γ (eV)	Γ_n (eV)
ENDF/B-VIII.0	4.25	2.07	1360
	5.67	0.62	231
	6.79	1.72	1183
	8.21	1.91	1139
Stieglitz [14]	4.18	3.23	1520
	5.67	1.23	220
	6.74	5.28	1200
	8.18	3.25	1030
Current	4.31	5.04	1408
	5.68	0.79	202
	6.78	4.14	956
	8.19	3.35	1313

agreement is not perfect. Although the interplay with the neutron widths is an important factor, capture widths from Stieglitz *et al.* are consistent with the current evaluation for the 8 keV level, however, they seem to be overestimated for the 5 and 6 keV levels. The differences between the current evaluation and the widths reported by Stieglitz *et al.* can be understood in differences in both the quantification of the multiple scattering corrections and the possible slight disagreement between oxide enriched data from Stieglitz *et al.* and metal data from Guber *et al.* as displayed in Figs. 5 and 7.

In Tabs. III– VII the thermal constant values and resonance integrals (RI) of the natural Chromium and $^{50-54}\text{Cr}$ isotopes are reported for several evaluated and measured data. As expected, the major updates are related to the $^{50,53}\text{Cr}$ isotopes. The thermal capture on natural chromium increased by 0.11 barn, a 0.3% increase driven by changes in ^{53}Cr still within the uncertainties of the Mughabghab Atlas 2017 value. However, the capture

TABLE III. ^{nat}Cr resonance region integral metrics. Atlas results marked with “exp” refer to the Mughabghab’s evaluation based on the experimental data, while Atlas values derived from calculations are marked with “calc”. “*” indicates the measurement is actually a measurement of (n,abs) which must equal (n,γ) at thermal energies.

σ_{therm} (b)	(n,tot)	(n,el)	(n,γ)
This work	6.71	3.48	3.23
ENDF/B-VIII.0 [8]	6.58	3.46	3.12
Atlas (2018) [26]		3.38 ± 0.01	3.17 ± 0.08
BROND-3.1 [13]	6.83	3.36	3.47
(1935) Dunning [27]	4.9		
(1937) Goldhaber [28]		3.6	
(1946) Coltman [29]			2.5 ± 0.05
(1950) Harris* [30]			3.05 ± 0.15
(1950) Colmer* [31]			3.1 ± 0.2
(1951) Grimeland [32]			2.88 ± 0.15
(1951) Pomerance [33]			2.83 ± 0.14
(1953) Melkonian [34]	7.3		
(1956) Prokhorov [35]			3.2 ± 0.1
(1973) Salama [36]	6.47 ± 0.33		
(1976) Kropff [37]	6.50 ± 0.14		3.25 ± 0.15

	RI (b)	(n,tot)	(n,el)	(n,γ)
This work	90.79	86.05	1.67	
ENDF/B-VIII.0 [8]	89.64	84.96	1.53	
Atlas (2018) [26]			2.1 ± 0.2	
BROND-3.1 [13]	89.65	84.85	2.02	
(1955) Macklin [38]				1.9
(1956) Prokhorov [35]				1.9 ± 0.4
(1957) Klimentov* [39]				2.6 ± 1.1
(1964) Kapchigashev [40]				1.5 ± 0.1

RI of the natural chromium increased by 9% to 1.67 b, but it is still low compared to the recommended Atlas value of 2.1 ± 0.2 barn.

Although the analysis for ^{50}Cr needs to be updated due to the multiple scattering corrections, the current analysis shows a relatively large increase in the scattering cross section and a slight decrease in the capture cross sections keeping the total thermal value almost unchanged. However, the ^{50}Cr RI increased to 7.73 b by 7% compared to the Atlas value of 7.2 b in better agreement with Kayzero data-base value [25].

The ^{53}Cr isotope features an increase of around 7% (13%) for the thermal capture cross section (RI) with respect to ENDF/B-VIII.0 library and the Atlas compilation. The values of the BROND-3.1 library [13] are clearly overestimated due to the assumption used in the fitting procedure of the capture cross sections.

TABLE IV. ^{50}Cr resonance region integral metrics. Atlas results marked with “exp” refer to the Mughabghab’s evaluation based on the experimental data, while Atlas values derived from calculations are marked with “calc”. All major libraries except JENDL-4.0 used the same ORNL RRR from Ref. [5].

σ_{therm} (b)	(n,tot)	(n,el)	(n,γ)
This work	18.06	2.85	15.21
ENDF/B-VIII.0 [8]	17.81	2.40	15.42
BROND-3.1 [13]	17.81	2.40	15.42
Atlas (2018) [26]	17.1 ± 0.4		14.7 ± 0.4
k0 (2019) [25]			15.1 ± 0.8
(1947) Seren [41]			11.0 ± 4.4
(1952) Pomerance [42]			16.3 ± 1.3
(1960) Lyon [43]			16.6 ± 1.7
(1968) Sims [44]			15.9 ± 0.1
(1975) Gleason [45]			15.8 ± 0.2
(1978) Heft [46]			16.1 ± 0.1
(1978) Koester [47]	2.41 ± 0.06		
(1984) Simonits [48]			15.2 ± 0.2
(1988) De Corte [49]			14.9 ± 0.36
(1997) Venturini [50]			14.2 ± 0.5
(2014) Arbocco [51]			14.41 ± 0.13

RI (b)	(n,tot)	(n,el)	(n,γ)
This work	273.13	261.97	7.73
ENDF/B-VIII.0 [8]	259.73	249.02	7.24
BROND-3.1 [13]	259.73	249.02	7.24
Atlas (2018) [26]			7.2 ± 0.2
k0 (2019) [25]			8 ± 2.5
(1968) Sims [44]			10.4 ± 0.4
(1971) De Corte [52]			8.3
(1972) Van Der Linden [53]			7.8 ± 0.4
(1975) Gleason [45]			9.0 ± 0.5
(1976) Sage [54]			12.5 ± 3.24
(1978) Heft [46]			10.5 ± 0.4

MACS(30 keV) (mb)	(n,γ)
This work	45.02
ENDF/B-VIII.0 [8]	38.25
JENDL-4.0 [55]	36.95
BROND-3.1 [13]	38.25
Atlas (exp) (2018) [26]	40.3 ± 4.0
Atlas (calc) (2018) [26]	37.3 ± 2.7
KADoNiS-0.3 [56]	49.0 ± 13.0
(1971) Allen [57]	31 ± 4
(1974) Beer [58], (1975) Beer [59]	50 ± 15
(1977) Kenny [60]	52 ± 13

D. Direct-Semidirect (DSD) neutron capture cross sections

Direct-semidirect (DSD) neutron capture cross sections on $^{50,52,53,54}\text{Cr}$ were computed using a single-particle direct-semidirect capture model implemented in computer code CUPIDO that was originally developed to cal-

TABLE V. ^{52}Cr resonance region integral metrics. Atlas results marked with “exp” refer to the Mughabghab’s evaluation based on the experimental data, while Atlas values derived from calculations are marked with “calc”. All major libraries used the same ORNL RRR from Ref. [5].

σ_{therm} (b)	(n,tot)	(n,el)	(n,γ)
This work	3.905	3.047	0.857
ENDF/B-VIII.0 [8]	3.905	3.047	0.857
BROND-3.1 [13]	3.687	2.926	0.761
Atlas (2018) [26]	3.64 ± 0.03	2.78 ± 0.02	0.86 ± 0.02
(1952) Pomerance [42]			0.73 ± 0.06
(1997) Venturini [50]			0.86 ± 0.03

RI (b)	(n,tot)	(n,el)	(n,γ)
This work	56.05	52.52	0.494
ENDF/B-VIII.0 [8]	56.05	52.52	0.494
BROND-3.1 [13]	55.90	52.53	0.761
Atlas (2018) [26]			0.66

MACS(30 keV) (mb)	(n,γ)
This work	7.991
ENDF/B-VIII.0 [8]	7.991
BROND-3.1 [13]	8.976
Atlas (exp) (2018) [26]	9.1 ± 2.1
Atlas (calc) (2018) [26]	9.1 ± 0.6
KADoNiS-0.3 [56]	8.8 ± 2.3
(1971) Allen [57]	3.8 ± 1.0
(1974) Beer [58], (1975) Beer [59]	8.3 ± 3.0
(1977) Kenny [60]	9.8 ± 2.3
(1989) Rohr [61]	8.79 ± 2.30

culate fluctuation effects in radiative capture in the giant dipole resonance energy region [65]. The CUPIDO code has also been used for computation of direct-semidirect capture in the thermal neutron and resolved resonance energy ranges [66], in conjunction with R-matrix nuclear data evaluations using the code SAMMY [67].

The original calculations of DSD capture used for this evaluation were performed in 2008 using then available version of CUPIDO, which did not yet have the energy dependence of the Koning-Delaroche optical model potential (OMP) parameters programmed into it. Consequently, the Koning-Delaroche OMP was first translated into a linear energy-dependent OMP (with 1 keV incident neutron energy as a reference point), and this OMP was then used as input for DSD calculations by CUPIDO. CUPIDO calculations using this OMP yielded DSD thermal neutron capture cross sections that were anomalously large. In fact, they were found to be much larger than the measured total thermal neutron capture of chromium isotopes. This anomalously large DSD capture was interpreted as a manifestation of a potential scattering divergence caused by the s -wave “resonance” effect that is inherent to single-particle potential models [68]. In

TABLE VI. ^{53}Cr resonance region integral metrics. Atlas results marked with “exp” refer to the Mughabghab’s evaluation based on the experimental data, while Atlas values derived from calculations are marked with “calc”. All major libraries used the same ORNL RRR from Ref. [5].

σ_{therm} (b)	(n,tot)	(n,el)	(n,γ)
This work	27.17	7.78	19.40
ENDF/B-VIII.0 [8]	25.94	7.82	18.11
BROND-3.1 [13]	30.51	7.82	22.69
Atlas (2018) [26]	25.9 ± 0.7	7.3 ± 0.2	18.6 ± 0.6
(1952) Pomerance [42]			17.5 ± 1.4
(1997) Venturini [50]			18.6 ± 0.6

RI (b)	(n,tot)	(n,el)	(n,γ)
This work	323.71	311.01	9.59
ENDF/B-VIII.0 [8]	317.76	305.52	8.43
BROND-3.1 [13]	319.27	304.29	11.19
Atlas (2018) [26]			8.66 ± 0.40
(1950) Harris [62]		78.	

MACS(30 keV) (mb)	(n,γ)
This work	51.73
ENDF/B-VIII.0 [8]	25.94
JENDL-4.0 [55]	26.17
BROND-3.1 [13]	48.99
Atlas (exp) (2018) [26]	54.0 ± 9.4
Atlas (calc) (2018) [26]	36.0 ± 5.0
KADoNiS-0.3 [56]	58.0 ± 10.0
(1971) Allen [57]	40 ± 5
(1974) Beer [58], (1975) Beer [59]	61 ± 24
(1977) Kenny [60]	58 ± 10

the mass range spanned by the four stable chromium isotopes, the said s -wave resonance is due to the energy of the $3s$ single-particle neutron state in the nuclear potential being nearly equal to the neutron binding energy.

These anomalously large DSD thermal neutron cross sections were regularized by adjusting the single-particle Woods-Saxon optical potential well depth, so that the potential elastic scattering length (R') of the adjusted well depth would fall within the uncertainty range of the values reported in the Mughabghab’s Atlas [26]. In particular, we have adjusted the depth of the real volume part of the Woods-Saxon potential for each chromium isotope. Modified parameter values used to calculate the reported DSD are shown in Table VIII. These adjusted values of the real volume potential depth were then used for calculations of DSD capture by the CUPIDO code, and the calculated thermal neutron DSD capture was then found to be reasonable and generally smaller than the measured total thermal capture cross sections of chromium isotopes. DSD neutron capture cross sections were computed in this way using the code CUPIDO between 0.01 meV and 1 MeV incoming neutron energy, and are shown

TABLE VII. ^{54}Cr resonance region integral metrics. Atlas results marked with “exp” refer to the Mughabghab’s evaluation based on the experimental data, while Atlas values derived from calculations are marked with “calc”. All major libraries except JENDL-4.0 used the same ORNL RRR from Ref. [5].

σ_{therm} (b)	(n,tot)	(n,el)	(n,γ)
This work	2.94	2.52	0.41
ENDF/B-VIII.0 [8]	2.93	2.52	0.41
BROND-3.1 [13]	2.93	2.52	0.41
Atlas (2018) [26]	2.95 ± 0.11	2.54 ± 0.20	0.41 ± 0.04
(1952) Pomerance [42]			< 0.3
(1954) Bazorgan [63]			0.36 ± 0.04
(1972) White [64]			0.34 ± 0.04

RI (b)	(n,tot)	(n,el)	(n,γ)
This work	50.98	47.24	0.21
ENDF/B-VIII.0 [8]	50.50	46.70	0.21
BROND-3.1 [13]	50.50	46.70	0.21
Atlas (2018) [26]			0.20 ± 0.04

MACS(30 keV) (mb)	(n,γ)
This work	4.78
ENDF/B-VIII.0 [8]	4.78
JENDL-4.0 [55]	4.69
BROND-3.1 [13]	4.78
Atlas (exp) (2018) [26]	6.2 ± 1.5
Atlas (calc) (2018) [26]	5.3 ± 1.0
KADoNiS-0.3 [56]	6.7 ± 1.6
(1971) Allen [57]	4.5
(1977) Kenny [60]	6.7 ± 1.6

in Fig. 15.

For calculations of captured neutron’s final bound state wave functions, the nuclear potential used by CUPIDO for all of the reported calculations in this work is the one of Bear and Hodgson [69]. In our single particle model of DSD capture into bound states of known binding energies, we have adopted a conventional approximation in which the bound state potential depth is varied to reproduce the binding energy of each bound state, e.g. [70]². Consequently, in this work the potential well depth of this potential was fitted by CUPIDO to reproduce the reported bound state energy of each bound state, which were supplied to CUPIDO as input parameters. Finally, amplitudes of DSD capture are computed as expectation values of an electromagnetic operator sandwiched between the incoming neutron wave function in the continuum and the captured neutron bound state. All DSD calculations reported in this work were performed using a current form of EM operator [65].

² An alternative convention is to use a bound state potential consistent with the OMP parameterization [71].

TABLE VIII. The strength of real volume part of the effective Woods-Saxon potential (at low energy) listed in column V_V , were adjusted to a corresponding value in column V'_V in order to make the potential scattering length R' of the modified potential fall within the uncertainty reported in Atlas in column R'_{Atlas} [26]. (No such modifications were needed for calculations of DSD capture on ^{50}Cr .)

Cr mass number	V_V [MeV]	V'_V [MeV]	R' [fm]	R'_{Atlas} [fm]
52	52.5	53.2	5.23	5.4 ± 0.3
53	52.2	52.7	5.41	5.64 ± 0.3
54	51.9	52.0	5.35	5.5 ± 0.3

The dominant contribution to the DSD capture for low energy neutrons is due to electric dipole (E1) transitions of neutrons in the incoming s -wave function. Therefore the most important capturing bound states in the corresponding $(A+1)$ chromium isotopes are those that could be reached by s -wave neutrons via an E1 transition. The spin-coupling algebra of quantum mechanics then implies that the bound states contributing the majority of DSD capture are those with orbital angular momentum value of 1, i.e. the bound p -levels. Consequently, we have collected published spectroscopic data of bound p -levels of the respective $(A+1)$ chromium isotopes, as deduced from (d,p) reactions, or from other neutron-depositing transfer reactions. (For $^{52,53}\text{Cr}$, $l = 0$ and 2 bound states were used in addition to $l = 1$ bound states.) Neutron single-particle spectroscopic factors of $^{51,53,54,55}\text{Cr}$ were taken from Refs. [72, 73], [74, 75], [76, 77], and [78, 79], respectively.

The DSD capture cross sections computed in this way were then used as input to the SAMMY code, where the (measured) total capture cross section was fitted as the sum of this DSD capture cross section and the resonant capture cross section computed by SAMMY using the Reich-Moore approximation. The inherent relative uncertainties of the DSD capture cross sections due to its model defect, spectroscopic factor uncertainties, etc., are approximately 20%.

Calculations of DSD capture were repeated recently using the newer version of the CUPIDO code that has a genuine Koning-Delaroche OMP parameterization built into it. These recent DSD calculations were found to be at most few percent apart from the original CUPIDO calculations, i.e., well within the experimental uncertainties, and therefore we have simply retained the original calculations for this evaluation. For completeness, the DSD capture computed using the Koning-Delaroche parameterization in the latest version of the CUPIDO code is plotted in Fig. 16, over a broader energy range showing the semidirect capture via giant dipole resonance in the 15 MeV range.

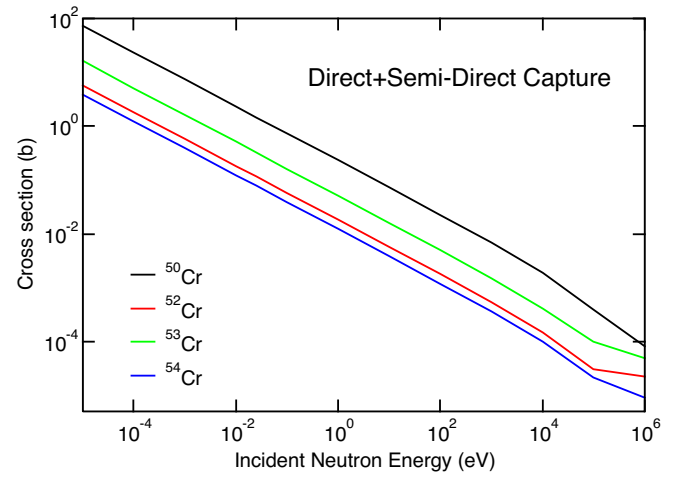


FIG. 15. (color online) Direct-semidirect (DSD) capture cross sections for all stable chromium isotopes used in this evaluation.

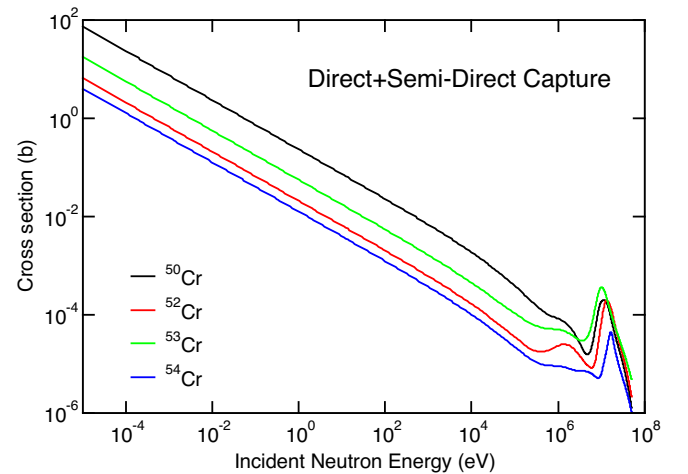


FIG. 16. (color online) Direct-semidirect (DSD) cross sections for all stable chromium isotopes computed using the latest version of the CUPIDO code using a genuine Koning-Delaroche OMP parameterization is found to be well within the experimental and the model uncertainties of the original calculations plotted in Fig. 15, and consequently the original DSD calculations were retained for the current evaluations. The new DSD calculations, including the large semidirect contribution due to giant dipole resonance in the 15 MeV range will be utilized when more accurate capture data become available in the future.

E. Angular distributions in the RRR

In the resolved resonance region, the angular distributions for all chromium isotopes were reconstructed from resonance parameters using the Blatt-Biedenharn formalism. This formalism uniquely reconstructs the angular distributions for a given scattering angle from the assigned spins of the resonances, and produces fluctuations

in the angular distribution on energy scales somewhat smaller than the energy grid used in the cross section reconstruction and occasionally finer than what can be accommodated by the ENDF 11-column floating point number format. Therefore the angular distributions were minimally smoothed so that the energy dependence of the angular distributions could be represented as faithfully as possible given the limitations of the ENDF format.

The resulting resonant behavior as a function of the incident energy can be seen in the black curves in Fig. 17, where the elastic cross section (top panel) and the first two coefficients ($P_1 \equiv \bar{\mu}(E)$ and $P_2 \equiv \xi(E)$) of the Legendre polynomial expansion of the elastic scattering distributions are plotted as a function of the incident neutron energy. Note that the plotted black curves were already smoothed to reduce the size of the file. However, additional resolution broadening of about 10% should be applied to compare with measured elastic angular distributions in the resonance region. The resolution broadened elastic cross sections and $\bar{\mu}(E)$ and $\xi(E)$ Legendre coefficients are shown as a function of the neutron incident energy in Fig. 17 with red lines. Note that significant fluctuations remain in the whole RRR (roughly below 2 MeV) despite the resolution broadening.

A comparison of resolution broadened angular distributions in the resonance region with ENDF/B-V, ENDF/B-VIII.0, and the current evaluation is shown in Figs. 18 and 19 for scattering on natural chromium and on ^{52}Cr major isotope, respectively. Note that the ENDF/B-V evaluation of angular distributions shown in Fig. 18 was based on low-resolution experimental data, while the ENDF/B-VIII.0 angular distributions were adopted from the ENDF/B-V evaluation with renormalized elastic cross sections³. The left column in Figs. 18 and 19 contains the 3% resolution-broadened curves, while the right column shows the 10% resolution-broadened curves; three different incident energies of 500, 800, and 1375 keV are shown in the upper, middle, and bottom rows for both cases. All these energies correspond to the RRR of the major ^{52}Cr isotope. The main point being stressed here is that the comparison of evaluations with low-resolution measured data requires strong smoothing to reproduce the experimental resolution. It should serve as a warning to avoid comparing low-resolution measured data with reconstructed angular distribution from the resonance parameters without applying resolution broadening to the reconstructed cross sections.

An improved description of experimental data can be clearly seen in Fig. 19 for the 10% curve (dashed red curve in the right column) compared to the 3% resolution broadened curve (dashed red curve in the left column) especially when the shape of the ratios is compared at all three analysed energies. Note also that the ob-

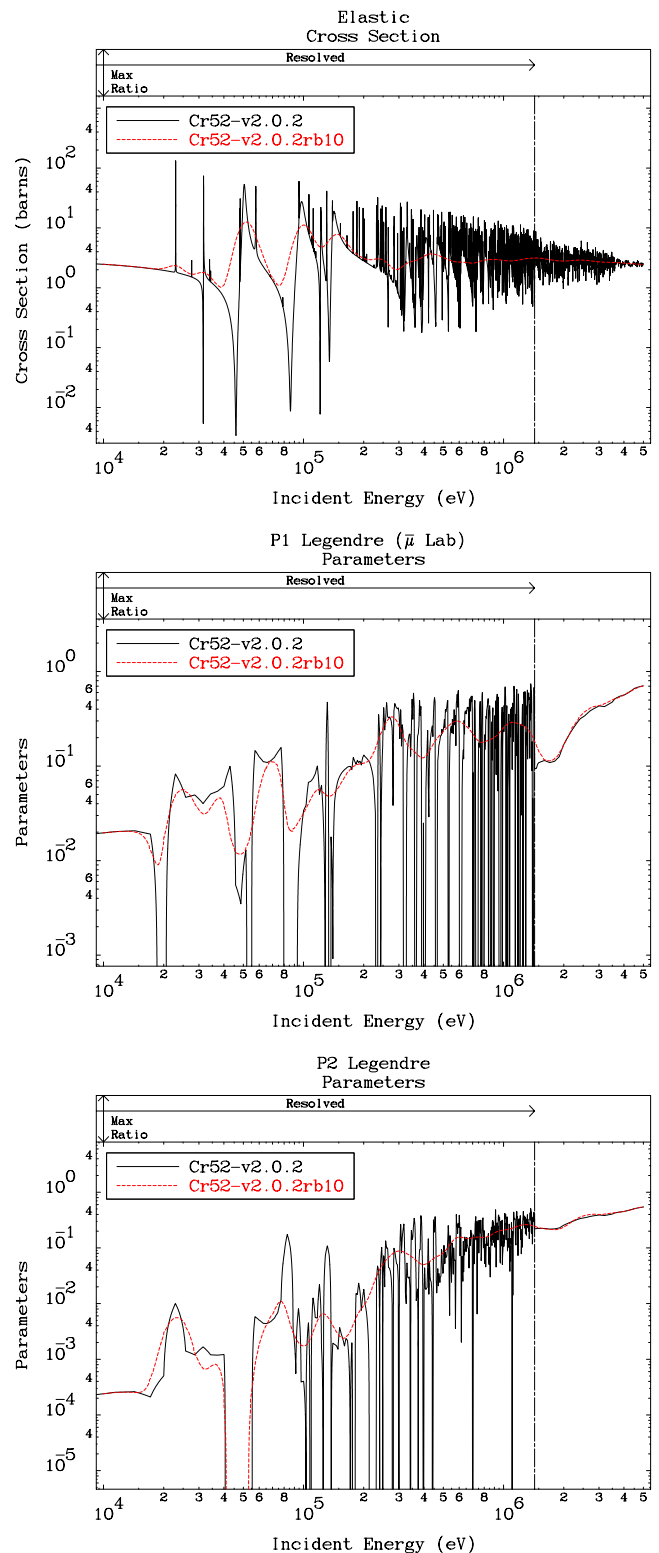


FIG. 17. (color online) Elastic cross section (top panel) and the $P_1 \equiv \bar{\mu}(E)$ coefficient (middle panel) and $P_2 \equiv \xi(E)$ coefficient (bottom panel) of the Legendre polynomial expansion of the elastic scattering distributions as a function of the incident neutron energy. Angular distributions on file are shown as black curves, while 10%–resolution broadened curves are shown in red.

³ Therefore, the shapes are exactly the same, shifted up or down according to the elastic cross section difference between the two evaluations.

served agreement with data both in normalization and shape is good in the whole energy range, and better than what was achieved in previous evaluations (see the bottom row of Fig. 19), especially at energies between 800 and 1375 keV, which correspond to the maximum probability of the fission neutrons.

A different comparison to experimental data, which is related to the calculated angular distributions, is shown in Fig. 20, where the 3% resolution broadened P_1 Legendre coefficient ($\bar{\mu}$) of the angular distribution in the laboratory system is shown as a function of the incident neutron energy. The energy range from 100 keV up to about 8 MeV corresponds to the region of relatively monotonic increase of the $\bar{\mu}$. There is a marked improvement in the description of measured data from 1 to 2 MeV as seen in the lower panel. A clear improvement of the description of measured data can be seen from 0.8 up to 1.3 MeV, near the end of the RRR. Fluctuations in data, specially in higher resolution data from Cox *et al.*, are much better captured by the new evaluation.

III. EXPERIMENTAL CONSTRAINTS ON FAST-REGION FLUCTUATIONS

In the energy range above the typical RRR (~ 0.5 MeV) to around 10 MeV, nearly all chromium isotopes exhibit fluctuations in their total cross section. This region of course is very important in reactors as it covers the majority of fission spectrum neutrons. This poses two problems:

1. In order to properly model leakage in nuclear systems, we require a detailed representation of the total and elastic cross sections as well as the elastic angular distribution. Because of the model lack of capability to predict observed fluctuations, this can only be done by directly fitting high-resolution experimental data.
2. Hauser-Feshbach theory combined with coupled channel calculations using an optical model potential can give us the best estimates of *energy averaged* cross sections and angular distributions. However to either demonstrate the efficacy of these calculations or to tune the model parameters, one requires energy averaged experimental results. Ideally, the optical model should reproduce the average cross section down into the resolved resonance region.

In either case, one relies on accurate, high resolution, experimental values. Table IX summarizes all total cross section measurements on all chromium isotopes (and elemental chromium samples) in the energy range 100 keV-10 MeV. In this table, we highlight several measurements with a single asterisk to denote that the experiment in question either has a fine enough energy resolution ($\Delta E < 250$ keV) over a large energy range to resolve

fluctuations in the cross section or has a well enough determined average cross section to be helpful in baselining the optical model calculations. There are two sets [4, 80] which were only available as transmission data. Although these were used in the resonance region evaluations, they have not been considered here. In the future we may consider converting these data to cross section data for the cross section fluctuation analysis.

We now discuss the sets highlighted in Table IX with the single asterisk.

(2001) *W.P.Abfaller, F.B.Bateman, et al.* - EXFOR entry 13753 [81] contains data from another “factory scale” systematic study of (n,tot) cross sections for 31 materials including ^{nat}Cr , in support of the Accelerator Production of Tritium project [82, 83]. These experiments were carried out at the LANSCE WNR target area 4 at Los Alamos National Laboratory. The goal of these measurements were a 1 % statistical accuracy in 1 % energy bins with systematic errors less than 1 % and this goal was achieved for the chromium target used. Indeed, the authors maintained such good control over the systematic uncertainties that the cross section covariance matrix is essentially diagonal in energy. The only potential source of error is that on the areal density of the chromium target which the authors claim is known to better than 0.5%. The target was a natural chromium powder encapsulated in a aluminum can and as metallic powder targets are prone to oxidation, there is a possibility of contamination. The authors did not note any structure from oxygen in the reconstructed cross sections given the statistical noise in the measurement.

(1973) *F.G.Perey, T.A.Love, et al.* - EXFOR entry 10342 contains data from ORELA measurements that were transmitted in a private communication [84] to Brookhaven, with very little information given. What we do know is that the authors performed transmission measurements on two separate elemental chromium targets with areal densities of 0.21060 a/b and 1.0490 a/b using the 47.350 m ORELA flight path with a burst width of 5 nsec. These experiments piggybacked off the measurements described in Ref. [85]. A careful reading of the EXFOR entry reveals that the targets were compressed chromium metal powder in a lucite binder and were formed into a right cylinder approximately 10 cm in diameter. This suggests that oxidation could be a problem with these samples, but we have no simple way to check. As the authors are deceased and ORELA is decommissioned, it is unlikely we will ever be able to find out more information about these experiments.

Three of the most interesting data sets are $^{52}\text{Cr}(n,\text{tot})$ from Agrawal *et al.*, $^{54}\text{Cr}(n,\text{tot})$ from Agrawal *et al.* [86] and $^{52}\text{Cr}(n,\text{tot})$ from Carlton *et al.* [15]. All are high resolution total cross section sets with detailed fluctuating structure above the first inelastic state threshold (~ 600 keV) that may help understand the total cross sections of $^{52-54}\text{Cr}$. Both the Agrawal sets and the Carlton set are believed to be chromium(III) oxide (Cr_2O_3) powder. Carlton *et al.* explicitly state that their targets are Cr_2O_3

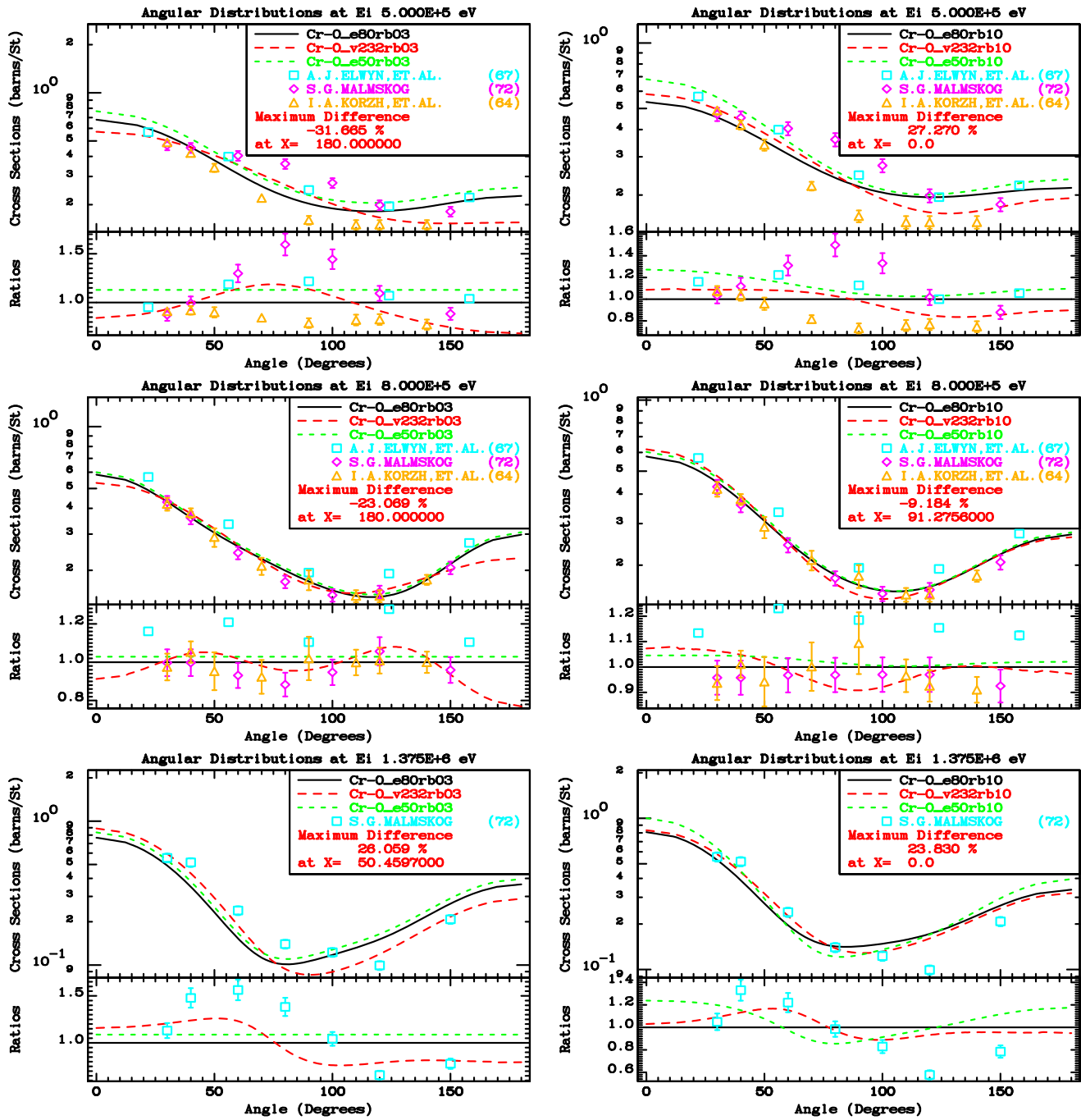


FIG. 18. (color online) Angular distributions of elastic scattered neutrons on natural Cr targets at three incident neutron energies of 500 (top), 800 (middle), and 1375 keV (bottom rows). The left column compares the ENDF/B-V evaluation (black), ENDF/B-VIII.0 evaluation (red dashed) and the current work (green dashed) with 3% resolution broadening; The right column compares the ENDF/B-VIII.0 evaluation (black) and the current work (red dashed) with 10% resolution broadening.

powder enriched with ^{52}Cr . For their transmission experiments they state that the target has an inverse thickness of 17.0 b/atom. Given that Agrawal *et al.*'s targets have inverse thicknesses of 25.33 b/atom (^{52}Cr target) and 18.48 b/atom (^{54}Cr target), we strongly suspect that the Agrawal targets are also powders in target containers of comparable dimension to those used by Carlton *et*

al. However, since both sets of experiments use powder and powder has a tendency to absorb water, the actual amount of H and O atoms in the targets may not be as well known as planned. This fact is openly acknowledged in the Carlton *et al.* paper [15]. This, coupled with many other problems, limit the usefulness of the Agrawal and Carlton datasets.

TABLE IX: Collection of (n,tot) data on chromium isotopes and natural chromium in the energy range 100 keV-10 MeV. Interesting data sets are flagged with an asterisk (*) next to the EXFOR entry number [87]. These sets are discussed in the text. Data sets marked with the double asterisk (**) are transmission measurement data and have not been converted to cross section data. We note that there are no usable sets for ^{50}Cr .

EXFOR Entry	Material	Ref.	Num. Pts.	E_{min} (MeV)	E_{max} (MeV)	Facility	Year/ Authors
11674.002	natCr	[88, 89]	472	0.00303	0.4085	ANL	(1957) C.T.Hibdon
11540.003	natCr	[90]	545	0.1007	0.6487	ANL	(1966) J.F.Whalen, J.W.Meadows
20482.002	natCr	[91–94]	164	0.5	1.206	CEA	(1967) J.Cabe, M.Laurat, <i>et al.</i>
20012.003	natCr	[95–98]	3883	0.5001	4.398	KfK	(1968) S.Cierjacks, P.Forti, <i>et al.</i>
20012.005	natCr	[95–98]	1231	4.4069	31.94	KfK	(1968) S.Cierjacks, P.Forti, <i>et al.</i>
10047.028*	natCr	[99]	240	2.339	14.888	PNNL	(1971) D.G.Foster Jr, D.W.Glasgow
10225.021	natCr	[100, 101]	218	1.001	8.696	BAPL	(1973) L.Green, J.A.Mitchell
10225.022	natCr	[100, 101]	214	1.011	8.39	BAPL	(1973) L.Green, J.A.Mitchell
10342.004*	natCr	[84, 85]	3658	0.18505	29.49684	ORNL	(1973) F.G.Perey, T.A.Love, <i>et al.</i>
10342.005*	natCr	[84, 85]	3658	0.18502	29.41653	ORNL	(1973) F.G.Perey, T.A.Love, <i>et al.</i>
12882.008	natCr	[102, 103]	685	1.9994	80.62	ORNL	(1980) D.C.Larson, J.A.Harvey, <i>et al.</i>
13753.017*	natCr	[81]	467	5.293	559.1	LANL	(2001) W.P.Abfaltrer, F.B.Bateman, <i>et al.</i>
14324.002**	natCr	[4]	30663	1.03e-5	0.631	ORNL	(2011) K. Guber, P. Koehler <i>et al.</i>
11601.004	^{50}Cr	[104]	1082	0.08	0.6205	Duke	(1966) J.A.Farrell, E.G.Bilpuch, <i>et al.</i>
20435.002	^{50}Cr	[105]	5181	0.026	0.285	KfK	(1972) R.R.Spencer, H.Beer, <i>et al.</i>
10047.029*	^{52}Cr	[99]	240	2.339	14.888	PNNL	(1971) D.G.Foster Jr, D.W.Glasgow
20435.003	^{52}Cr	[105]	5281	0.021	0.285	KfK	(1972) R.R.Spencer, H.Beer, <i>et al.</i>
22131.005	^{52}Cr	[61, 106]	8137	0.24001	1.2923	Geel	(1989) G.Rohr, R.Shelley, <i>et al.</i>
12830.008*	^{52}Cr	[86]	8310	0.0058679	4.9335	ORNL	(1984) H.M.Agrawal, J.B.Garg, <i>et al.</i>
13840.002*	^{52}Cr	[15]	13620	0.050185	31.162	ORNL	(2000) R.F.Carlton, J.A.Harvey, <i>et al.</i>
13840.005*	^{52}Cr	[15]	12213	0.066633	69.131	ORNL	(2000) R.F.Carlton, J.A.Harvey, <i>et al.</i>
10047.030*	^{53}Cr	[99]	248	2.262	14.828	PNNL	(1971) D.G.Foster Jr, D.W.Glasgow
20155.012	^{53}Cr	[107–110]	1657	0.016879	0.36003	KfK	(1971) K.-N.Mueller, G.Rohr, <i>et al.</i>
14324.004**	^{53}Cr	[4]	30663	1.03e-5	0.631	ORNL	(2011) K. Guber, P. Koehler <i>et al.</i>
11601.005	^{54}Cr	[104]	992	0.1	0.5955	Duke	(1966) J.A.Farrell, E.G.Bilpuch, <i>et al.</i>
12830.009*	^{54}Cr	[86]	8207	0.0053161	4.9277	ORNL	(1984) H.M.Agrawal, J.B.Garg, <i>et al.</i>
14114.004**	^{54}Cr	[80]	5169	0.0235	2.88	ORNL	(2006) R.F.Carlton, C.Baker, J.A.Harvey

(1984) H.M.Agrawal, J.B.Garg, *et al.* - EXFOR entry 12830 contains neutron transmission data for $^{52}\text{Cr}(n,\text{tot})$ (Run ID # 8914) and $^{54}\text{Cr}(n,\text{tot})$ (Run ID # 8910) from the paper of Agrawal, *et al.* [86]. These measurements were undertaken at the ORELA facility at Oak Ridge National Laboratory on the 78.203 m flight-path. Table I of this reference provides the isotopic composition of the targets. Neither ref. [86] nor ORELA log books [111] indicate the nature of the sample holder. Both

targets were run for about a week. Agrawal *et al.* state that they corrected their data for the oxide contribution using a background correction of

$$\sigma^{corr}(E) = \sigma^{meas} - 1.5 \times [3.6 - (2 \times 10^{-6})E] \quad (2)$$

where E is given in eV and σ in barns. While the prefactor of 1.5 arises from stoichiometry of a Cr_2O_3 unit cell, the additional 3.6 barns is a (poor) estimate of the zero energy intercept of the total ^{16}O cross section. Further-

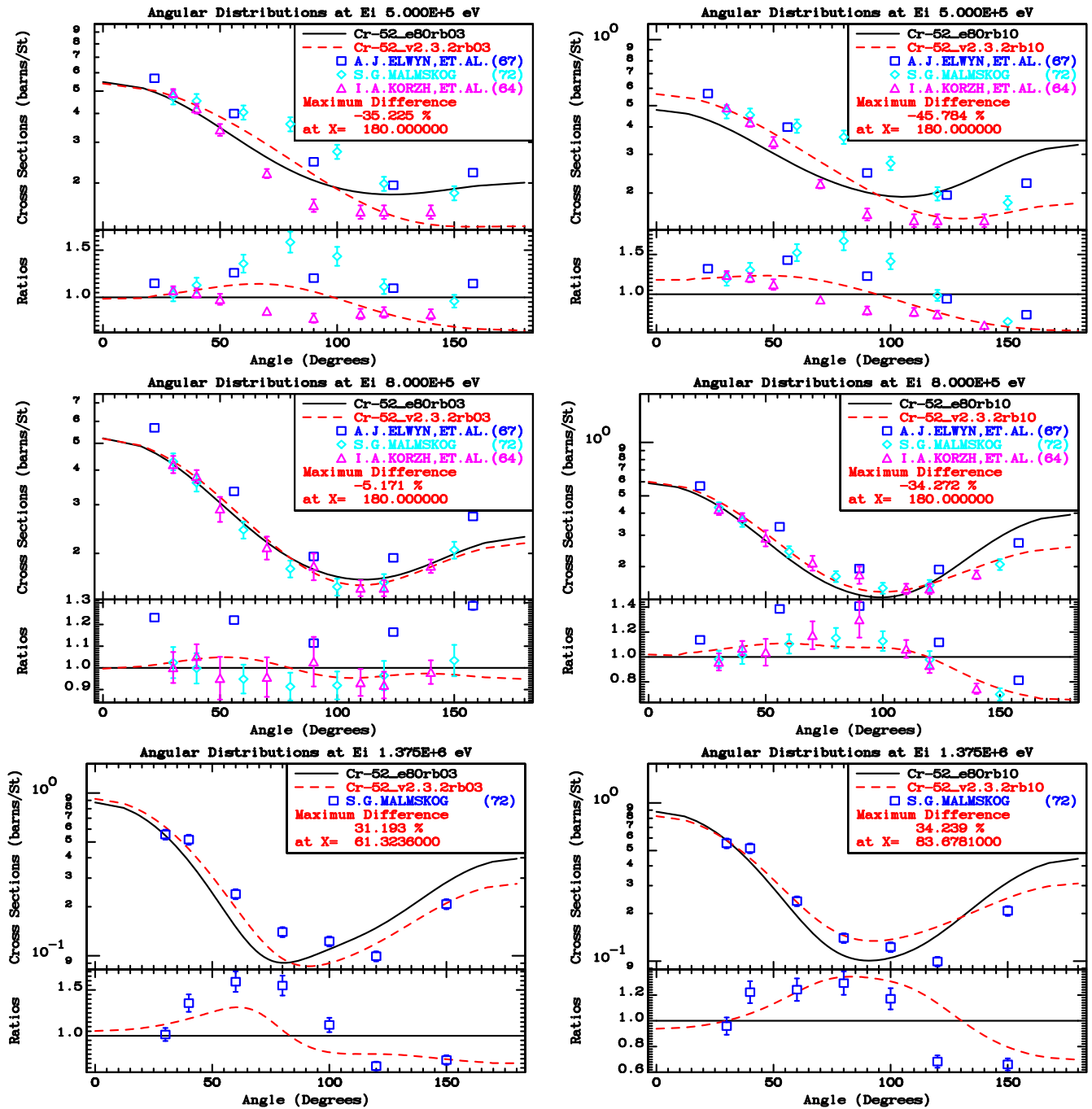


FIG. 19. (color online) Angular distributions of elastic scattered neutrons on ^{52}Cr targets at three incident neutron energies of 500 (top), 800 (middle), and 1375 keV (bottom rows). The left column compares the ENDF/B-V evaluation (black), ENDF/B-VIII.0 evaluation (red dashed) and the current work (green dashed) with 3% resolution broadening; The right column compares the ENDF/B-VIII.0 evaluation (black) and the current work (red dashed) with 10% resolution broadening.

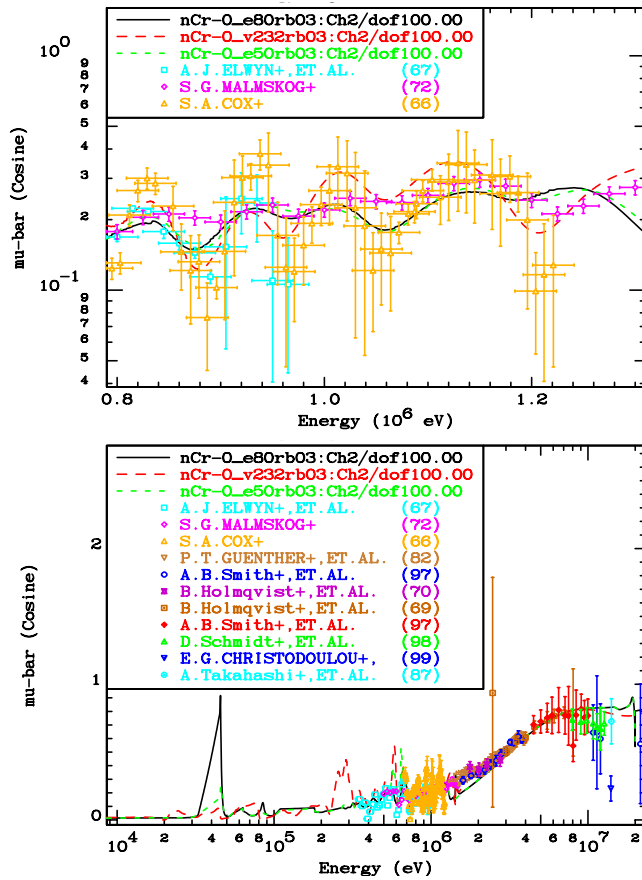


FIG. 20. (color online) Energy dependence of the P_1 coefficient ($\bar{\mu}$) of the Legendre polynomial expansion in the LAB system. The energy region from 10 keV up to 20 MeV is shown in the bottom panel, while the important region from 0.8 up to 1.3 MeV is zoomed on the upper panel. Black solid curves and red dashed curves correspond to 3% resolution-broadened ENDF/B-VIII.0 and current evaluation, respectively.

more, this factor only appears that it was used in the R-matrix analysis they performed using their measurements. At higher energies there is an obvious contribution from oxygen resonances. We attempted to correct for the presence of both oxygen and hydrogen (supposing that the powder sample absorbed water), but were unable to fully correct because of systematic energy shifts in both Agrawal *et al.* data. It appears that the ORELA resolution function, including flight path corrections due to rescattering in the ORELA water moderator [112], was not properly accounted for. Nevertheless, correcting for the rescattering and our best notion of the isotopic composition of the Agrawal *et al.* targets, we extracted a $^{52}\text{Cr}(n,\text{tot})$ cross section that is only in modest agreement with the data of Foster Jr. *et al.* [99]. In the end, the Agrawal data could not be used.

(2000) R.F. Carlton, J.A. Harvey, et al. - EXFOR entry 13840 contains neutron transmission data for $^{52}\text{Cr}(n,\text{tot})$ from the paper of Carlton, *et al.* [15]. This

TABLE X. Table of isotopic composition of the targets used by Agrawal *et al.* [86]. Taken from Table I of Ref. [86].

Sample	Isotope	Atomic Fraction (%)
$^{52}\text{Cr}_2\text{O}_3$	50	0.01
	52	99.87 ± 0.02
	53	0.12 ± 0.02
	54	0.01
$^{54}\text{Cr}_2\text{O}_3$	50	0.18 ± 0.05
	52	3.09 ± 0.10
	53	1.33 ± 0.10
	54	95.40 ± 0.10

TABLE XI. Table of isotopic composition of the targets used by Carlton *et al.* [15]. Given the nearly identical isotopic makeup of this target and the $^{52}\text{Cr}_2\text{O}_3$ target of Agrawal *et al.*, it is likely that the same target was used in both experiments.

Sample	Isotope	Atomic Fraction (%)
$^{52}\text{Cr}_2\text{O}_3$	50	0.01
	52	99.87
	53	0.12
	54	0.01

measurement was taken at the ORELA facility at Oak Ridge National Laboratory on the 201.575 ± 0.005 m flightpath. The longer flight path provide superb energy resolution even at high energies, eliminating the timing and energy resolution problems in the Agrawal *et al.* sets. The isotopic composition of the target used by Carlton *et al.* is shown in Table XI. The composition is nearly identical to Agrawal *et al.*'s $^{52}\text{Cr}(n,\text{tot})$ target, leading us to suspect that both Carlton *et al.* and Agrawal *et al.* used the same sample to produce their targets. That said, Carlton *et al.* took a more ingenious approach to correcting for the oxygen content of the target. Instead of a pure $^{52}\text{Cr}_2\text{O}_3$ target, Carlton *et al.* used a $^{52}\text{Cr}_2\text{O}_3+\text{Be}$ target and cycled it with a second BeO target. The thickness of the BeO target was designed so that the number density of oxygen scatterers in the BeO target was identical to that in the $^{52}\text{Cr}_2\text{O}_3+\text{Be}$ target. The amount of added Be was chosen to be identical to the number of Be scatterers in the BeO target. Together, it was hoped that the oxygen and Be content could be “subtracted” away [15]. At first glance, the correction appears to have worked. In Fig. 21 we show the ^{52}Cr total cross section in the range 4-20 MeV. The light blue set that is above all of the others is Carlton *et al.*'s original, uncorrected set. There are two things to note about this set. First, it appears to have not been corrected for the other isotopes in the target. We subtracted our best estimate of the contributions from other isotopes, using ENDF/B-VIII.0 cross sections for the other chromium isotopes, oxygen, hydrogen and

beryllium, resulting in the red points with the error band. This corrected the data below 5 MeV, but was unable to explain the portion above 5 MeV. This brings us to the second issue, this set appears to be two sets merged in an undocumented manner. Carlton *et al.* corrected this set, resulting in the other set in the red triangles. The nature of the correction is not documented in Ref. [15] or in the ORELA logbooks [111]. We note that these corrected points are systematically below both the ENDF/B-VIII.0 evaluation and the data of Foster and Glasgow [99].

IV. EVALUATED RESULTS IN THE FAST RANGE

Multi-channel evaluation in the fast region, regarded here to be where incident neutron energies are higher than the first inelastic of each isotope, were determined by the EMPIRE nuclear reaction code [113], unless stated otherwise. Selection of reaction models was based on quality of overall agreement of calculated cross sections with experimental data. Due to low-energy level densities being strongly parity asymmetric, we adopted RIPL-3 HFB level densities and tuned using the approach of Ref. [114] for ^{52}Cr . For the minor chromium isotopes we simply adopted the level-density model of Gilbert-Cameron [115]. Width fluctuation corrections were applied up to 9.9 MeV and pre-equilibrium was determined using the exciton model [116] as implemented in the code PCROSS [117]. Full γ -ray cascades for every excited nucleus were calculated. We employed γ -strength functions from the RIPL3 MLO1 formulation by Plujko for E1 transitions initiated from the continuum, for all nuclei. M1, E1 and E2 electromagnetic transitions were considered. Compound-nucleus decay and direct cross sections were added incoherently and compound-nucleus anisotropy was calculated using Blatt-Biedenharn coefficients.

In Table XII we identify the optical model potentials (OMP) used for the different reaction channels. In particular, for the incoming channel of $^{50,52,54}\text{Cr}$ targets we used the recently-developed, even-even chromium-specific, dispersive soft-rotor of Li *et al.* [118] (index #616 in RIPL) which was fitted as described in Ref. [118] using both neutron and proton scattering data and a soft-rotor model of nuclear structure that typically coupled the first five or six discrete levels of each target nucleus. For ^{53}Cr we used the same OMP, indexed in RIPL as #617, which is equivalent to #616 with rigid rotor couplings. The soft-rotor structure model provides an excellent description of the nuclear structure of quasi-spherical and very soft to deformation near-magic even-even chromium isotopes.

Model parameters were adjusted using the KALMAN code [123] using selected data sets as described in the sections below. Once optimal agreement through fitting was achieved, localized minor tuning was done for specific reactions to maximize agreement with certain data sets.

TABLE XII. Optical model potentials used in the EMPIRE calculations.

Ejectile	Type	RIPL #	Reference
n (direct)	CC (soft rotor)	616	Li+ [118]
n (direct)	CC (rigid rotor)	617 for ^{53}Cr	Li+ [118]
n (compound)	Spher.	2405	Koning+ [119]
p	Spher.	5405	Koning+ [119]
α	Spher.	9600	Avrigneanu+ [120]
d	Spher.	6200	Haixia+ [121]
t	Spher.	7100	Becchetti+ [122]
^3He	Spher.	8100	Becchetti+ [122]

A. Cross Sections

In this section we discuss cross sections for the major neutron-induced reactions on isotopes of chromium in the fast region. For the reactions that are not explicitly mentioned we accepted EMPIRE results without modifications. In general, in such cases, there were no significant (or any) data to compare with, or the calculated results were close to those measured.

1. Total Cross Sections

In ENDF/B-VIII.0, total cross sections in the fast range for chromium isotopes date back to the ENDF/B-VI MOD1 evaluation of Larson *et al.* from 1989 and were based on calculations with the spherical potential of Wilmore-Hodgson [124] using elemental transmission data. We provide significant improvements by using an isotopic-dependent coupled-channel approach with modern dispersive soft- and rigid-rotor optical model potentials. In our present evaluation we defined the total cross sections in the fast region as follows:

$^{52}\text{Cr}(n, \text{total})$ - For ^{52}Cr we made minor parameter adjustments to optical model parameters (changes smaller than 1%) to optimize agreement with smoothed $^{\text{nat}}\text{Cr}$ data of Green *et al.* [100] and Foster Jr. [99]. The optical model potential employed fails to describe the quick decrease of the total cross section data below 6 MeV which is a typical behavior for Cr/Ni/Fe targets. For this reason we replaced total cross sections between 3.6 and 6 MeV by the $^{\text{nat}}\text{Cr}$ experimental data of Perey [85], and, between the inelastic threshold and 3.6 MeV by the ^{52}Cr total data of Carlton *et al.* [15], which in this energy range is compatible with Perey, but of higher resolution. The higher resolution of Carlton *et al.* data is critical at energies lower than 3 MeV for the correct calculation of self-shielding factors, which are extremely sensitive to fluctuating data.

Fig. 22 compares the total cross section from the current work and ENDF/B-VIII.0 and relevant experimental

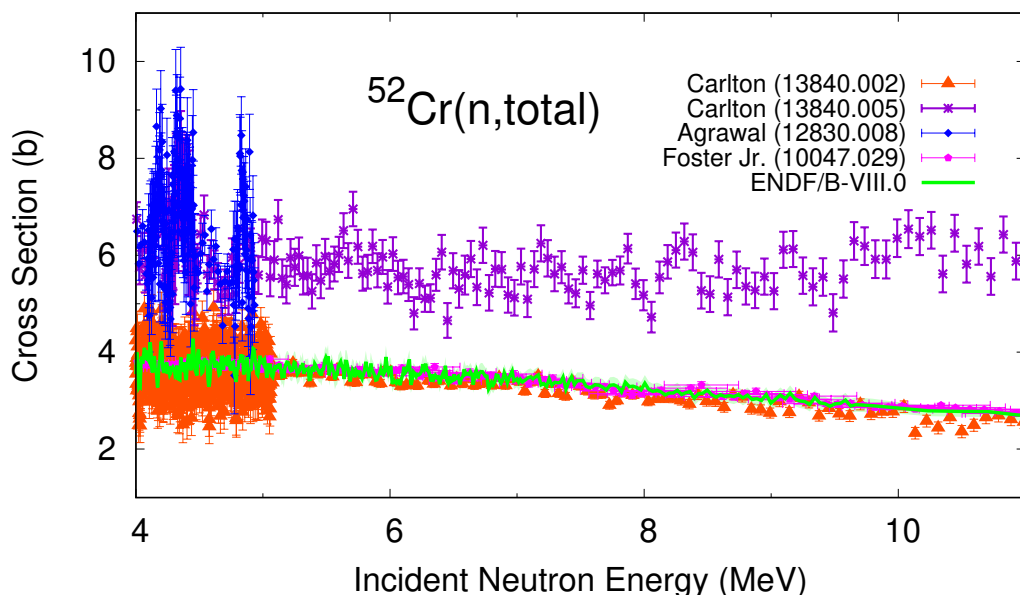


FIG. 21. (color online) Total cross-section data available for ^{52}Cr in EXFOR in the 4-20 MeV region, with ENDF/B-VIII.0 plotted as reference. Numbers in parentheses indicate EXFOR entries and subentries [87]. References for the experimental data can be found in Table IX. The reasons for the limited usability of the experimental data sets is discussed in the text.

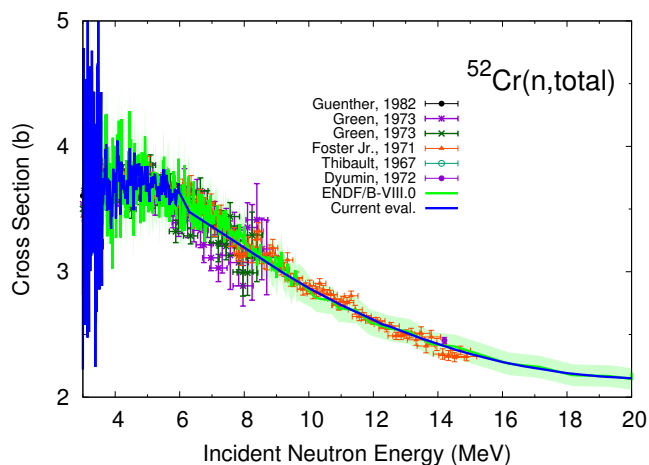


FIG. 22. (color online) Total cross section in the fast range region for ^{52}Cr . Data taken from Refs. [99–101, 125–127].

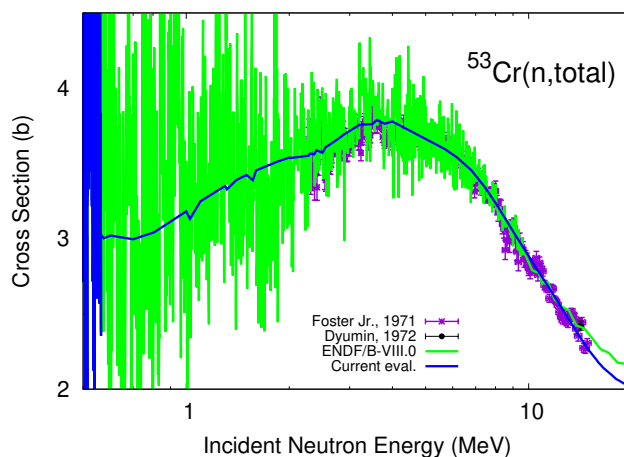


FIG. 23. (color online) Total cross section in the fast range region for ^{53}Cr . Data taken from Refs. [99, 127].

data.

$^{53}\text{Cr}(n,\text{total})$ - Due to the lack of higher resolution data specific for ^{53}Cr we simply fitted to experimental of Foster Jr. [99]. Fig. 23 shows our evaluated $^{53}\text{Cr}(n,\text{total})$ cross sections compared to ENDF/B-VIII.0 and experimental data. It is important to note that the fluctuations seen in ENDF/B curve in Fig. 23 were taken from elemental chromium data and therefore is not supported by any ^{53}Cr -specific data. Such fluctuations are already accounted for in our evaluation for ^{52}Cr total cross section.

$^{50}\text{Cr}(n,\text{total})$ - There were no experimental data available in the fast region, except a single point at

around 14 MeV from Dyumin et al. [127]. Therefore, our recommendation follows EMPIRE calculations. Both ENDF/B-VIII.0 and current evaluation agree with this single datum within 3%.

$^{54}\text{Cr}(n,\text{total})$ - Unfortunately, we were not able to use the data of Agrawal et al. [86], as described in Section III. Since there was no usable data in fast region, apart from a single point from Dyumin et al. [127] at ~ 14 MeV, we again followed EMPIRE calculations. Our evaluation agree with this single data point within $\sim 2\%$.

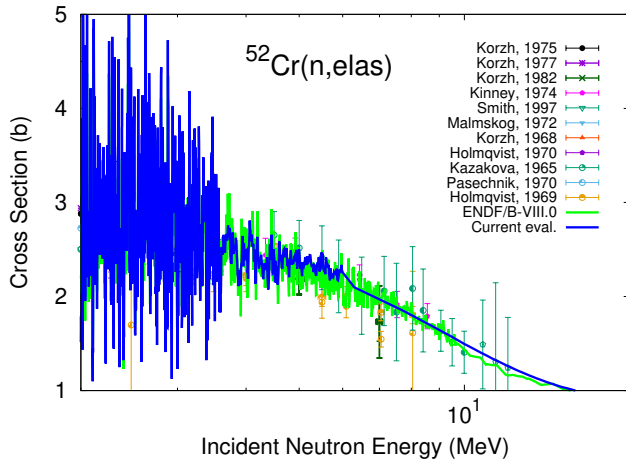


FIG. 24. (color online) Elastic cross section in the fast range for ^{52}Cr . Data taken from Refs. [128–138].

2. Elastic Cross Sections

The elastic cross sections are generally calculated from the optical model above 5 MeV. In the region of fluctuations they are defined as the difference between the total and the sum of the remaining partial cross sections.

$^{52}\text{Cr}(n,elas)$ - Even though the elastic cross sections were indirectly defined, through the difference between total and all other reactions, we can see in Fig. 24 that we achieve good agreement with experimental data, especially above fluctuations.

$^{50,53,54}\text{Cr}(n,elas)$ - There are no available elastic experimental data for ^{53}Cr and the few data points available for ^{50}Cr and ^{54}Cr have large error bars and are not constraining enough. We therefore adopted EMPIRE calculations for elastic cross section of the minor chromium isotopes.

3. Inelastic Cross Sections

In the fast neutron range, defined in the present evaluation as the region above the first inelastic threshold for each chromium isotope, the inelastic channel increasingly becomes the most important constraint, apart from total and elastic cross sections, at least until the opening of the $(n,2n)$ channel.

The inelastic thresholds for chromium isotopes are 564.03 keV, 783.32 keV, 834.855 keV and 1.4341 MeV for ^{53}Cr , ^{50}Cr , ^{54}Cr , and ^{52}Cr , respectively. Due to their relative abundance, the elemental inelastic cross section is strongly defined, above 1.4341 MeV, by the ^{52}Cr , hence its careful discussion below. The main constraint for the inelastic channel were the $^{52}\text{Cr}(n,n'\gamma)$ measurements of Mihailescu *et al.* [139] even though they in some cases differ strongly from previous measurements of Voss *et al.* For the minor isotopes, the most recent inelastic data dates back to the 1978 experiment of Karatzas *et al.* [140].

We were able to make the data set of Karatzas useful to our minor evaluation after realizing that their values reported in EXFOR did not correspond to the isotopic cross sections, but rather isotopic inelastic cross sections on a natural target, thus needing to be renormalized by their abundance. After this, we realized that the ^{52}Cr Karatzas data were in fact consistent with smoothed Mihailescu, bringing confidence to use it as constraint for the minor isotopes.

$^{52}\text{Cr}(n,inelastic)$ - Like many near-closed shell nuclides, chromium isotopes present strong fluctuations up to relatively high neutron incident energies. In this evaluation we make use of measurements of Mihailescu *et al.* [139], which were obtained through a 200 meter time-of-flight experiment using the white neutron spectrum of GELINA on a Cr_2O_3 sample. This thorough and detailed measurement was not taken into account in previous ENDF/B evaluations, even though JEFF-3.3 [7] has incorporated them in some form, at least for the neutron level cross sections.

Maximum consistency between inelastic neutron data and inelastic gamma cross-section measurements were attempted. For that, missing experimental unambiguous information related to branching ratios and high-level spin and parity in RIPL were complemented through constraints from gamma cross-section data. As examples of such changes, the level with excitation energy 3.9512 MeV was missing in RIPL, even though it can be found in ENSDF, and was added to the evaluation level scheme; levels with excitation energy 3.7396, 3.9475, 3.9512, and 4.1000 MeV had incomplete or non-existent decay information in RIPL and/or ENSDF. In Fig. 25 we show the predicted EMPIRE calculations for the gamma cross sections using decay scheme from RIPL, where missing branching ratios decay directly to ground state, as the red curve, and the current evaluation (blue curve), compared with Mihailescu data. In some few cases the agreement with data is not optimal: e.g., panels (f) and (h) of Fig. 25 are either consistently lower or higher than measured data; or in one case the evaluation agrees well with data of Voss *et al.* [141] but not as well with Mihailescu. However, generally, the agreement of the present evaluation with Mihailescu data is very good, in particular for neutron incident energies above ~ 5 MeV. We draw the attention for the good description of the main γ -emission cross section, i.e., the transition from the first excited state ($E_1 = 1.4341$ MeV) to the ground state, shown in Fig. 25 (a). Since a large majority of the level excitations in ^{52}Cr will eventually decay to the first excited level before reaching the ground state, this γ transition is a good approximation of total neutron inelastic, up to certain energy. We also point out to the measured transition of $E_\gamma = 1.2463$ MeV, shown in Fig. 25 (k). Since the experimental resolution of the Mihailescu measurement (1.1 keV at 1 MeV [139]) was not enough to separate the transitions $E_\gamma = 1246.278$ MeV (10th excited level to the 2nd) from the $E_\gamma = 1247.88$ MeV (15th excited level to the 4th). When the evaluated cross section for both transi-

tions is summed, a good agreement with measured data is reached.

We smoothed the total inelastic neutron cross section, as well as partial inelastic neutron cross sections so we could better assess the quality of our model-parameter fits. Because we adopted a realistic coupled-channels optical model potential, we were able to develop a consistent framework between Mihailescu data for inelastic neutrons, as well as for inelastic gamma cross sections, which are the actual observables of the experiment. In Fig. 26 we compare the total inelastic from the current evaluation with ENDF/B-VIII.0 and experimental data, in particular the ones from Mihailescu *et al.* We clearly identified the need to lower total inelastic cross section above 5 MeV, when compared to ENDF/B-VIII.0. In the decreasing part of total inelastic (above ~ 13 MeV), current evaluation is significantly lower than ENDF/B-VIII.0, in agreement with the upper bound of Mihailescu data. Attempts to lower it further to improve agreement with data would implicate poor description of other threshold reaction channels open at this energy such as (n,p) and (n,2n). However, considering the good agreement with Mihailescu data seen in Fig. 25(a) in this same energy region suggests that the total inelastic neutron data may be slightly underestimated at such higher energies.

Due to the expected diminishing of predictive quality of the optical model approach at energies below 5 MeV, we decided to simply adopt Mihailescu data for the first 5 excited level cross sections below 5 MeV (first inelastic) and 4 MeV (second to fifth inelastic channel), constrained by total cross-section data and with the difference put into the elastic channel. Fig. 27 shows the partial inelastic cross sections for the first four excited levels. Noteworthy is the fact that, for the first excited level, our evaluation also agrees well with the higher-energy set of Schmidt [147], bringing to consistency inelastic gamma, partial level, and total neutron inelastic cross-section data.

$^{53}\text{Cr}(n,inelastic)$ - For ^{53}Cr we fitted to total inelastic data of Karatzas *et al.* [140], reaching a good agreement. The current evaluation lowers total inelastic significantly above ~ 2 MeV in comparison with ENDF/B-VIII.0, as can be seen in Fig. 28 (top panel). In the bottom panel of Fig. 28 we show a comparison for the inelastic cross section of the first level. The agreement with data is not as good but these data carry additional measurement difficulties due to the low excitation energy.

$^{50}\text{Cr}(n,inelastic)$ - Fig. 29 shows the ^{50}Cr total inelastic cross section, as well as the partial cross sections for the first three excited levels. As mentioned above we fitted to data of Karatzas *et al.* [140], obtaining a good agreement with experimental data, and generally better than ENDF/B-VIII.0.

4. Capture Cross Sections

$^{52}\text{Cr}(n,\gamma)$ - For a magic nucleus like ^{52}Cr capture cross sections in the fast region are small. Availability of data for this nucleus is also poor as the resulting compound nucleus is stable as can be seen in Fig. 30, where we compare the present evaluation with ENDF/B-VIII.0 and the single datum available, from Frenes *et al.* Our evaluation is consistently lower than ENDF/B-VIII.0 from threshold up to around 14 MeV, but there are no data available to constrain them in this region. Our evaluation does however reproduce better the cross-section cusps due to the opening of inelastic channels, as well as the 14 MeV datum.

$^{50}\text{Cr}(n,\gamma)$ - The only other chromium isotope to have capture data in the fast region is ^{50}Cr , even though, like ^{52}Cr it is just a single point. Nevertheless, this point of Yijun Xia *et al.* [159] helped us constrain the capture normalization, as seen in Fig. 31.

5. (n,2n) Cross Sections

$^{52}\text{Cr}(n,2n)$ - The existing ENDF/B evaluation for $^{52}\text{Cr}(n,2n)$ ^{51}Cr cross sections dates back from ENDF/B-VI-MOD1 [10], done by D. Larson (ORNL) in 1989. In that evaluation, the cross sections were taken from the activation file for ^{52}Cr but were adjusted to be smaller below the energy of 15.5 MeV to match the data of Wagner *et al.* [160] which agreed well with other data from up to the same period in this energy region.

For our new evaluation, in addition of the data of Wagner [160], we considered $^{52}\text{Cr}(n,2n)$ experimental sets equally or more recent than the previous 1989 evaluation (Refs. [161–168]). Ultimately, we fitted to the dosimetry file IRDFF v1.05 [169, 170] below 20 MeV, which is compatible with the data sets listed. Since the IRDFF-1.05 above 20 MeV corresponds to a renormalized TENDL library not fitted to data, we decided to fit to Uno data above 20 MeV. Fig. 32 shows the $^{52}\text{Cr}(n,2n)$ cross section from our evaluation compared to ENDF/B-VIII.0, IRDFF-1.05 and experimental data. It should be noted that our evaluation is slightly higher than the IRDFF file below 20 MeV and the shape between 16 and 20 MeV disagree with data. The IRDFF file is recommended for neutron dosimetry applications.

6. (n,p) Cross Sections

$^{52}\text{Cr}(n,p)$ - The previous $^{52}\text{Cr}(n,p)$ ^{52}V dates back from ENDF/B-VI-MOD1 [10], done by D. Larson (ORNL) in 1989. The (n,p) cross sections had been calculated by the TNG code [171–174] but modified between 7–16 MeV for better fit of the experimental data up to 9 MeV of Smith *et al.* [175] and measurements, by then recent, at 14.5 MeV [176–178]. There are many experimental data sets which are newer than the previous eval-

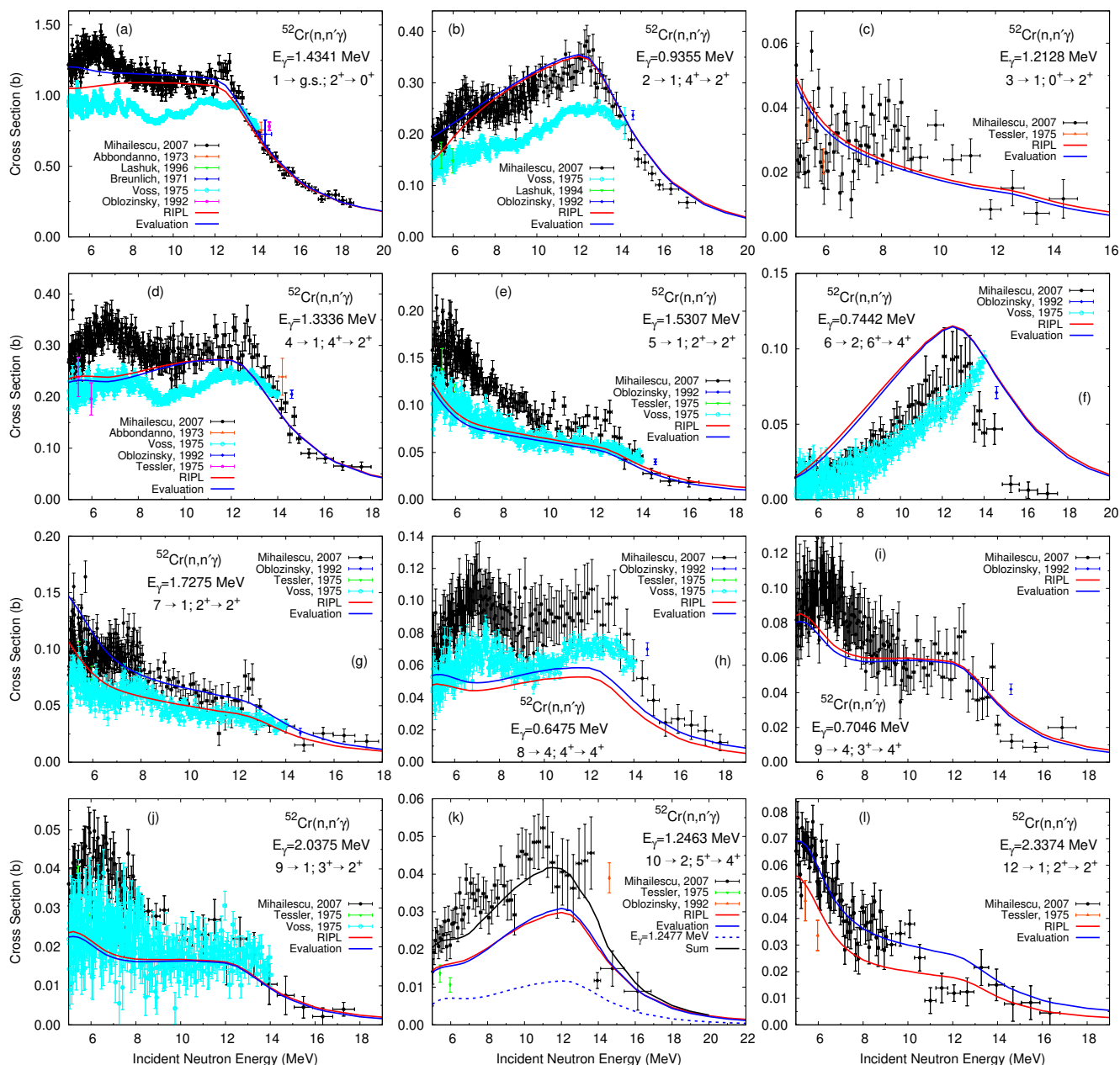


FIG. 25. (color online) Inelastic gamma cross section measurements for ^{52}Cr . The energy of the transition γ is indicated in each panel, as well as the index, spins, and parities of the levels involved in the transition. Results are shown only above neutron incident energy of 5 MeV as model calculations were replaced by experimental data for the first neutron inelastic level cross section below 5 MeV and second to fifth levels below 4 MeV. Data taken from Refs. [139, 141–146].

uation, even though some display inconsistencies among them. The data of Fessler *et al.* [163] begins at 9.31 MeV, which is above all Smith data used in the previous evaluation, and goes up to 21.1 MeV. Data from Mannhart *et al.* [179] overlaps with Smith at 7.9 MeV and goes up to 14.5 MeV. Both sets of Fessler [163] and Mannhart [179] play an important complementary role relative to the previous evaluation. In addition to these sets, the new (n,p) data considered in this evaluation were Refs. [180–186]. Older sets or data sets with clear conflicting points were

excluded from fits and tuning. Fig. 33 shows a comparison between the present work and ENDF/B-VIII.0 and the experimental data mentioned above. A clear improvement in the agreement with data, especially above around 9 MeV can be observed.

$^{50}\text{Cr}(n,p)$ - Fig. 34 shows a comparison between the present evaluation and ENDF/B-VIII.0 with experimental data. It can be seen that both describe equally well the data from Smith *et al.* [175] at lower range and the peak of (n,p) cross section, but the current evaluation de-

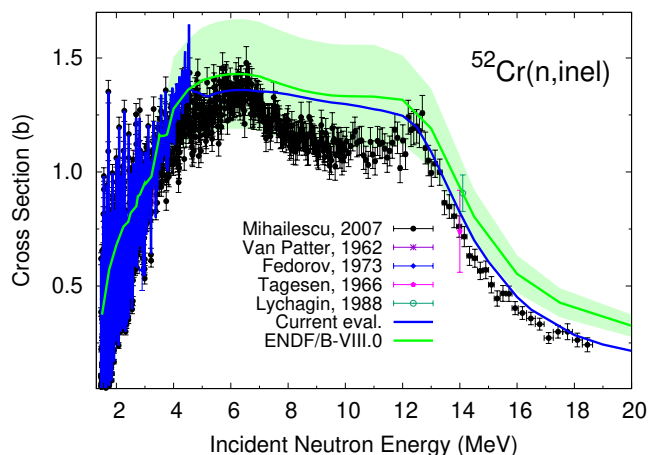


FIG. 26. (color online) Total inelastic cross section measurements for ^{52}Cr . Data taken from Refs. [139, 148–151].

scribe better the high-energy data of Fessler *et al.* [163].

$^{50}\text{Cr}(n,p)$ - As seen in Fig. 35, there is only a single datum for the $^{50}\text{Cr}(n,p)$, which is from Klochkova *et al.* from 1992 [190]. In our fits we ensure that the evaluation go through that experimental point.

$^{54}\text{Cr}(n,p)$ - In the case of ^{54}Cr , the (n,p) reaction can be constrained by some experiments that overlap those of ^{52}Cr (Fig. 36). Some of those are newer than the previous ENDF/B evaluation. We performed fits of model parameters taking in consideration the sets shown in Fig. 36, reaching a good agreement in the rising part of the cross section, in particular with the most recent experiment of Tran Due Thiep *et al.* [181]. Even though the agreement with the set of Fessler *et al.* [163] in the decreasing part of the cross section is far from optimal, it is in a much better qualitative agreement with data than ENDF/B-VIII.0, for which the (n,p) cross section continues to increase after 16 MeV and beyond 20 MeV.

B. Elastic and Inelastic Angular Distributions

In the fast region, the ^{52}Cr elastic angular distributions between 1.6 and 2.8 MeV were taken from a fit of experimental data of Guenther *et al.* [125], after small tuning to increase forward scattering by half the uncertainty. Above 4.5 MeV, angular distributions were taken directly from EMPIRE calculation.

For ^{53}Cr , we adopted elastic angular distributions from ENDF/B-VIII.0 between 600 keV and 3 MeV. Above that, angular distributions were provided by EMPIRE calculations. For $^{50,54}\text{Cr}$, all angular distributions in the fast region were taken from EMPIRE, as well as all inelastic angular distributions for all isotopes.

In Fig. 37 elastic angular distributions for ^{52}Cr are shown for select incident energies starting at 6 MeV, i.e., above the region where fluctuations in the elastic cross section are relevant. We see that even though our evalu-

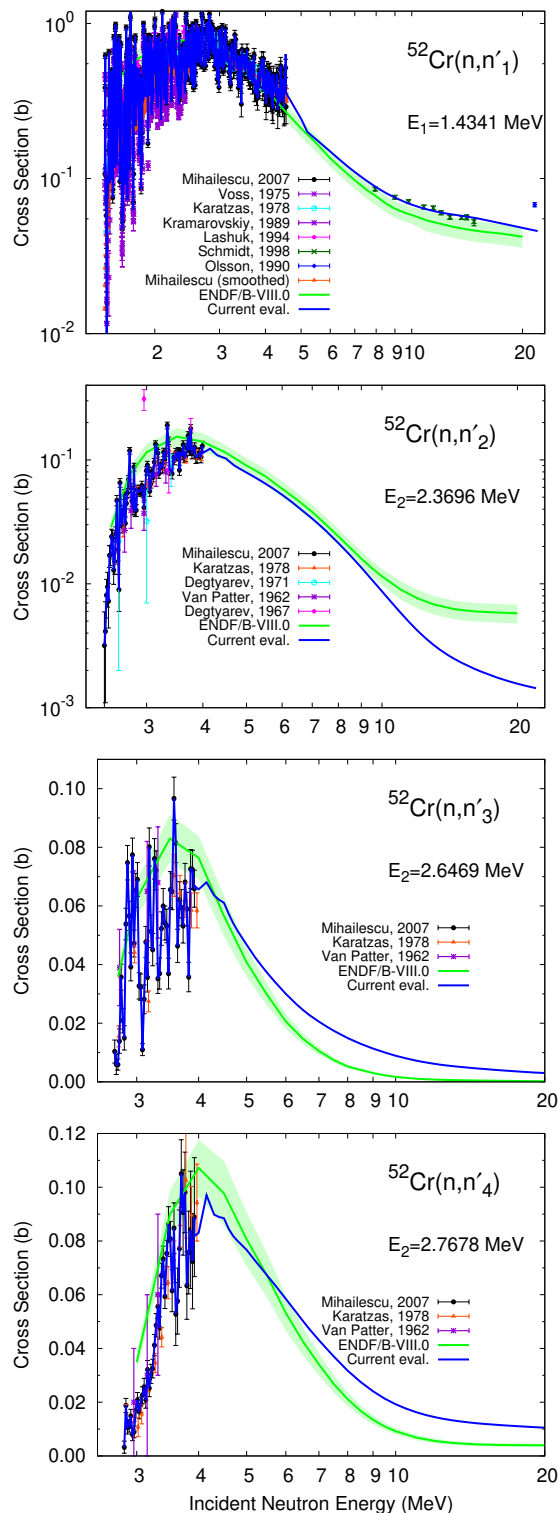


FIG. 27. (color online) Partial inelastic cross section measurements for ^{52}Cr . Data taken from Refs. [139–141, 143, 148, 152–156].

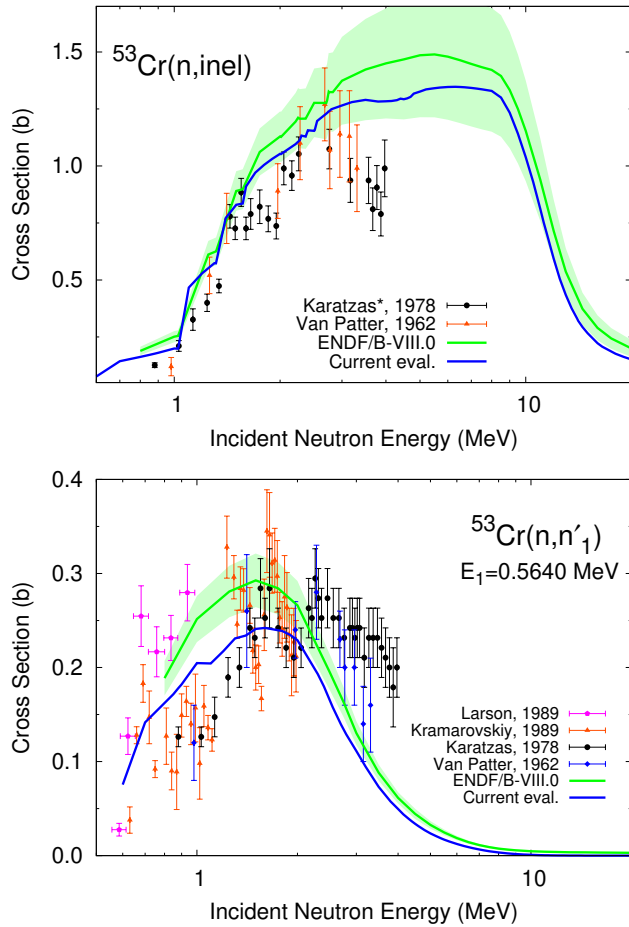


FIG. 28. (color online) Total inelastic cross section for ^{53}Cr (top panel) and for the first excited level, which has excitation energy of 0.5640 MeV. Data taken from Refs. [140, 148, 152, 157].

ation does not differ much from ENDF/B-VIII.0, where it does it is consistently in better agreement with experimental data. This is an indication in support of the optical model potential employed.

Similarly, Fig. 38 shows evaluated inelastic angular distributions for the first inelastic state of ^{52}Cr compared to ENDF/B-VIII.0. Again, we focus on incident energies above 6 MeV, where the impact of cross-section fluctuations is much smaller. The most relevant experimental sets available are from Schmidt *et al.* [153], Korzh *et al.* [130], and Kinney *et al.* [131]. The Schmidt data set corresponds to a 12 m time-of-flight (TOF) experiment with neutron incident energies ranging from about 8 to 15 MeV, and is the most reliable of the three sets. From panels (a)-(d) of Fig. 38, which show examples of the Schmidt set for 14.76, 14.10, 11.44, and 9.80 MeV respectively, we see that, while ENDF/B-VIII.0 is not able to fully describe the observed data, our evaluation agrees very well with data, even reproducing some details of the measured angular distributions. This behavior is observed for all incident energies of the Schmidt set, even

though for the lower-energy ones the agreement at very low and very high scattering angles may not be as good. In panels (e) and (f) of Fig. 38 we show comparisons with the lower resolution experiments of Korzh and Kinney, at lower incident energies. Again we see that our current evaluation provides a much more realistic angular distributions for the first inelastic channel of ^{52}Cr . This is likely due to the fact that we use an optical model potential based on a significantly better structure model in our calculations than what was used in ENDF/B-VIII.0, namely the dispersive optical potential of Li *et al.* [118], which takes into account the soft-rotor degrees of freedom of chromium isotopes.

There are also elastic and inelastic angular distribution data for natural samples of chromium in the fast region. The main data sets are the ones from Smith *et al.* [132] and Schmidt *et al.* [153], in addition to other relevant experiments. Even though the inelastic angular distributions do not bring much more information than that of isotopic data, it is instructive to compare elastic angular distributions. Fig. 39 shows examples of such angular distributions for select different neutron incident energies. At higher energies there is a clearly better agreement of the current evaluation with data than ENDF/B-VIII.0. This become not so evident below ~ 5 MeV where the optical model becomes not as reliable, and the agreement with data is poorer, both from the current evaluation and ENDF/B-VIII.0.

In contrast with Fig. 37 that shows that ^{52}Cr isotopic elastic angular distributions from our evaluation is mildly in better agreement with data than ENDF/B-VIII.0, in the case of natural chromium our evaluation is in significantly much better agreement with measurements than previous ENDF/B-VIII.0 evaluation, except at 3 MeV of incident neutron energy as shown in Fig. 39. This indicates that the angular distributions for minor isotopes have also been improved.

C. Energy Spectra

There are several measurements of neutron energy spectra concentrated around 14 MeV. At these incident energies, the high outgoing-energy end of the spectra is dominated by the elastic peak and direct transitions to the collective levels that are well modeled by CC and DWBA calculations. The middle part of the spectrum is governed by the PE emission, while the low energy peak is the evaporation peak described by the Hauser-Feshbach model. Proper description of the neutron spectra is thus a very good overall test of the quality of the reaction modeling used in the evaluation.

D. Double Differential Cross Sections

Energy-angle correlated cross sections add another dimension to the energy spectra, associated with the scat-

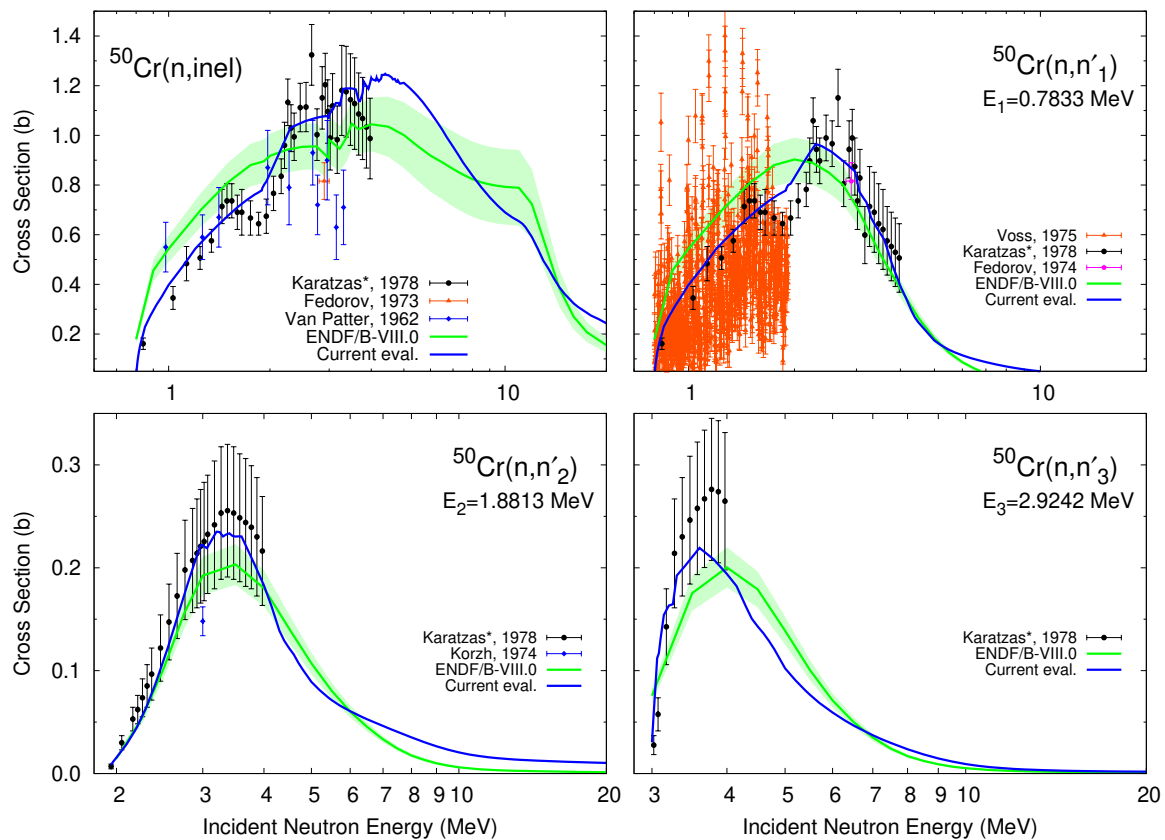


FIG. 29. (color online) ^{50}Cr inelastic cross sections for the sum of all levels (top left) and for the first, second, and third excited levels, which have excitation energy of 0.7833 MeV, 1.8813 MeV, and 2.9242 MeV, respectively. Data taken from Refs. [128, 140, 141, 148, 149].

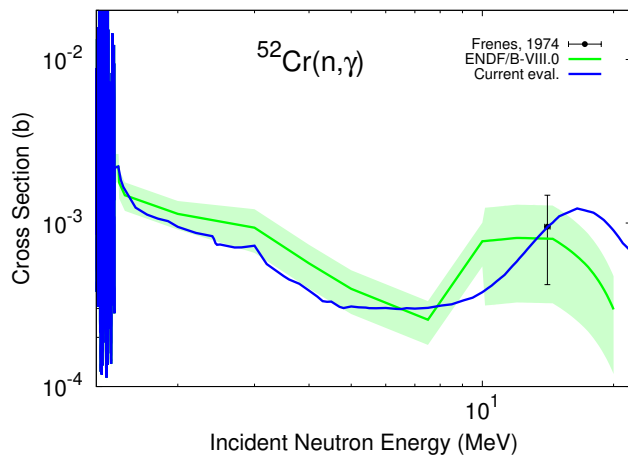


FIG. 30. (color online) Capture cross section for ^{52}Cr in the fast neutron range. Data taken from Refs. [158].

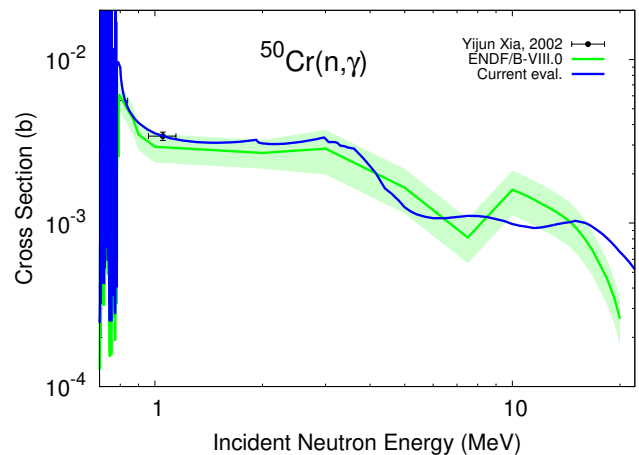


FIG. 31. (color online) Capture cross section for ^{50}Cr in the fast neutron range. Data taken from Refs. [159].

tering angle. These arguably correspond to an even more direct kind of measurement since energy spectra are usually obtained by integrating double-differential (DD) ones which unavoidably involves some approximations related to interpolation and extrapolation of angular distribu-

tions. However, employed models in EMPIRE rely on empirical Kalbach parameterization of double differential cross section [200]. Therefore, comparison of an evaluation with double-differential cross sections provides for an additional stringent test of the modeling employed in the

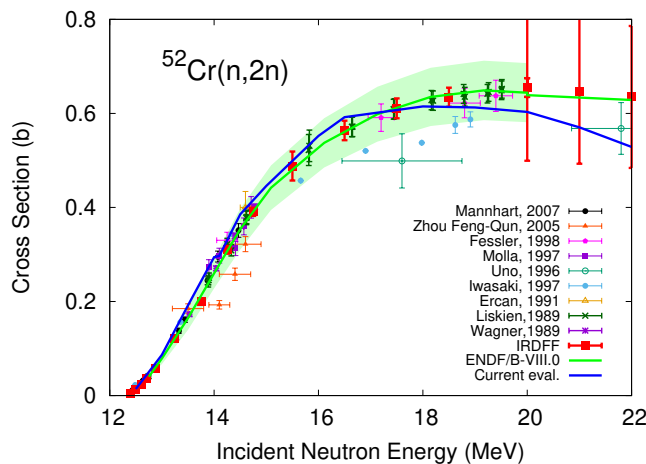


FIG. 32. (color online) Evaluated $^{52}\text{Cr}(n,2n)$ cross section compared to ENDF/B-VIII.0, IRDFF [169, 170] and experimental data [160–168].

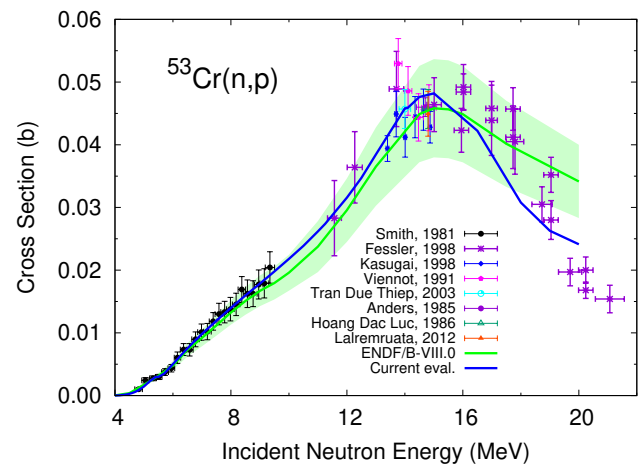


FIG. 34. (color online) Evaluated $^{53}\text{Cr}(n,p)$ cross section compared with ENDF/B-VIII.0 and with relevant experimental data [163, 180–182, 184, 187–189].

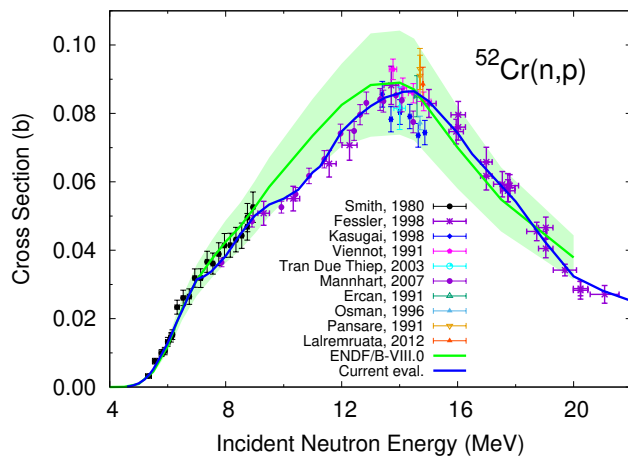


FIG. 33. (color online) Evaluated $^{52}\text{Cr}(n,p)$ cross section compared with ENDF/B-VIII.0 and with relevant experimental data [163, 175–186].

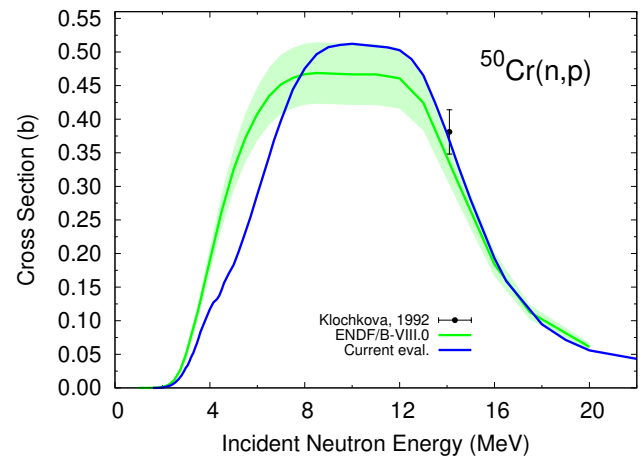


FIG. 35. (color online) Evaluated $^{50}\text{Cr}(n,p)$ cross section compared with ENDF/B-VIII.0 and with relevant experimental data [190].

evaluation procedure.

1. Neutron Double-Differential Spectra

There are double-differential (DD) neutron data available for $^{\text{Nat}}\text{Cr}$ for a variety of incident energies ranging from 7.95 MeV up to 14.8 MeV, each for a different set of scattering angles. Undoubtedly, the widest variety of measured angles is associated with experiments at neutron incident energies of 14.1 MeV due to the availability of almost monoenergetic D-T neutron sources. Because of that, and also due to the importance for fusion of 14–15 MeV D-T neutrons (e.g., as illustrated by the leakage experiment discussed in Section V), we focus our DD discussion here on this incident energy. Conclusions can

certainly be extrapolated to other incident energies where data are available.

In Fig. 41 we show the DD spectra cross sections for 14.1 MeV incident neutrons on $^{\text{Nat}}\text{Cr}$ as a function of the neutron outgoing energy E_{out} at six different scattering angles, which were chosen as a general representation of the whole scattering solid angle: 30, 60, 90, 110, 130 and 150 degrees. The three main data sets available at this energy are from Schmidt *et al.* [198], Matsuyama *et al.* [201], and Takahashi *et al.* [196]. Smith's data set is the most recent one and spans across more angles but often has no points around the elastic and first inelastic peak, while Takahashi and Matsuyama tend to have broader resolution. Even though Schmidt's data is generally consistent with the two other sets, there are discrepancies, especially at more forward angles, as can be seen in the 30 degree panel in Fig. 41. Matsuyama

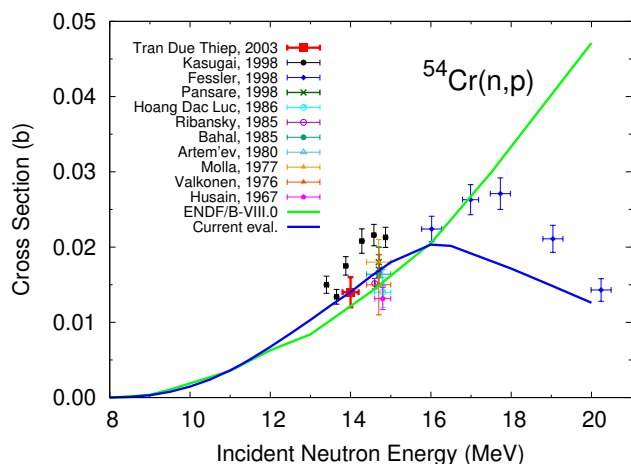


FIG. 36. (color online) Evaluated $^{54}\text{Cr}(n,p)$ cross section compared with ENDF/B-VIII.0 and with relevant experimental data [163, 177, 181, 182, 186, 189, 191–195].

and Takahashi data are normally smoother in the continuum/preequilibrium region ($E_{\text{out}} = \sim 2$ to ~ 8 MeV) but present some structure in the discrete region $E_{\text{out}} = \sim 8$ to ~ 13 MeV. By comparing the current evaluation with ENDF/B-VIII.0 in regards to agreement with data, it is generally observed that the current evaluation is better in the continuum and preequilibrium region with a smoother transition to the compound component. The present evaluation has a small peak in the outgoing neutron energy between 8 and 9 MeV, which seems to be supported by data. That is not completely clear only for very backward angles (e.g., 150 degrees). On the discrete-level part, there are scattering angles for which ENDF/B-VIII.0 seems better (e.g. 60 and 90 degrees), cases where the current evaluation seems to be in better agreement (e.g. 30 degrees), but also cases where there is not a clear way to determine which agrees better with data (e.g. 110 and 130 degrees). Noteworthy is that frequently there is a low cross-section point from Schmidt (eg. 90, 130 degrees) at around $E_{\text{out}} \sim 11.5$ MeV that our evaluations seems to agree to better. Regarding the first inelastic and elastic peaks, generally there is a small advantage for the current evaluation (e.g. 30 degrees) but both the evaluation and ENDF/B-VIII.0 agree well with data, especially if broader resolution is employed. Differences between ENDF/B-VIII.0 and current evaluation at the elastic peak vary with the scattering angle, which can be understood by the differences in angular distributions (see Fig. 39).

2. γ Spectra

In addition to properly describing the cross section of the scattered neutrons for all angles and outgoing energies, for all incident energies, a fully consistent evaluation should also be able to accurately provide analogous in-

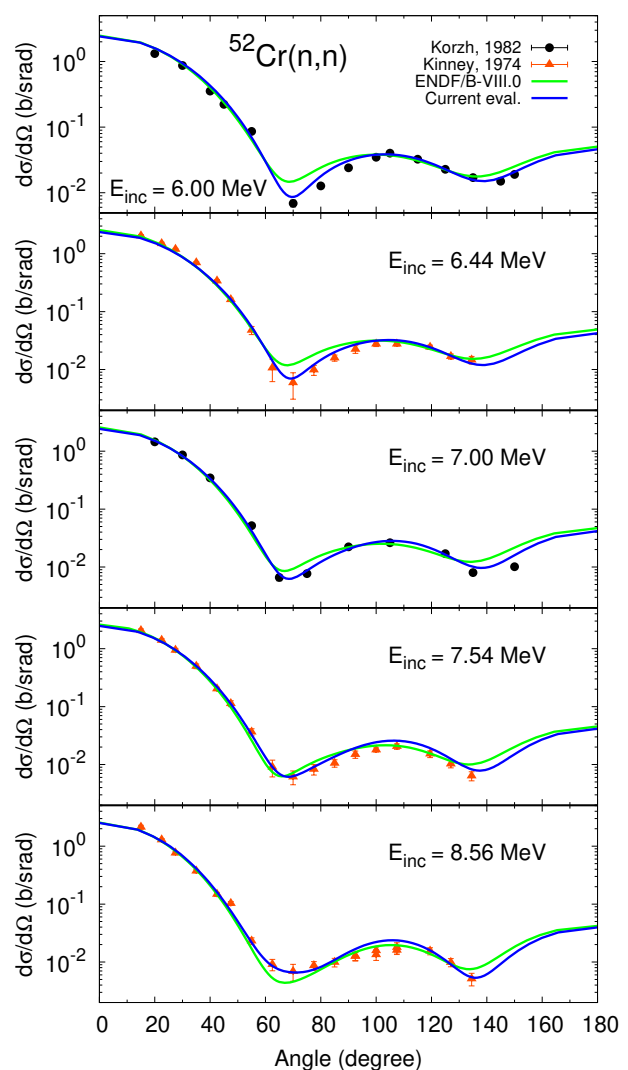


FIG. 37. (color online) $^{52}\text{Cr}(n,\text{elas})$ elastic angular distribution in the fast region. Experimental data taken from Refs. [130, 131].

formation about the scattered gammas. In practice such task is not that simple, as the full evaluation is normally a complex combination of experimental data and models that may not be fully self-consistent. Nevertheless, it is still a very instructive way to assess strong points and deficiencies of the evaluation. In Fig. 42 we compare the evaluated double-differential spectra of gamma production, as a function of the outgoing γ energy for select values of neutron incident energy and scattering angle, with experimental data.

We see that, in general, the peaks at gamma energies corresponding to the inelastic transitions of the first few excited levels of ^{52}Cr , the major isotope in elemental chromium, are much better described by the current evaluation than ENDF/B-VIII.0. This is likely due to the effort done in the evaluation in consistently fitting inelastic gamma and neutron cross sections, as described

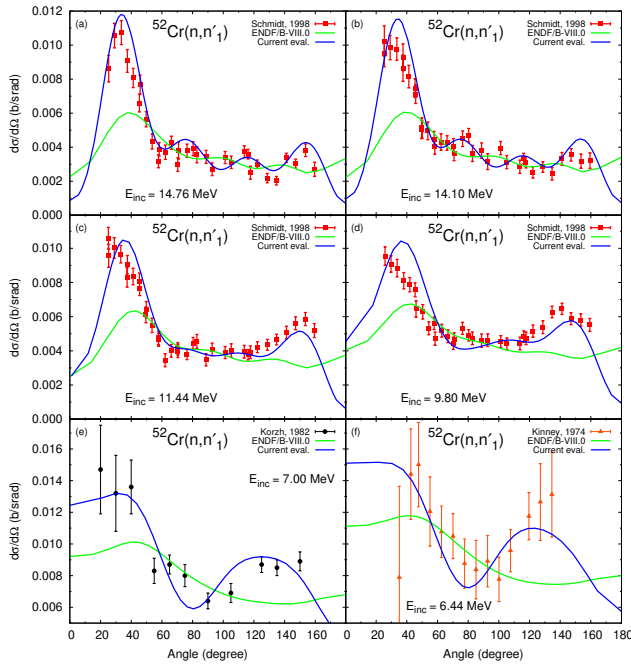


FIG. 38. (color online) $^{52}\text{Cr}(n,n')$ elastic angular cross section in the fast region. Data taken from Refs. [130, 131, 153].

in Sec. IV A 3. The consistently good agreement achieved and exemplified in Fig. 25 and Figs. 26 and 27 certainly contributed to the gamma spectra agreement in that energy range. A noteworthy exception is the gap in the spectra seen at ~ 300 keV gamma energy. The cause of this may be due to transitions that have not been properly described but it has not been fully investigated yet. We leave this for a future work.

For higher energy gammas, but below the neutron incident energy, the current evaluation also is in much better agreement with the data than ENDF/B-VIII.0. Outgoing gammas with energies above the incident neutron energy, which correspond to transitions in the compound nucleus, are well described more or less equally well by both the current evaluation and ENDF/B-VIII.0, being slightly underestimated in a few cases. These are due to capture processes and the accurate description of capture cross section in the fast neutron region is hindered by the lack of experimental data (see Sec. IV A 4).

V. VALIDATION

A. Criticality Benchmarks

Testing of chromium data on criticality benchmarks is important, since it has implications on criticality safety, as well as on design optimization of new types of reactors. In most cases chromium does not appear alone. Usually it is alloyed in stainless steel, which is a common structural material. Data testing therefore includes cases with a

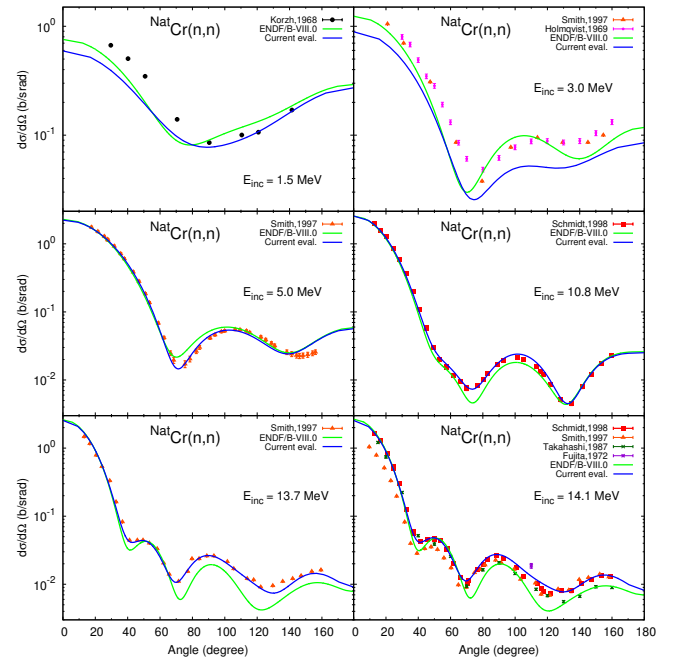


FIG. 39. (color online) $^{\text{Nat}}\text{Cr}(n,n)$ elastic angular distribution cross section in the fast region. Data taken from Refs. [132, 134, 138, 153, 196, 197].

significant content of stainless steel.

The selection of benchmarks from the ICSBEP Handbook was based on previous work reported by various authors [204], and especially on the sensitivity searches in the **DICE system** of the NEA Data Bank [205]. We converged on 22 cases, which are expected to have sensitivity to chromium. The list is given in Table XIII. There is only one benchmark dedicated specifically to testing chromium data, namely the Russian k_{∞} measurement in the KBR facility (KBR-15). Other benchmarks mainly involve chromium is stainless steel (labeled as “SS” in Table XIII) used either as cladding or a reflector.

One of the objectives in nuclear data evaluation is the condition that a new evaluation does not degrade the overall performance of a library. Of course it is possible that an inferior/older evaluation performs better in certain cases due to cancellation of errors in combination with other materials, but such cases need to be looked at very carefully. In particular, it is well known (and acknowledged in the main reference describing the ENDF/B-VIII.0 library) that the iron evaluations have some deficiencies and improved evaluations developed within the INDEN collaboration of the IAEA [206] are available. Similarly, improvements to the silicon evaluations have been made and are also available from the INDEN web page. Thus, the new chromium evaluations were tested together with the new iron and silicon evaluations. The results for libraries were compared and are identified by labels as follows:

- INDEN Chromium, iron, silicon, and oxygen evalua-

TABLE XIII. List of benchmarks from the ICSBEP Handbook selected for the validation of chromium data.

No.	ICSBEP Label	Short name	Common name	Comment
1	HEU-COMP-INTER-005	hci005-009	KBR-09(SS)	k_∞
2	HEU-COMP-INTER-005	hci005-010	KBR-10(Mo)	k_∞
3	HEU-COMP-INTER-005	hci005-015	KBR-15(Cr)	k_∞
4	HEU-COMP-THERM-011	hct011-001	RRC-KI-21x21-001	SS _{cladding}
5	HEU-COMP-THERM-011	hct011-002	RRC-KI-21x21-002	SS _{cladding}
6	HEU-COMP-THERM-011	hct011-003	RRC-KI-21x21-003	SS _{cladding}
7	HEU-COMP-THERM-012	hct012-001	RRC-KI-18x18-001	SS _{cladding}
8	HEU-COMP-THERM-012	hct012-002	RRC-KI-18x18-002	SS _{cladding}
9	HEU-COMP-THERM-013	hct013-001	RRC-KI-14x14-001	SS _{cladding}
10	HEU-COMP-THERM-013	hct013-002	RRC-KI-14x14-002	SS _{cladding}
11	HEU-COMP-THERM-014	hct014-001	RRC-KI-10x10-001	SS _{cladding}
12	HEU-COMP-THERM-014	hct014-002	RRC-KI-10x10-002	SS _{cladding}
13	HEU-COMP-THERM-022	hct022-001	SPERT-III	SS _{cladding}
14	HEU-MET-INTER-001	hmi001	ZPR-9/34	SS _{reflector}
15	HEU-MET-INTER-001	hmi001d	ZPR-9/34	SS _{reflector}
16	HEU-MET-THERM-016	hmt016	LACEF/Ni-Cr-Mo-Gd	
17	IEU-COMP-THERM-005	ict005	KBR-21	k_∞
18	LEU-SOL-THERM-012	lst012-001	TRACY-203c	
19	MIX-COMP-FAST-001	mcf001	ZPR-6/7	
20	MIX-MET-FAST-008	mmf008-003	ZEBRA-8C/2	k_∞
21	PU-MET-INTER-002	pmi002	ZPR-6/10	SS _{reflector}

tions from INDEN, the rest from ENDF/B-VIII.0

- **Cr-BROND** Chromium evaluations from BROND-3.1 [13], iron, silicon, and oxygen evaluations from INDEN, the rest from ENDF/B-VIII.0
- **e80** All materials from ENDF/B-VIII.0
- **jeff33** All materials from JEFF-3.3
- **e71** All materials from ENDF/B-VII.1

The BROND-3.1 [13] evaluations of chromium isotopes have a significantly enhanced capture in the cluster of resonances near 5 keV, mainly from $^{50,53}\text{Cr}$, linked to a much larger thermal capture as discussed in the Introduction. The evidence for the enhancement were the preliminary results of the measurements by Guber et al. [4]. A lot of effort was invested to find a solution that would respect experimental data measured by several authors and provide good performance in the simulations of integral experiments. The results for the selected list of benchmarks are shown in Figure 43. The Chi-squared per degree of freedom (χ^2/DoF) is shown in Figure 44. The figure shows that compared to ENDF/B-VIII.0 the χ^2/DoF is reduced by more than a factor of two when the INDEN evaluations are used and is similar to what achieved with chromium from BROND-3.1.

The BROND-3.1 evaluation [13] showed the best performance for the KBR-15 benchmark, but in our opinion, for the wrong reason. In fact, BROND-3.1 is not the best for the other two KBR benchmarks involving stainless steel and a molybdenum alloy. Additionally, the BROND-3.1 evaluation is performing significantly worse than the current work for the HCT benchmarks from the

Kurchatov institute (RRC-KI) which are highly sensitive to the chromium thermal capture, which is an evidence that the thermal capture of BROND-3.1 is overestimated.

The current INDEN evaluation is off for the KBR-15 benchmark by 4000 pcm, but this is still a reduction of the discrepancy with pure ENDF/B-VIII.0 data by a factor of three. Note that the results for ENDF/B-VII.1, JEFF-3.3 and ENDF/B-VIII.0 are out of scale for this benchmark. It must be borne in mind that k_∞ measurements are extremely sensitive, but they also involve many corrections based on nuclear data, so it is possible that the uncertainty of the reference benchmark value is underestimated. The other big improvement is for the PMI002 (ZPR-6/10) benchmark, which has been a notorious outlier for a long time. With the current INDEN evaluations the predicted PMI002 reactivity is within the uncertainty interval of the measured value. Some improvement is observed also in the reactivity predictions of the thermal benchmarks from the Kurchatov institute (RRC-KI) as discussed above. Other benchmarks do not show large sensitivity to the differences in the evaluations.

B. D-T Neutron Leakage Experiments

In 1980's a series of experiments was performed on the Oktavian facility for benchmarking nuclear data for fusion neutronics [207]. One of the experiments involved a 40 cm diameter chromium sphere with a pulsed D beam incident of a tritiated Ti target that acted as the D-T (fusion) neutron source. Time-of-flight leakage spectrum was measured about 10 m from the target at an angle

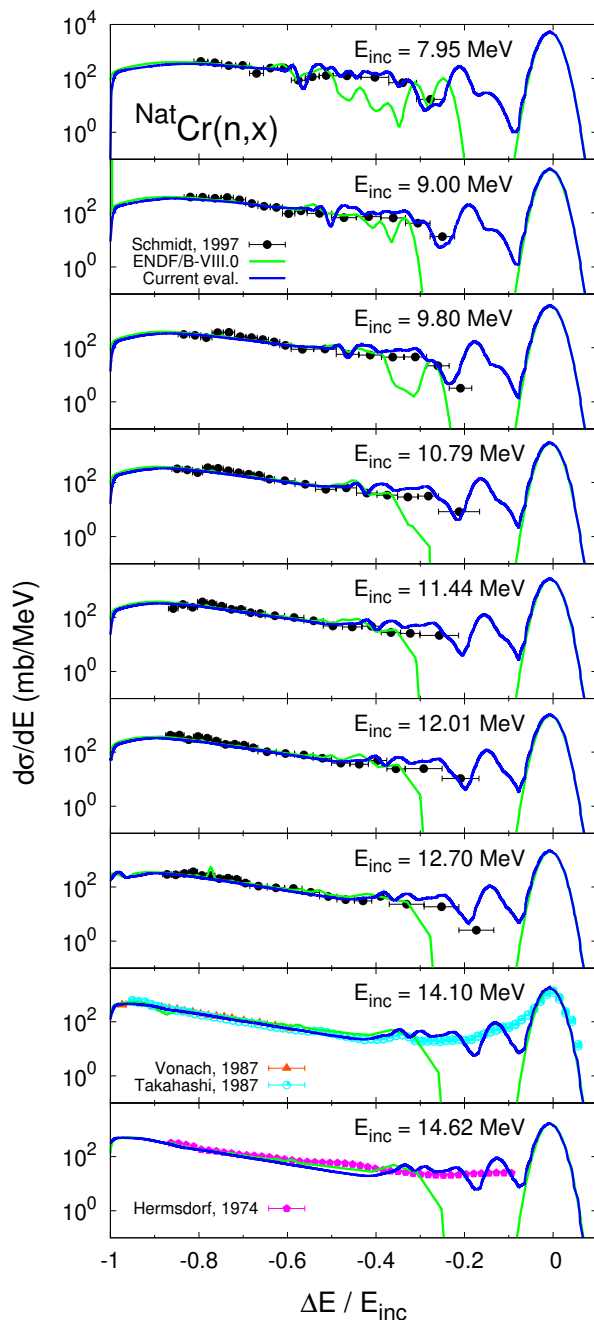


FIG. 40. (color online) Energy-differential spectra for ${}^{\text{Nat}}\text{Cr}(n,x)$, as a function of the normalized energy transfer $\Delta E/E_{\text{inc}}$, where E_{inc} is the incident neutron energy and $\Delta E = E_{\text{out}} - E_{\text{inc}}$ is the difference between the neutron outgoing energy and the incident energy. Experimental data taken from Refs. [196, 198, 199].

of 55 degrees relative to the beam. The source spectrum is given in Table 4.6 of the report. In a companion report [208] the results with different data libraries are presented and a sample computational model for the MCNP Monte Carlo code is given. The source specifications are claimed to be the lethargy spectrum but the units were

"1/MeV/n", which would imply the energy spectrum. By repeating the calculations with the ENDF/B-IV and JENDL-3.2 libraries the plot in Fig. 4.11 of [207] and in Fig. 5.3.9 of [208] the interpretation of the spectra was affirmed.

The computational model for MCNP in [208] is very simple, with the measured neutron spectrum for the source and the surface leakage current spectrum for the tally. A more detailed model was designed that took the sphere geometry accurately into account and the source was modeled from first principles by explicitly modeling the target, taking into account the angle and energy distribution of the neutrons from the D-T reaction. The approach followed closely the one applied by Milocco et al. [209] for the analysis of other Oktavian benchmarks in the SINBAD data base. The detector was modeled as a point-detector about 9 m from the target and at an angle of 55 degrees. Gaussian resolution-broadening of the source was done within MCNP assuming 7 ns pulse width at half maximum to approximately take into account the finite pulse width and other effects in the measuring system.

Spectrum tally in the detector was collected in the time-domain and converted to energy spectrum externally with the ACEFLX code available locally. The conversion would be exact if the time offset and the flight path with which the measured ToF spectrum was converted into the energy spectrum. Since this information is not known exactly we took the library to use time offset of 4 ns and flight path of 9.1 m using relativistic kinematics.

Calculations were performed with the ENDF/B-VIII.0 library and with a modified library that included the new chromium evaluations. The results are presented in Fig. 45. The figure shows excellent agreement in the energy range 0.25-0.6 MeV with both libraries. In the energy range 0.6-1.1 MeV the new INDEN evaluation is distinctly better. Between 1.1 MeV and 2 MeV some discrepancy is seen, which is much smaller with the INDEN evaluation. Above 2 MeV both evaluations lie within the experimental uncertainty, INDEN being slightly closer to the mean of the measured values. The converse is true between 4 MeV and 9 MeV. Above 9 MeV the discrepancies are larger, but these could be to the assumptions in modeling the target assembly, the resolution function, as well as the nuclear data.

C. CEA Pile-oscillation Experiments in MINERVE Reactor

The collaboration group at the CEA/DEN/CAD/DER/SPRC/Laboratoire d'Études de Physique in Cadarache, France, has developed an experimental program entitled MAESTRO [22] for the validation of thermal capture cross sections of structural and moderating materials using pile-oscillation experiments in the MINERVE reactor. The experiment

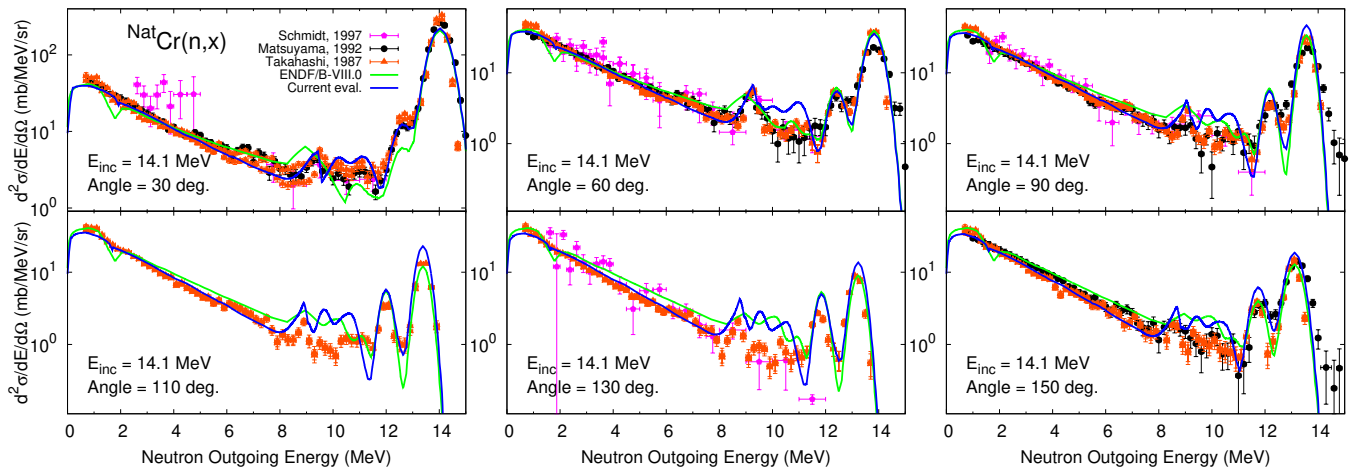


FIG. 41. (color online) Double-differential spectra cross sections for 14.1 MeV incident neutrons on ^{Nat}Cr as a function of the neutron outgoing energy at different scattering angles. Resolution broadening was applied to visually match resolution of the spectra data. Experimental data taken from Refs. [196, 198, 201].

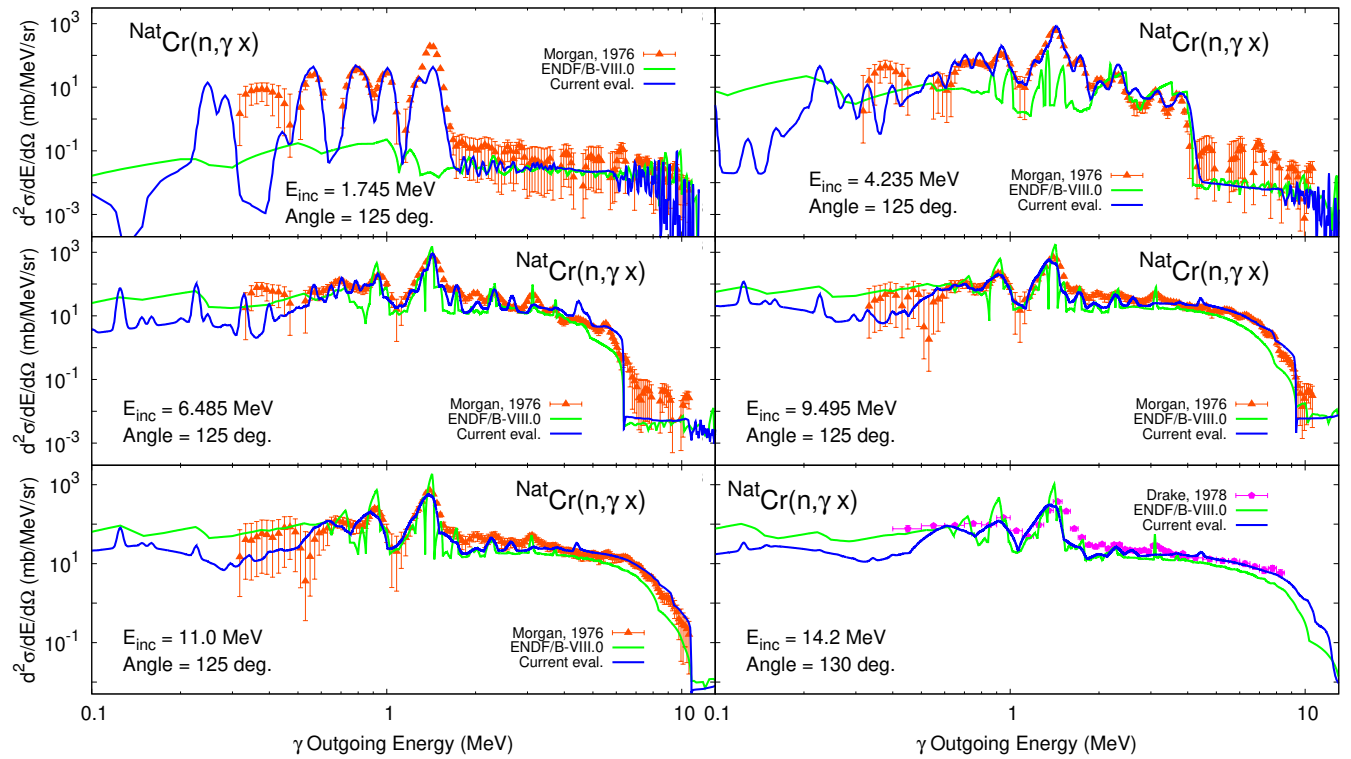


FIG. 42. (color online) Double-differential spectra for gamma production cross sections for a variety of neutron incident energies on ^{Nat}Cr at the fixed scattering angle of 125 degrees, except for $E_{inc} = 14.2$ MeV which is presented for 130 degrees, as a function of the outgoing γ energy. Resolution broadening was applied to visually match resolution of the spectra data. Experimental data taken from Refs. [202, 203].

consisted of oscillating small samples in a critical MINERVE reactor core and measuring the response function (namely the reactivity worth) of the sample. Note that the sensitivity was maximized for thermal neutrons and rapidly decreased for higher energy neutrons; a very low sensitivity to the keV region was

determined. Among structural materials of interest pile-oscillation measurements were undertaken in MAESTRO Phase III (2013-2014) on natural chromium and iron samples. Pure rods of Fe and Cr materials were used in those experiments. Very accurate metrology of the dimensions ($\pm 10\mu\text{m}$) and mass ($\pm 10\text{mg}$) were

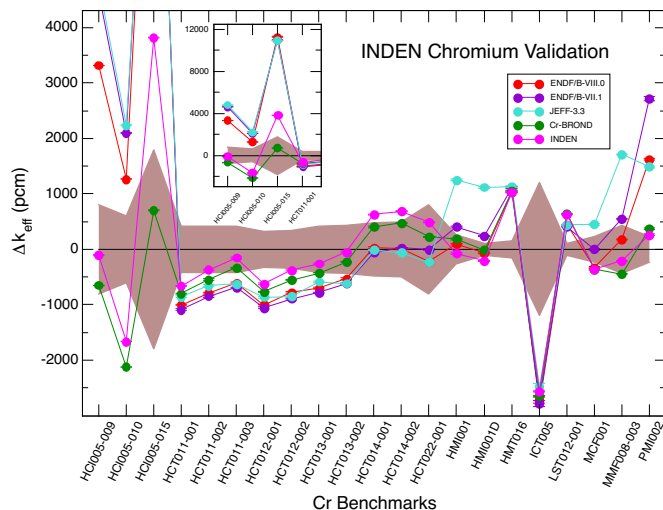


FIG. 43. (color online) Comparison of the differences from the reference benchmark values using different data libraries. Details of each calculation are discussed in text.

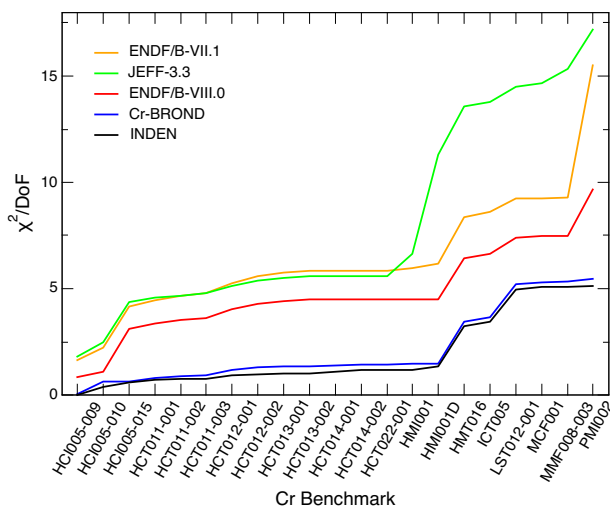


FIG. 44. (color online) Cumulative Chi-squared per degree of freedom for the selected list of benchmarks. Details of each calculation are discussed in text.

undertaken [22]. Void (dummy) samples were used to cancel the reactivity worth due to the cladding. The measurement reactivity uncertainty of ± 0.01 pcm was achieved due to design improvements [22].

A 3D detailed full core model of the MINERVE reactor was implemented using TRIPOLI Monte Carlo model allowing to reach agreement within 3.4% of the measured actinide fission and capture reaction rates $^{238}\text{U}(n,f)/^{235}\text{U}(n,f)$, $^{237}\text{Np}(n,f)/^{235}\text{U}(n,f)$, $^{239}\text{Pu}(n,f)/^{235}\text{U}(n,f)$, $^{240}\text{Pu}(n,\gamma)/^{239}\text{Pu}(n,f)$, and $^{242}\text{Pu}(n,\gamma)/^{239}\text{Pu}(n,f)$ in the central position of the

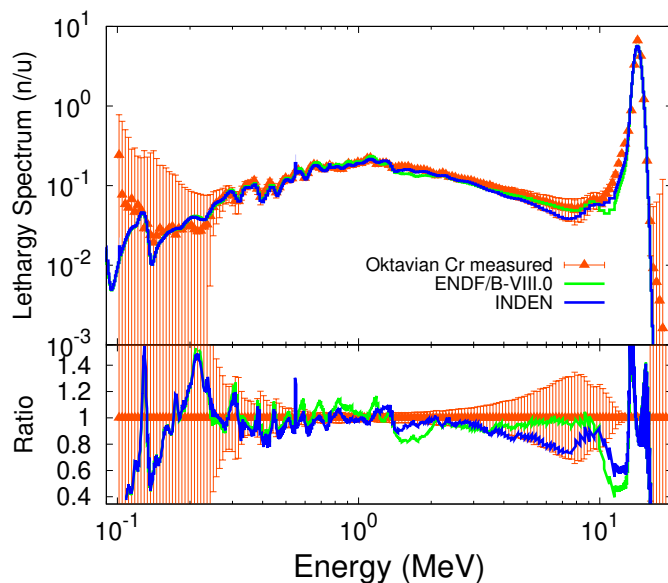


FIG. 45. (color online) Leakage spectrum from the Okta-vian Cr sphere with a D-T source. Calculated spectra with ENDF/B-VIII.0 and the new INDEN evaluation for chromium are compared to measured data.

MINERVE core using the JEFF-3.2 transport library. This is the same position used to measure the samples of interest and these reaction rate measurements validate the calculated neutron flux at that location.

Results of measurements for chromium and iron samples gave (C/E -1) of $-0.5(\pm 1.1)\%$ and $+0.3(\pm 1.2)\%$, respectively using JEFF-3.2 transport library as documented in Ref. [22]. A sample of stainless steel 316L (SS316L) that contains about 18% of chromium and 64% of iron gave (C/E -1) of $-0.7(\pm 1.1)\%$ [22], whilst a sample of stainless steel 304L (SS304L) that contains about 19% of chromium and 68% of iron gave (C/E -1) of $+0.3(\pm 1.1)\%$ [22].

As can be seen in Table III, the thermal capture on natural chromium in this evaluation increased by 0.11 barn compared to JEFF-3.2⁴, a 0.35% increase driven by thermal capture increase in ^{53}Cr . Therefore, an estimated MAESTRO (C/E-1) value for natural chromium will improve benchmark result to $-0.15(\pm 1.1)\%$. There is an estimated reactivity worth for the SS316L sample of only $+0.06\%$ due to the increased thermal capture of natural chromium resulting in an updated (C/E-1) value of $-0.64(\pm 1.1)\%$ for SS316L, which is still acceptable within the quoted experimental benchmark uncertainties. The estimated reactivity worth for the SS304L sample is $+0.07\%$ due to the increased thermal capture of natural chromium resulting in an updated (C/E-1) value of

⁴ The resonance evaluation of chromium isotopes in ENDF/B-VIII.0 is identical to the evaluation in JEFF-3.2

+0.37(\pm 1.1)% for SS304L, which is also acceptable within the quoted experimental benchmark uncertainties.

The 7% decrease of the thermal capture in ^{56}Fe from 2.586 b in JEFF-3.2 to 2.396 b in the INDEN evaluation (as suggested by Firestone *et al.* [19]) is estimated to decrease the (C/E-1) of the natural iron by -6.4% resulting in an updated (C/E-1) value of -6.1(\pm 1.1)% for the MAESTRO benchmark. Such large decrease in the (C/E-1) clearly rejects the proposed reduction of the thermal capture on natural iron. A similar rejection trend is observed for experimental values of SS316L and SS304L stainless-steel samples.

In summary, MAESTRO benchmark results are fully compatible with new chromium evaluations presented in this work. The evaluation trend of increasing thermal capture is confirmed and improves the already good benchmark performance for thermal neutron capture on natural chromium. However, the proposed decrease of the thermal capture of ^{56}Fe as suggested by Firestone *et al.* [19] cannot be supported by the MAESTRO benchmark as measurements on three independent samples (Fe, SS304L, and SS316L) rejected the proposed change.

Future additional validation may be provided by a new benchmark experiment being developed by CEA/EPLP collaboration, the PETALE neutron transmission experiment [210] which data acquisition concluded in September 2020. PETALE is being performed at the EPFL/CROCUS facility (Lausanne, Switzerland), and first results are expected in 2021. This transmission experiment will, indeed, help to validate the elastic and inelastic cross sections for Cr, Fe and Ni elements, independently, as it consists of transmission through purely isotopic blocks of the aforementioned structural materials.

VI. CONCLUSIONS AND RECOMMENDATIONS

In the resolved resonance region, particularly in the cluster of *s*-wave resonances of the $^{50,53}\text{Cr}$ isotopes, this work has clarified and unraveled some of the most relevant issues related to the measured and evaluated data with particular focus to the deficiencies of the ENDF/B-VIII.0 library.

Regarding the measured data, this work showed that the normalization of the neutron capture yield is of fundamental importance and in the case of data sets from Stieglitz *et al.* and Guber *et al.* reported in the EXFOR library, the adopted normalization (i.e., by the inverse of the thickness) is the incorrect choice as shown in Figs. 4 and 3. In general, the measured data should be both reported as neutron capture yield data and checked for the correct normalization. Moreover, for nuclei with large total cross section, the capture measurements should be designed with the proper thickness sample to minimize the self shielding effects and multiple-scattering corrections.

Although the large discrepancy between oxide enriched data sets from Stieglitz *et al.* and Guber *et al.* was not directly resolved, a correction of about 3% to the thickness of the data from Guber *et al.* was found and the corrected value used in the current evaluation. Also, the fit of capture yield data from Guber *et al.* measured on metal natural sample showed remarkable consistency with oxide enriched data from Stieglitz *et al.* as shown in Figs. 5–7. This implies that the ^{53}Cr oxide enriched data from Guber *et al.* are affected by a normalization issue.

Regarding the evaluated data, a new set of resonance parameters was derived by the fit of capture yield data measured on metal natural sample and reported in Tab. II. Direct capture was shown to play an important role in the resonance evaluation of near magic nuclei like chromium isotopes.

Monte Carlo simulations revealed some inconsistency in describing the multiple scattering corrections for the cases of oxide-enriched samples, for which the multiple scattering corrections are large, and a careful choice between the finite size and infinite slab approximation should be performed. Additional work and numerical simulations as well as possible corrections to the algorithm to compute the multiple scattering corrections with defined approximations are planned as future updates to the SAMMY code. Further verification of multiple scattering corrections used in SAMMY code and comparison to MCNP-calculated multiple scattered corrections are warranted.

The fit of ^{50}Cr measured data was performed for the time being in finite size approximation; a revised set of resonance parameters is needed as soon as the multiple scattering corrections can be described properly. These updates might also clarify the problem with alignment of the measured data in the cluster of *s*-wave resonances.

The currently evaluated ^{53}Cr resonance integral value is higher than the value reported in the ENDF/B-VIII.0 library, which is consistent with Mughabghab Atlas 2017 evaluated value. However, the current evaluated RI is still more than a barn lower than the value reported by BROND-3.1 (11.19 b) and Stieglitz’s thesis (10.75 b). The overestimated resonance integral value for BROND-3.1 is related to the overestimated thermal capture cross section and the assumptions on the fitted cross sections in the *s*-wave cluster of resonances. For Stieglitz, the value of the resonance integral can be calculated by the infinite dilution formula as in Eq. (119) of Stieglitz’s thesis together with the reported resonance parameters. However, in that equation it is unclear the quantity “M” defined as “reduced mass of neutron” contrary to the ANL report [211] where the equation was taken from and that quantity was defined as the neutron mass.

Complete reevaluations of the fast-region reaction for all stable chromium isotopes were performed taking into account new data (e.g., inelastic, (n,p) reactions) and new modeling (e.g. soft-rotor coupled-channel optical potential), leading to substantial improvement in the description of experimental data for angle-integrated cross sections.

tions, angular distributions, energy spectra, and neutron and gamma double-differential spectra.

The new chromium evaluations combined with proposed INDEN iron evaluations were benchmarked with MCNP simulations of a small suite of critical assemblies sensitive to natural chromium and iron data and with the Oktavian chromium shielding benchmark. Considerable performance improvements were observed both for critical assemblies and the shielding experiment. Thermal capture values of chromium and iron INDEN evaluations were benchmarked with the CEA MAESTRO pile-oscillation experiments. The chromium evaluations show small improvement in the observed C/E trend well within the quoted uncertainties. However, the proposed 7% decrease of the thermal capture in natural iron⁵ is rejected by CEA MAESTRO pile-oscillation measurements.

Despite the significant advances in evaluated data and documented performance improvements of the proposed chromium evaluations, the authors would like to remark that there are outstanding issues that still need to be addressed in a future work: a) A dispersive coupled-channel optical model needs to be improved below 4 MeV of neutron incident energy. b) The modeling description of measured inelastic gammas as shown in Fig. 25 should be improved. Important work has been recently published

in modeling of the $^{57}\text{Fe}(n,n'\gamma)$ [212] that could serve as a template for such improvement. c) The high energy part of the resolved resonance region and capture in particular can be improved. d) Additional work is needed on the evaluated resonance integrals of $^{50,53}\text{Cr}$ isotopes. e) Capture gamma spectra of thermal neutrons in iron and chromium need to be reevaluated to address issues recently raised by Mauborgne *et al.* [213].

ACKNOWLEDGMENTS

Authors would like to acknowledge G. Noguere for very productive discussions and exchange of information. Work at Brookhaven National Laboratory was sponsored by the Office of Nuclear Physics, Office of Science of the U.S. Department of Energy under Contract No. DE-AC02-98CH10886 with Brookhaven Science Associates, LLC. ORNL is managed by UT-Battelle, LLC, for the U.S. Department of Energy under Contract No. DE-AC05-00OR22725. The U.S. Department of Energy Nuclear Criticality Safety Program sponsored the work presented in this paper.

-
- [1] R. L. Klueh and D. R. Harries, “High-chromium ferritic and martensitic steels for nuclear applications: (MONO 3),” in *High-Chromium Ferritic and Martensitic Steels for Nuclear Applications: (MONO 3)* (2001).
- [2] C. Delafoy, J. Bischoff, J. Larocque, P. Attal, L. Gerken, and K. Nimishakavi, “Benefits of FRAMATOME’s E-ATF evolutionary solution: Cr-coated cladding with Cr₂O₃-doped fuel,” in *Proceedings of the 2018 “Top Fuel - Reactor Fuel Performance” Conference*, A0149 (2018).
- [3] V. Pronyaev, “New measurements needed to update JEFF evaluations and remove compensation of the neutron cross sections,” Tech. Rep. JEF/DOC-1525, Nuclear Energy Agency, OECD (2013).
- [4] K. H. Guber, P. E. Koehler, D. Wiarda, and J. A. Harvey, “Neutron cross-section measurements on structural materials at ORELA,” *J. Korean Phys. Soc.* **59**, 1685 (2011).
- [5] L. Leal, H. Derrien, K. Guber, G. Arbanas, and D. Wiarda, “Evaluation of the chromium resonance parameters including resonance parameter covariance,” *J. Korean Phy. Soc.*, 1644 (2011).
- [6] P. Pereslavytsev, A. Konobeyev, U. Fischer, and L. Leal, “Evaluation of ^{50}Cr , ^{52}Cr , ^{53}Cr , ^{54}Cr neutron cross section data for energies up to 200 MeV,” *J. Korean Phy. Soc.*, 931 (2011).
- [7] A. J. M. Plompen, O. Cabellos, C. De Saint Jean, *et al.*, “The Joint Evaluated Fission and Fusion nuclear data library, JEFF-3.3,” *The Eur. Phys. J. A* **56**, 181 (2020).
- [8] D. Brown, M. Chadwick, R. Capote, *et al.*, “ENDF/B-VIII.0: The 8th major release of the nuclear reaction data library with CIELO-project cross sections, new standards and thermal scattering data,” *Nucl. Data Sheets* **148**, 1 (2018).
- [9] M. Chadwick, H. Hughes, R. Little, E. Pitcher, and P. Young, “Nuclear data for accelerator-driven systems,” *Prog. Nucl. Energy* **38**, 179 (2001).
- [10] V. McLane and members of the Cross Section Evaluation Working Group, “ENDF-201, ENDF/B-VI Summary Documentation, Supplement I, ENDF/HE-VI Summary Documentation,” Tech. Rep. BNL-NCS-17541, [ENDF-201], 4th EDITION [ENDF/B-VI] SUPPLEMENT I, National Nuclear Data Center, Brookhaven National Laboratory, Upton, New York (1996).
- [11] J. Bess *et al.*, “International criticality safety benchmark evaluation project.” Nuclear Energy Agency, OECD, Paris, France, [Online] Available at <http://icsbep.inel.gov>.
- [12] Koscheev, Vladimir, Manturov, Gennady, Pronyaev, Vladimir, Rozhikhin, Evgeny, Semenov, Mikhail, and Tsibulya, Anatoly, “Use the results of measurements on kbr facility for testing of neutron data of main structural materials for fast reactors,” *EPJ Web Conf.* **146**, 06025 (2017).
- [13] A. Blokhin, E. Gai, A. Ignatyuk, I. Koba, V. Manokhin, and V. Pronyaev, “New version of neutron evaluated data library BROND-3.1,” *Probl. At. Sci. Technol. Series: Nucl. React. Constants*, 62 (2016). In Russian.
- [14] R. G. Stieglitz, R. W. Hockenbury, and R. C. Block, “keV neutron capture and transmission measurements

⁵ as suggested by Firestone *et al.* [19]

- on ^{50}Cr , ^{52}Cr , ^{53}Cr , ^{54}Cr , ^{60}Ni and V,” Nucl. Physics, Sect. A **163**, 592 (1971).
- [15] R. F. Carlton, J. A. Harvey, D. C. Larson, and N. W. Hill, “Neutron resonance spectroscopy for $n + ^{52}\text{Cr}$: Total and differential elastic scattering cross sections,” Phys. Rev. C **62**, 014608 (2000).
- [16] D. M. Hetrick, D. C. Larson, and C. Y. Fu, “Generation of covariance files for the isotopes of Cr, Fe, Ni, Cu and Pb in ENDF/B-VI,” Tech. Rep. ORNL/TM-11763, Oak Ridge National Laboratory (1991). ENDF Report ENDF-350.
- [17] M. Herman, A. Trkov, R. Capote, *et al.*, “Evaluation of neutron reactions on iron isotopes for CIELO and ENDF/B-VIII.0,” Nucl. Data Sheets **148**, 214 (2018).
- [18] E. Pirovano, R. Beyer, M. Dietz, *et al.*, “Cross section and neutron angular distribution measurements of neutron scattering on natural iron,” Phys. Rev. C **99**, 024601 (2019).
- [19] R. B. Firestone, T. Belgya, M. Krtička, F. Bečvář, L. Szentmiklosi, and I. Tomandl, “Thermal neutron capture cross section for $^{56}\text{Fe}(n, \gamma)$,” Phys. Rev. C **95**, 014328 (2017).
- [20] S. Kwon, M. Ohta, and K. Ochiai, “ENDF/B-VIII β 4 benchmark test with iron and concrete shielding experiments using 40 and 65 MeV neutrons at QST/TIARA,” Fusion Eng. Des. **136**, 2 (2018). Special Issue: Proceedings of the 13th International Symposium on Fusion Nuclear Technology (ISFNT-13).
- [21] C. Konno, K. Ochiai, S. Sato, and M. Ohta, “Analyses of iron and concrete shielding experiments at JAEA/TIARA with JENDL/HE-2007, ENDF/B-VII.1 and FENDL-3.0,” Fusion Eng. Des. **98-99**, 2178 (2015). Proceedings of the 28th Symposium On Fusion Technology (SOFT-28).
- [22] P. Leconte, “Nuclear data feedback on structural, moderating and absorbing materials through the MAESTRO experimental programme in MINERVE,” Tech. Rep. JEF/DOC-1849, Nuclear Energy Agency, OECD, Paris, France (2017).
- [23] Monte Carlo Code Group, “A general Monte Carlo N-particle (MCNP) transport code, version 6.1.” Los Alamos National Laboratory, Los Alamos, NM, USA, [Online] Available at <https://laws.lanl.gov/vhosts/mcnp.lanl.gov/index.shtml>.
- [24] C. Werner (editor), “MCNP users manual - code version 6.2,” Tech. Rep. LA-UR-17-29981, Los Alamos National Laboratory (2017).
- [25] “The Kayzero database,” (2019), <http://www.kayzero.com/>, [Online] Available at http://www.kayzero.com/k0naa/k0naaorg/Nuclear_Data_SC/Nuclear_Data_SC.html.
- [26] S. F. Mughabghab, *Atlas of Neutron Resonances, Vol.1 and 2*. Elsevier, Amsterdam (2018).
- [27] J. R. Dunning, G. B. Pegram, G. A. Fink, and D. P. Mitchell, “Interaction of neutrons with matter,” Phys. Rev. **48**, 265 (1935). EXFOR Entry # 12634.
- [28] M. Goldhaber and G. H. Briggs, “Scattering of slow neutrons,” Proc. Royal Soc. (London), Ser. A **162**, 127 (1937). EXFOR Entry # 22518.
- [29] J. Coltman and M. Goldhaber, “Capture cross sections for slow neutrons,” Phys. Rev. **69**, 411 (1946). EXFOR Entry # 12616.
- [30] S. P. Harris, C. O. Muehlhause, S. Rasmussen, H. P. Schroeder, and G. E. Thomas, “Pile neutron absorption cross sections,” Phys. Rev. **80**, 342 (1950).
- [31] F. C. W. Colmer and D. J. Littler, “Pile neutron absorption cross sections of some of the elements,” Proc. Phys. Soc. (London), Sect. A **63**, 1175 (1950).
- [32] E. H. Bertel Grimeland and F. Aetter, “Mesure par la modulation d’une pile de la section efficace de quelques éléments pour l’absorption des neutrons lents,” Comptes Rendus, Ser. B **232**, 2089 (1951).
- [33] H. Pomerance, “Thermal neutron capture cross sections,” Phys. Rev. **83**, 641 (1951). EXFOR Entry # 11047.
- [34] E. Melkonian, W. W. Havens, Jr, and L. J. Rainwater, “Slow neutron velocity spectrometer studies V, Re, Ta, Ru, Cr, Ga,” Phys. Rev. **92**, 702 (1953).
- [35] Y. A. Prokhorov, *Measurement of the effective cross-sections of neutron absorption in the middle energy range*. PhD thesis, Fiziko-Energeticheskii Inst., Obninsk, Russia (1956). EXFOR Entry # 41648.
- [36] M. Salama, M. Adib, A. Abdel-Kawi, S. El-Miniawy, M. El-Khosht, and I. Hamouda, “Measurements of the total neutron cross section of chromium, cobalt and zirconium in the energy range 3 meV to 1 eV,” Atomkernenergie **22**, 87 (1973). EXFOR Entry # 30468.
- [37] F. Kropff, J. R. Granada, L. A. Remez, and A. Vasile, “Total cross-section of chromium at low neutron energies,” Annals Nucl. Energy **3**, 55 (1976). EXFOR Entry # 30311.
- [38] R. L. Macklin, H. S. Pomerance, *et al.*, “Resonance capture integrals,” in *Proc. U.N. Intern. Conf. Peaceful Uses At. Energy*, **5**, (Geneva) (1955). EXFOR Entry # 14388.
- [39] V. B. Klimentov and V. M. Griazev, “The measurement of the resonance integrals for neutron absorption,” Sov. At. Energy **3**, 1387 (1957). EXFOR Entry # 40368.
- [40] S. P. Kapchigashev and Y. P. Popov, “Capture cross sections for neutrons of energy up to 50 keV for Cr, ^{50}Cr , ^{52}Cr , ^{53}Cr nuclei (E),” Sov. At. Energy **16**, 306 (1964).
- [41] L. Seren, H. N. Friedlander, and S. H. Turkel, “Thermal neutron activation cross section,” Phys. Rev. **72**, 888 (1947).
- [42] H. Pomerance, “Thermal neutron capture cross sections,” Phys. Rev. **88**, 412 (1952). EXFOR Entry # 11507.
- [43] W. S. Lyon, “Reactor neutron activation cross sections for a number of elements,” Nucl. Sci. Eng. **8**, 378 (1960). EXFOR Entry # 11625.
- [44] G. Sims and D. Juhnke, “The thermal neutron cross-sections and resonance integrals of ^{50}Cr , ^{109}Ag , ^{123}Sb , ^{133}Cs , ^{191}Ir and ^{202}Hg ,” J. Inorg. Nucl. Chem. **30**, 349 (1968). EXFOR Entry # 11658.
- [45] G. Gleason, “Thermal neutron cross sections and (n- γ) resonance integrals pt 1,” Radiochem. Radioanal. Lett. **23**, 317 (1975). EXFOR Entry # 10644.
- [46] R. Heft, “A consistent set of nuclear-parameter values for absolute INAA,” in *Proc. of the Am. Nucl. Soc. Topical Conf.* (B. Carpenter *et al.*, eds.), (Mayagüez, Puerto Rico) (1978). EXFOR Entry # 12866.
- [47] L. Koester, K. Knopf, and W. Waschowski, “Interactions of slow neutrons with the chromium isotopes,” Z. fuer Physik A, Hadron. Nucl. **287**, 61 (1978).
- [48] A. Simonits, F. De Corte, L. Moens, and J. Hoste, “Critical evaluation and experimental determination of the nuclear activation and decay parameters for the reac-

- tions: $^{50}\text{Cr}(n,\gamma)^{51}\text{Cr}$, $^{58}\text{Fe}(n,\gamma)^{59}\text{Fe}$, $^{109}\text{Ag}(n,\gamma)^{110m}\text{Ag}$,” J. Radioanal. Nucl. Chem. **81**, 369 (1984). EXFOR Entry # 30677.
- [49] F. De Corte and A. Simonits, “A compilation of accurately measured 2200 m/s cross-sections for 101 n,gamma reactions of interest in activation analysis; a critical comparison with literature,” in *Conf. on Nucl. Data For Sci. and Technol., Mito 1988*, 583 (1988). EXFOR Entry # 23488.
- [50] L. Venturini and B. Pecequilo, “Thermal neutron capture cross-section of ^{48}Ti , ^{51}V , $^{50,52,53}\text{Cr}$ and $^{58,60,62,64}\text{Ni}$,” Appl. Radiat. Isot. **48**, 493 (1997). EXFOR Entry # 31489.
- [51] F. Farina Arbocco, P. Vermaercke, K. Smits, L. Sneyers, and K. Strijckmans, “Experimental determination of K_0 , Q_0 factors, effective resonance energies and neutron cross-sections for 37 isotopes of interest in NAA,” J. Radioanal. Nucl. Chem. **302**, 655 (2014). EXFOR Entry # 23260.
- [52] F. De Corte, A. Speecke, and J. Hoste, “Activation analysis of high-purity silicon,” J. Radioanal. Chem. **9**, 9 (1971).
- [53] R. Van der Linden, F. De Corte, P. Van den Winkel, and J. Hoste, “A compilation of infinite dilution resonance integrals, I,” J. Radioanal. Chem. **11**, 133 (1972). EXFOR Entry # 20643.
- [54] L. Sage and A. Furr, “Measurement of some resonance integrals,” Trans. Am. Nucl. Soc. **23**, 501 (1978). EXFOR Entry # 10637.
- [55] K. Shibata, O. Iwamoto, T. Nakagawa, *et al.*, “JENDL-4.0: A new library for nuclear science and engineering,” J. Nucl. Sci. Technol. **48**, 1 (2011).
- [56] I. Dillmann, R. Plag, F. Käppeler, and T. Rauscher, “Kadonis v0.3 - the third update of the “Karlsruhe Astrophysical Database of Nucleosynthesis in Stars,”” in *EFNUDAT Fast Neutrons - scientific workshop on neutron measurements, theory and applications*, (Geel, Belgium) (2009). <http://www.kadonis.org/>.
- [57] B. Allen, J. Gibbons, and R. Macklin, “Nucleosynthesis and neutron-capture cross sections,” in *Advances in Nuclear Physics*, **4**, ch. 4, 205, New York: Plenum Press (1971).
- [58] H. Beer, R. R. Spencer, and A. Ernst, “The s-process near the iron seed - some improved capture cross sections,” Astron. Astrophys. **37**, 197 (1974).
- [59] H. Beer and R. R. Spencer, “keV neutron radiative capture and total cross section of $^{50,52,53}\text{Cr}$, $^{54,57}\text{Fe}$, and $^{62,64}\text{Ni}$,” Nucl. Phys. A **240**, 29 (1975).
- [60] M. J. Kenny, B. J. Allen, A. R. de L. Musgrove, R. L. Macklin, and J. Halperin, “Neutron capture by the chromium isotopes,” Tech. Rep. AAEC/E-400, Australian Atomic Energy Commission Research Establishment (1977).
- [61] G. Rohr, R. Shelley, A. Brusegan, F. Poortmans, and L. Mewissen, “Nonstatistical effects observed with $^{52}\text{Cr} + n$ resonances,” Phys. Rev. C **39**, 426 (1989).
- [62] S. P. Harris, C. O. Muehlhause, and G. E. Thomas, “Low energy neutron resonance scattering and absorption,” Phys. Rev. **79**, 11 (1950).
- [63] G. A. Bazorgan, J. W. Irvine, J. , and C. D. Coryell, “Preparation and half-life of ^{55}Cr ,” Phys. Rev. **95**, 781 (1954). EXFOR Entry # 12592.
- [64] D. H. White and R. E. Howe, “Gamma-Ray Spectra and Level Structure of ^{55}Cr from Thermal Neutron Capture in ^{54}Cr ,” Nucl. Physics, Sect. A **187**, 12 (1972). EXFOR Entry # 10429.
- [65] W. E. Parker, M. B. Chadwick, F. S. Dietrich, *et al.*, “Fluctuation effects in radiative capture to unstable final states: A test via the $^{89}\text{Y}(p\rightarrow,\gamma)$ reaction at $E_p=19.6$ MeV,” Phys. Rev. C **52**, 252 (1995).
- [66] G. Arbanas, F. S. Dietrich, and A. K. Kerman, “Direct-semidirect neutron capture calculations applied to R-Matrix data evaluations in the resolved resonance region,” AIP Conf. Proc. **769**, 296 (2005).
- [67] N. M. Larson, “Updated user’s guide for Sammy: Multilevel R-matrix fits to neutron data using Bayes’ equations,” Tech. Rep. ORNL/TM-9179/R8, ENDF-364/R2, Oak Ridge National Laboratory (2008).
- [68] H.-D. Meyer and K. Tang, “s wave resonances with square well potentials,” Z. für Physik A Atoms Nucl. **279**, 349 (1976).
- [69] K. Bear and P. E. Hodgson, “The systematics of nuclear bound states,” J. Phys. G: Nucl. Phys. **4**, L287 (1978).
- [70] E. Krausmann, W. Balogh, H. Oberhammer, T. Rauscher, K.-L. Kratz, and W. Ziegert, “Direct neutron capture for magic-shell nuclei,” Phys. Rev. C **53**, 469 (1996).
- [71] Y. Xu and S. Goriely, “Systematic study of direct neutron capture,” Phys. Rev. C **86**, 045801 (2012).
- [72] P. David, H. Duhm, R. Bock, and R. Stock, “ $(^3\text{He},\alpha)$ reactions on the chromium isotopes,” Nucl. Phys. A **128**, 47 (1969).
- [73] H. Xiaolong, “Nuclear Data Sheets for $A = 51$,” Nucl. Data Sheets **107**, 2131 (2006).
- [74] J. Kopecky, R. Chrien, and H. Liou, “Resonance neutron capture in ^{52}Cr ,” Nucl. Phys. A **334**, 35 (1980).
- [75] J. Beene, “Nuclear data sheets for $A = 52$,” Nucl. Data Sheets **25**, 235 (1978).
- [76] G. Brown, A. Denning, and A. Macgregor, “Spectroscopic factors for $l_n = 1$ and $l_n = 3$ transitions in (d,p) reactions with some calcium and chromium nuclei,” Nucl. Phys. A **153**, 145 (1970).
- [77] H. Junde and H. Su, “Nuclear Data Sheets for $A = 54$,” Nucl. Data Sheets **107**, 1393 (2006).
- [78] A. Macgregor and G. Brown, “A study of the $^{54}\text{Cr}(d,p)^{55}\text{Cr}$ and $^{53}\text{Cr}(t,p)^{55}\text{Cr}$ reactions,” Nucl. Phys. A **198**, 237 (1972).
- [79] H. Junde, “Nuclear Data Sheets for $A = 55$,” Nucl. Data Sheets **109**, 787 (2008).
- [80] R. F. Carlton, C. Baker, and J. A. Harvey, “High-resolution transmission measurements for $^{54}\text{Cr} + n$,” Phys. Rev. C **74**, 044614 (2006).
- [81] W. P. Abfalterer, F. B. Bateman, F. S. Dietrich, R. W. Finlay, R. C. Haight, and G. L. Morgan, “Measurement of neutron total cross sections up to 560 MeV,” Phys. Rev. C **63**, 044608 (2001).
- [82] W. Abfalterer, F. Bateman, F. Dietrich, R. Finlay, R. Haight, and G. Morgan, “Measurement of neutron total cross sections up to 600 MeV in support of the APT program,” Tech. Rep. LA-UR-99-0666, Los Alamos National Laboratory (1999).
- [83] W. Abfalterer, R. Haight, G. Morgan, F. Bateman, F. Dietrich, and R. Finlay, “Measurement of neutron total cross sections in support of the APT program,” Tech. Rep. LA-UR-98-4231, Los Alamos National Laboratory (1998).
- [84] F. Perey, T. Love, and W. Kinney, “Test of neutron total cross-section evaluations from 0.2 to 20 MeV for C, O,

- Al, Si, Ca, Fe, and SiO₂,” Tech. Rep. 4823, Oak Ridge National Laboratory (1972).
- [85] F. Perey, T. Love, and W. Kinney, “EXFOR entry #10342.” Private communication (1973).
- [86] H. M. Agrawal, J. B. Garg, and J. A. Harvey, “Parity dependence of the level densities of ⁵³Cr and ⁵⁵Cr at high excitation,” *Phys. Rev. C* **30**, 1880 (1984).
- [87] V. Zerkin and B. Pritychenko, “The experimental nuclear reaction data (exfor): Extended computer database and web retrieval system,” *Nucl. Inst. Meth. Phys. Res. Sect. A: Accel. Spectrometers, Detect. Assoc. Equip.* **888**, 31 (2018).
- [88] C. T. Hibdon, “Neutron total cross sections of chromium and iron in the keV region,” *Phys. Rev.* **108**, 414 (1957).
- [89] C. Hibdon, “Neutron cross sections in the keV region,” Progress Report 5554, Argonne National Laboratory (1956).
- [90] J. F. Whalen and J. W. Meadows, “Fast neutron total cross sections using a mono-energetic source and an automated facility,” Progress Report 7210, Argonne National Laboratory (1966).
- [91] J. Cabe, M. Laurat, P. Yvon, and G. Bardolle, “Search for an intermediate structure in neutron total cross sections (in french),” *Nucl. Physics, Sect. A* **102**, 92 (1967).
- [92] J. Cabe, M. Laurat, and P. Yvon, “Contribution to the study of the nuclear structure using neutron cross-section measurements between 400 keV and 1200 keV. isolated resonances and intermediate structure. (in French),” Tech. Rep. 3279, Centre d’Etudes Nucleaires, Saclay (1967).
- [93] M. Bormann, “Report from Euratom-countries + Euratom to EANDC,” Progress Report 76, CEA/DAM Ile-de-France, Bruyeres-le-Chatel, Arpajon, France (1967).
- [94] J. Cabe, M. Laurat, P. Yvon, and G. Bardolle, “Report from Euratom-countries + Euratom to EANDC,” Progress Report 57, CEA/DAM Ile-de-France, Bruyeres-le-Chatel, Arpajon, France (1965).
- [95] S. Cierjacks, P. Forti, D. Kopsch, L. Kropp, J. Nebe, and H. Unseld, “High resolution total neutron cross-sections between 0.5-30 MeV,” Tech. Rep. 1000, Kernforschungszentrum Karlsruhe (1968).
- [96] S. Cierjacks, P. Forti, D. Kopsch, L. Kropp, J. Nebe, and H. Unseld, “High resolution total neutron cross-sections between 0.5-30 MeV,” Tech. Rep. 3963, Euratom (1968).
- [97] S. Cierjacks, P. Forti, D. Kopsch, L. Kropp, J. Nebe, and H. Unseld, “High resolution total neutron cross-sections between 0.5-30 MeV,” Tech. Rep. 111, Euratom (1968). Report from Euratom-countries + Euratom to EANDC.
- [98] S. Cierjacks, P. Forti, D. Kopsch, L. Kropp, J. Nebe, and H. Unseld Private communication (1970).
- [99] D. G. Foster Jr. and D. W. Glasgow, “Neutron total cross sections, 2.5 - 15 MeV. I. Experimental,” *Phys. Rev. C* **3**, 576 (1971).
- [100] L. Green and J. Mitchell, “Total cross section measurements with a ²⁵²Cf time of flight spectrometer,” Tech. Rep. 1073, Westinghouse Atomic Power Division (1973).
- [101] L. Green and J. Mitchell, “Total cross section measurements with a ²⁵²Cf time of flight spectrometer,” in *3rd Conference on Neutron Cross-Sections and Technology*, **1**, (Knoxville, TN, USA), 325 (1971).
- [102] D. Larson, J. Harvey, and N. Hill, “Measurement of neutron total cross sections at ORELA to 80 MeV,” in *Symposium on Neutron Cross Sections for 10-50 MeV*, (Brookhaven, NY, USA), 277 (1980).
- [103] D. Larson, J. Harvey, and N. Hill, “Measurement of neutron total cross sections at ORELA to 80 MeV,” Progress Report 5787, Oak Ridge National Laboratory (1981).
- [104] J. A. Farrell, E. G. Bilpuch, and H. W. Newson, “s and p wave neutron spectroscopy. Part XI a. Level spacings in even intermediate elements,” *Annals Phys. (New York)* **37**, 367 (1966).
- [105] R. Spencer, H. Beer, and F. Froehner, “The total neutron cross sections of ⁵⁰Cr, ⁵²Cr, ⁶²Ni and ⁶⁴Ni in the energy region 10 - 300 keV,” tech. rep., Institut für Angewandte Kernphysik (IAK) (1972). KFK-1517 (November 72) EANDC(E) 146 'AL'.
- [106] G. Rohr, R. Shelley, A. Brusegan, F. Poortmans, and L. Mewissen, “Nonstatistical effects observed with ⁵²Cr + n resonances,” in *Conference on Nuclear Data For Science and Technology*, (Mito, Japan), 779 (1988).
- [107] K. N. Muller and G. Rohr, “Strength function fluctuations in the mass region of the 3s resonance,” *Nucl. Physics, Sect. A* **164**, 97 (1971).
- [108] K.-N. Muller and G. Rohr in *Nuclear Data for Reactors Conference*, **1**, (Helsinki, Finland), 619 (1970).
- [109] K.-N. Muller and G. Rohr Tech. Rep. 1114, Kernforschungszentrum Karlsruhe (1969).
- [110] M. Cho, H. Bak, F. Fröhner, and K. Müller, “Total cross sections for kilovolt neutrons of even-odd nuclei in H.E. region of the 3s strength-function resonances,” *J. Korean Nucl. Soc.* **2**, 241 (1970).
- [111] K. Guber, “ORELA logbooks.” Private communication (2018).
- [112] C. Coceva, R. Simonini, and D. Olsen, “Calculation of hte ORELA neutron moderator spectrum and resolution function,” *Nucl. Inst. Meth.* **211**, 459 (1983).
- [113] M. Herman, R. Capote, B. V. Carlson, P. Obložinský, M. Sin, A. Trkov, H. Wienke, and V. Zerkin, “EMPIRE: Nuclear reaction model code system for data evaluation,” *Nucl. Data Sheets* **108**, 2655 (2007).
- [114] G. P. A. Nobre, D. A. Brown, M. W. Herman, and A. Golas, “Constraining level densities through quantitative correlations with cross-section data,” *Phys. Rev. C* **101**, 034608 (2020).
- [115] A. Gilbert and A. G. W. Cameron, “A composite nuclear-level density formula with shell corrections,” *Can. J. Phys.* **43**, 1446 (1965).
- [116] J. J. Griffin, “Statistical model of intermediate structure,” *Phys. Rev. Lett.* **17**, 478 (1966).
- [117] J. M. Akkermans, H. Gruppelaar, and G. Reffo, “Angular distributions in a unified model of preequilibrium and equilibrium neutron emission,” *Phys. Rev. C* **22**, 73 (1980).
- [118] R. Li, W. Sun, E. Soukhovitskii, J. Quesada, and R. Capote, “Dispersive coupled-channels optical-model potential with soft-rotator couplings for Cr, Fe, and Ni isotopes,” *Phys. Rev. C* **87**, 054611 (2013).
- [119] A. J. Koning and J. P. Delaroche, “Local and global nucleon optical models from 1 keV to 200 MeV,” *Nucl. Phys. A* **713**, 231 (2003).
- [120] V. Avrigeanu, P. E. Hodgson, and M. Avrigeanu, “Global optical potentials for emitted alpha particles,” *Phys. Rev. C* **49**, 2136 (1994).
- [121] H. An and C. Cai, “Global deuteron optical model potential for the energy range up to 183 MeV,” *Phys. Rev. C* **73**, 054605 (2006).
- [122] F. D. Becchetti and G. W. Greenlees, “Nucleon-Nucleus Optical-Model Parameters, $A < 40$, $E > 50$ MeV,”

- Phys. Rev. **182**, 1190 (1969).
- [123] T. Kawano and K. Shibata, "Covariance evaluation system," JAERI data/code, Japan Atomic Energy Research Institute, Tokai, Japan (1997).
- [124] D. Wilmore and P. Hodgson, "The calculation of neutron cross-sections from optical potentials," Nucl. Phys. **55**, 673 (1964).
- [125] P. T. Guenther, A. B. Smith, and J. F. Whalen, "The total, elastic and inelastic scattering fast neutron cross sections of natural chromium," Nucl. Sci. Eng. **82**, 408 (1982).
- [126] C. Thibault, "Study of fast (n,He3) in the (d,d) reaction, measurement of some total cross sections.," Tech. Rep. 3124 (1967). Centre d'Etudes Nucleaires, Saclay Reports.
- [127] A. I. Dyumin, D. M. Kaminker, G. N. Popova, and V. A. Smolin, "Total neutron cross sections for titanium, chromium, and copper isotopes," Izv. Rossiiskoi Akademii Nauk, Ser. Fiz. **36**, 852 (1972).
- [128] I. Korzh, V. Mishchenko, E. Mozhzhukhin, A. Golubova, N. Pravdivyi, I. Sanzhur, and M. Pasechnik, "Neutron scattering in energy range 1.5-3.0 MeV on the even isotopes of Cr, Ni, Zn," in *3.All Union Conf. on Neutron Phys., Kiev, 9-13 Jun 1975*, **4**, 220 (1975).
- [129] I. Korzh, V. Mishchenko, E. Mozhzhukhin, M. Pasechnik, N. Pravdivyi, and I. Sanzhur, "Study of Neutron Scattering in the Energy Region 1.5-3.0 MeV by Even-Even Isotopes of Cr," Yad. Fiz. **26**, 1151 (1977).
- [130] I. Korzh, V. Mishchenko, E. Mozhzhukhin, and N. Pravdivyi, "Investigation of scattering of fast neutrons on ^{52}Cr ," Yad. Fiz. **35**, 1097 (1982).
- [131] W. E. Kinney and F. G. Perey, "Natural chromium and ^{52}Cr neutron elastic and inelastic scattering cross sections from 4.07 to 8.56 MeV," Tech. Rep. ORNL-4806, Oak Ridge National Laboratory (1974).
- [132] A. B. Smith and D. Schmidt, "Neutron scattering and models: chromium," J. Phys. G: Nucl. Part. Phys. **23**, 197 (1997).
- [133] S. Malmkog, "Differential neutron elastic scattering cross sections for Cr, Fe and Ni in the energy range 500 to 1400 keV," internal report 25, Aktiebolaget Atomenergi, Stockholm (1972).
- [134] I. Korzh, V. Mishchenko, M. Pasechnik, N. Pravdivyi, I. Sanzhur, and I. Tockii, "Elastic scattering of 1.5 MeV neutrons by medium-atomic-weight nuclei," Ukrainian Phys. J. **12**, 1522 (1968).
- [135] B. Holmqvist, S. Johansson, G. Lodin, M. Salama, and T. Wiedling, "A neutron elastic scattering study of Chromium, Iron and Nickel in the energy region 1.77 to 2.76 MeV," Studsvik Repts. 385, Aktiebolaget Atomenergi, Stockholm (1970).
- [136] L. Kazakova, V. Kolesov, V. Popov, O. Salnikov, V. Sluchevskaja, and V. Trikova, "Elastic scattering of neutrons with initial energy 2 MeV," in *European-American Nucl. Data Committee Documents*, no. 50-S, 200 (1965).
- [137] M. Pasechnik, I. Korzh, I. Kashuba, V. Mishchenko, N. Pravdivyi, and I. Sanzhur, "Investigation of Elastic Scattering of Neutrons in the Energy Region 0.3-4.1 MeV by Ti and Cr Nuclei Using the Optical Model of the Nucleus," Yad. Fiz. **11**, 958 (1970).
- [138] B. Holmqvist, T. Wiedling, S. Johansson, G. Lodin, A. Kiss, B. Gustavsson, and B. Antolkovic, "Neutron elastic scattering cross sections experimental data and optical model cross section calculations," Studsvik Repts. 366, Aktiebolaget Atomenergi, Stockholm (1969).
- [139] L. Mihailescu, C. Borcea, A. Koning, and A. Plompen, "High resolution measurement of neutron inelastic scattering and (n,2n) cross-sections for ^{52}Cr ," Nucl. Phys. A **786**, 1 (2007).
- [140] P. T. Karatzas, G. P. Couchell, B. K. Barnes, L. E. Beghian, P. Harihar, A. Mittler, D. J. Pullen, E. Sheldon, and N. B. Sullivan, "Neutron inelastic scattering cross sections for natural chromium determined from the (n,n' γ) reaction," Nucl. Sci. Eng. **67**, 34 (1978).
- [141] F. Voss, S. Cierjacks, D. Erbe, and G. Scmalz, "Measurement of the gamma-ray production cross sections from inelastic neutron scattering in some chromium and nickel isotopes between 0.5 and 10 MeV," in *Conference on Nuclear Cross-Sections and Technology*, (Washington D.C., USA) (1975).
- [142] U. Abbondanno, R. Giacomich, M. Lagonegro, and G. Pauli, "Gamma rays resulting from nonelastic processes of 14.2 MeV neutrons with sodium, magnesium, silicon, sulphur, titanium, chromium and iron," J. Nucl. Energy **27**, 227 (1973).
- [143] A. Lashuk and I. Sadokhin, "Gamma-quanta production cross sections at neutron inelastic scattering at the energy 3 MeV," Vop. At.Nauki i Tekhn., Ser. Yadernye Konstanty, 59 (1996).
- [144] W. Breunlich, G. Stengl, and H. Vonach, "Bestimmung von (n,n' γ)-querschnitten für 14.4 meV-neutronen im massebereich a = 46-88," Z. fuer Naturforschung, Sect. A **26**, 451 (1971).
- [145] P. Obložinský, S. Hlaváč, G. Maino, and A. Mengoni, "Gamma-ray production from $^{52}\text{Cr}(n, x\gamma)$ reactions at 14.6 meV," Il Nuovo Cimento A (1965-1970) **105**, 965 (1992).
- [146] G. Tessler and S. Glickstein, "Gamma-ray production cross sections for neutron inelastic scattering from Cr, Ni, ^{92}Zr , and ^{94}Zr from 3 to 6 MeV," in *Conf. on Nucl. Cross-Sect. and Techn.*, **2**, (Washington), 934 (1975).
- [147] W. Mannhart, D. Schmidt, and D. L. Smith, "Measurement of the $^{52}\text{Cr}(n,p)^{52}\text{V}$, $^{52}\text{Cr}(n,2n)^{51}\text{Cr}$, $^{51}\text{V}(n,p)^{51}\text{Ti}$ and $^{51}\text{V}(n,\alpha)^{48}\text{Sc}$ cross sections between 7.9 and 14.4 MeV," in *Conference on Nuclear Data for Science and Technology*, **1**, (Trieste, Italy), 505 (1997).
- [148] D. M. Van Patter, N. Nath, S. M. Shafroth, S. S. Malik, and M. A. Rothman, "Gamma rays from inelastic neutron scattering in chromium," Phys. Rev. **128**, 1246 (1962).
- [149] M. Fedorov, T. Yakovenko, N. Surovitskaya, E. Korbet-skiy, and L. Sokolov, "Scattering of neutrons with 2.9 MeV energy on even-even isotopes of iron, chromium and zinc," **3**, 56 (1973). 2. Conf. on Neutron Physics, Kiev 1973.
- [150] S. Tagesen and P. Hille, "Competing gamma emission in the (N,2N) reaction on 24-Cr-52," Acta Phys. Austriaca **23**, 31 (1966).
- [151] A. Lychagin, S. Simakov, B. Devkin, B. Zhuravlev, M. Kobosev, O. Salnikov, V. Talalaev, and T. Sz-taricskai, "Neutron spectra from $^{52}\text{Cr}(N,N'\text{G})$ and $^{208}\text{Pb}(N,N'\text{G})$ reactions at an incident neutron energy of 14.1 MeV," in *Symp. on Nucleon Induced Reactions*, (Smolenice), 272 (1988).
- [152] Y. Kramarovskiy, Y. Nemilov, L. Pobedonostsev, and

- E. Teterin, "The excitation functions of neutron inelastic scattering for ^{52}Cr , ^{53}Cr and Al-27," *Vop. At.Nauki i Tekhn., Ser. Yadernye Konstanty*, 30 (1989).
- [153] D. Schmidt and W. Mannhart, "Differential cross sections of neutron scattering on elemental chromium at energies between 8.0 MeV and 14.8 MeV," *Tech. Rep. 31*, Physikalisch Technische Bundesanstalt (1998). *Phys. Techn. Bundesanst., Neutronenphysik Reports*.
- [154] N. Olsson, E. Ramstrom, and B. Trostell, "Neutron elastic and inelastic scattering from Mg, Si, S, Ca, Cr, Fe and Ni at $E(n) = 21.6$ MeV," *Nucl. Phys. A* **513**, 205 (1990).
- [155] Y. G. Degtyarev and V. N. Protopopov, "(n,n' γ) reactions on ^{27}Al , ^{51}V , ^{52}Cr , ^{55}Mn , ^{56}Fe , ^{93}Nb , ^{208}Pb , and ^{209}Bi : Gamma spectra and cross sections," *Izv. Rossiiskoi Akademii Nauk, Ser. Fiz.* **35**, 2341 (1971).
- [156] J. Degtjarev and V. Protopopov, "Excitation of Al-27, Cr-52, Fe-56 and Bi-209 low levels at inelastic scattering of 1-4 MeV neutrons," *Atomnaya Energiya* **23**, 568 (1967).
- [157] D. C. Larson and J. K. Dickens, " $^{53}\text{Cr}(n, n'\gamma)$ reactions and the level structure of ^{53}Cr ," *Phys. Rev. C* **39**, 1736 (1989).
- [158] N. Frenes, W. Hofmann, M. Uhl, and H. Warhanek, "Bestimmung des differentiellen wirkungsquerschnittes $d\sigma(e)/d\Omega$ / de der reaktion $^{52}\text{Cr}(n, \gamma)^{53}\text{Cr}$," *Acta Phys. Austr.* **40**, 365 (1974).
- [159] Y. Xia, Z. Yang, and Y. Zheng, "Measurement of neutron capture cross section of ^{50}Cr in the energy range from 50 to 1052 keV," *Tech. Rep. INDC(CPR)-059/L,P1* (2002).
- [160] M. Wagner, G. Winkler, H. Vonach, C. Buczko, and J. Csikai, "Measurement of the cross sections for the reactions $^{52}\text{Cr}(n,2n)^{51}\text{Cr}$, $^{66}\text{Zn}(n,2n)^{65}\text{Zn}$, $^{89}\text{Y}(n,2n)^{88}\text{Y}$ and $^{96}\text{Zr}(n,2n)^{95}\text{Zr}$ from 13.5 to 14.8 MeV," *Annals Nucl. Energy* **16**, 623 (1989).
- [161] W. Mannhart and D. Schmidt, "Measurement of neutron activation cross sections in the energy range from 8 MeV to 15 MeV," *Tech. Rep. 53*, Physikalisch Technische Bundesanstalt (2007). *Phys. Techn. Bundesanst., Neutronenphysik Reports*.
- [162] Zhou Feng-Qun, Yi Yan-Ling, Tuo Fei, Cao Xue-Xiang, and Kong Xiang-Zhong, "Measurement of cross sections for $^{50}\text{Cr}(n,2n)^{49}\text{Cr}$ and $^{52}\text{Cr}(n,2n)^{51}\text{Cr}$ reactions induced by 13.5-14.6 MeV neutrons," *High Energy Phys. Nucl. Physics, Chin. ed.* **29**, 644 (2005).
- [163] A. Fessler, E. Wattecamp, D. L. Smith, and S. M. Qaim, "Excitation functions of $(n, 2n)$, (n, p) , $(n, np + pn + d)$, and (n, α) reactions on isotopes of chromium," *Phys. Rev. C* **58**, 996 (1998).
- [164] N. I. Molla, R. U. Miah, S. Basunia, S. M. Hossain, and M. Rahman, "Excitation functions of (n, p) , (n, α) and $(n, 2n)$ processes on some isotopes of Cl, Cr, Ge, Mo and Ce in the energy range 13.57-14.71 MeV," in *Proc. Intern. on Nuclear Data for Science and Technology*, **1**, (Trieste), 517 (1997).
- [165] Y. Uno, Y. Uwamino, T. S. Soewarsono, and T. Nakamura, "Measurement of the neutron activation cross sections of ^{12}C , ^{30}Si , ^{47}Ti , ^{48}Ti , ^{52}Cr , ^{59}Co , and ^{58}Ni between 15 and 40 MeV," *Nucl. Sci. Eng.* **122**, 247 (1996).
- [166] S. Iwasaki, T. Win, S. Matsuyama, and N. Odano, "Measurement of $(n,2n)$ cross-sections for Sc, Mn, Cr and In between 12 and 19 MeV with activation technique (JAERI-Conf-97-005)," in *Proceedings of the 1996 Symposium on Nuclear Data*, 169 (1997).
- [167] A. Ercan, M. Erduran, M. Subasi, E. Gueltekin, G. Tarcan, A. Baykal, and M. Bostan, "14.6 MeV neutron induced reaction cross section measurements," in *Conf. on Nucl. Data for Sci. and Technol.*, 376 (1991).
- [168] H. Liskien, M. Uhl, M. Wagner, and G. Winkler, "The excitation function for the reaction $^{52}\text{Cr}(n,2n)^{51}\text{Cr}$," Private communication (1989).
- [169] E. M. Zsolnay, R. Capote, H. Nolthenius, and A. Trkov, "Summary description of the new international reactor dosimetry and fusion file (IRDFF release 1.0)," *Tech. Rep. INDC(NDS)-0616*, IAEA, Vienna (2012).
- [170] R. Capote, K. I. Zolotarev, V. G. Pronyaev, and A. Trkov, "Updating and extending the IRDF-2002 dosimetry library," *J. ASTM Int.* **9** (2012).
- [171] C. Fu, "Symp. on neutron cross sections from 10 to 50 MeV," BNL report BNL-NCS-51425, p.675, Brookhaven National Laboratory (1980).
- [172] C. Y. Fu, "A Consistent Nuclear Model for Compound and Precompound Reactions with Conservation of Angular Momentum," *Tech. Rep. ORNL/TM-7042*, Oak Ridge National Laboratory (1980).
- [173] C. Fu, "Approximation of precompound effects in Hauser-Feshbach codes for calculating double differential (n, xn) cross sections," *Nucl. Sci. Eng.* **100**, 61 (1988).
- [174] K. Shibata and C. Fu, "Recent improvements of the TNG statistical model code," *Tech. Rep. ORNL/TM-10093*, Oak Ridge National Laboratory (1986).
- [175] D. L. Smith and J. W. Meadows, "Cross-section measurement for the $^{52}\text{Cr}(n,p)^{52}\text{V}$ reaction near threshold," *Nucl. Sci. Eng.* **76**, 43 (1980).
- [176] J. P. Gupta, H. D. Bhardwaj, and R. Prasad, "Pre-equilibrium emission effect in (n, p) reaction cross-sections at 14.8 MeV," *Pramana* **24**, 637 (1985).
- [177] O. I. Artem'ev, I. V. Kazachevskii, V. N. Levkovskii, V. L. Poznyak, and V. F. Reutov, "Cross sections for (n, p) and (n, α) reactions on chromium, iron, copper, and molybdenum nuclei at a neutron energy of 14.8 MeV," *Sov. At. Energy* **49**, 655 (1980).
- [178] N. Molla and S. Qaim, "A systematic study of (n, p) reactions at 14.7 MeV," *Nucl. Phys. A* **283**, 269 (1977).
- [179] W. Mannhart and D. Schmidt, "Measurement of Neutron Activation Cross Sections in the Energy Range from 8 MeV to 15 MeV," *Tech. Rep. Neutronenphysik Reports*, No.53, Physikalisch-Technische Bundesanstalt (2007).
- [180] B. Lalremruata, N. Otuka, G. J. Tambave, V. K. Mulik, B. J. Patil, S. D. Dhole, A. Saxena, S. Ganesan, and V. N. Bhoraskar, "Systematic study of (n,p) reaction cross sections from the reaction threshold to 20 MeV," *Phys. Rev. C* **85**, 024624 (2012).
- [181] T. D. Thiep, N. V. Do, T. T. An, and N. N. Son, "Nuclear reactions with 14 MeV neutrons and bremsstrahlungs in giant dipole resonance (GDR) region using small accelerators," *Nucl. Phys. A* **722**, C568 (2003).
- [182] Y. Kasugai, H. Yamamoto, K. Kawade, and T. Iida, "Measurement of (n,p) cross-sections for shortlived products by 13.4-14.9 MeV neutrons," *Annals Nucl. Energy* **25**, 23 (1998).
- [183] K. T. Osman and F. I. Habbani, "Measurement and Study of (n,p) Reaction Cross-sections for Cr, Ti, Ni, Co, Zr and Mo Isotopes using 14.7 MeV Neutrons," *tech.*

- rep., University of Khartoum (1996). Sudanese report to the I.N.D.C., No.001 (1996).
- [184] M. Viennot, M. Berrada, G. Paic, and S. Joly, "Cross-section measurements of (n,p) and (n,np+pn+d) reactions for some titanium, chromium, iron, cobalt, nickel, and zinc isotopes around 14 MeV," *Nucl. Sci. Eng.* **108**, 289 (1991).
- [185] A. Ercan, M. N. Erduran, M. Subasi, E. Gueltekin, G. Tarcan, A. Baykal, and M. Bostan, "14.6 MeV neutron induced reaction cross section measurements," in *Conference on Nuclear Data for Science and Technology*, (Juelich, Germany), 376 (1991).
- [186] G. R. Pansare, P. M. Dighe, and V. N. Bhoraskar, "Cross-sections of a few (n, α) and (n, p) reactions induced at 14.7 MeV neutrons," *Pramana* **37**, 425 (1991).
- [187] D. L. Smith, J. W. Meadows, and F. F. Porta, "Measurement of the $^{53}\text{Cr}(n, p)^{53}\text{V}$ cross section below 9.4 meV using a sample transport facility," *Nucl. Sci. Eng.* **78**, 420 (1981).
- [188] B. Anders, B. Bahal, and R. Pepelnik, "Measurements of 14 MeV neutron activation cross section at KORONA," *Tech. Rep. 85-E-24, Ges.Kernen.-Verwertung, Schiffbau and Schiffahrt* (1985).
- [189] H. D. Luc, P. N. Ngoc, N. V. Do, and L. B. Bach, "Determination of some (n,p),(n,np) and (n,alpha) reaction cross sections induced by 14.8 MeV neutrons on Cr and Ti isotopes," Vietnam report to the I.N.D.C. 5, INDC (1986).
- [190] L. Klochkova, B. Kovrigin, and V. Kuritsyn *Yadernye Konstanty* **1992**, 27 (1992).
- [191] I. Ribanský, T. Panteleev, and L. Stoeva, "Neutron activation cross-sections for Cr isotopes at 14.6 meV neutron energy," *Annals Nucl. Energy* **12**, 577 (1985).
- [192] B. Bahal and R. Pepelnik, "Cross section measurements of Cr,Mn,Fe,Co,Ni for an accurate determination of these elements in natural and synthetic samples using a 14 MeV neutron generator," *Tech. Rep. 85-E-11, Ges.Kernen.-Verwertung, Schiffbau and Schiffahrt* (1985).
- [193] N. I. Molla and S. M. Qaim, "A systematic study of (n,p) reactions at 14.7 MeV," *Nucl. Phys. A* **283**, 269 (1977).
- [194] M. Valkonen, P. Homberg, R. Rieppo, J. Keinaenen, and J. Kantele, "Studies of 14 MeV neutron activation cross sections with special reference to the capture reaction," *Dept.of Physics Reports 1/1976, Univ. of Jyvaeskylae* (1976).
- [195] L. Husain and P. Kuroda, "14.8 MeV neutron activation cross sections for chromium," *J. Inorg. Nucl. Chem.* **29**, 2665 (1967).
- [196] A. Takahashi, E. Ichimura, Y. Sasaki, and H. Sugimoto, "Double-differential and angle integrated emission spectra at 14.1 MeV for beryllium and natural chromium," *Tech. Rep. 87-03, Osaka University* (1992).
- [197] I. FUJITA, M. SONODA, A. KATASE, Y. WAKUTA, H. TAWARA, M. HYAKUTAKE, and K. IWATANI, "Inelastic scattering of 14meV neutrons by medium weight nuclei," *J. Nucl. Sci. Technol.* **9**, 301 (1972).
- [198] D. Schmidt, W. Mannhart, and B. R. L. Siebert, "Measurement of Elastic, Inelastic and Double-Differential Neutron Scattering Cross Sections on V, Cr and Pb at Energies between 8 MeV and 15 MeV," in *Conference on Nuclear Data for Science and Technology*, **1**, (Trieste, Italy), 407 (1997).
- [199] H. Vonach, A. Chalupka, F. Wenninger, and G. Staffel, "Measurement of the angle-integrated secondary neutron spectra from interaction of 14 MeV neutrons with medium and heavy nuclei," U.S. report to the I.N.D.C. 84, INDC (1980).
- [200] C. Kalbach and F. M. Mann, "Phenomenology of continuum angular distributions. I. Systematics and parametrization," *Phys. Rev. C* **23**, 112 (1981).
- [201] S. Matsuyama, T. Okubo, M. Baba, T. Ito, T. Akiyama, N. Ito, and N. Hirakawa, "Measurement of double-differential neutron emission cross sections of Mo, Ta and W," *Tech. Rep. 93-046, Japan Atomic Energy Research Institute* (1992).
- [202] G. Morgan and E. Newman, "The $\text{cr}(n,x\text{ gamma})$ reaction cross section for incident neutron energies between 0.2 and 20.0 meV," technical memo 5098, Oak Ridge National Laboratory (1976).
- [203] D. M. Drake, E. D. Arthur, and M. G. Silbert, "Cross Sections for Gamma-Ray Production by 14-MeV Neutrons," *Nucl. Sci. Eng.* **65**, 49 (1978).
- [204] R. Lell and R. McKnight, "Argonne data testing of new evaluations for ENDF/B," (Santa Fe, NM, USA) (2010). Cross Section Evaluation Working Group Meeting.
- [205] J. Dyrda, N. Soppera, and I. Hill, "Nuclear Data Sensitivity Tool (NDaST)," Nuclear Energy Agency, OECD, Paris, France (2020), [Online] Available at https://www.oecd-nea.org/jcms/pl_32450/nuclear-data-sensitivity-tool-ndast.
- [206] "INDEN - International Network of Nuclear Data Evaluators." International Atomic Energy Agency, Vienna, Austria, [Online] Available at <https://www.nds.iaea.org/INDEN/>.
- [207] Sub Working Group of Fusion Reactor Physics Subcommittee, "Fusion reactor physics subcommittee, collection of experimental data for fusion neutronics benchmark," *Tech. Rep. JAERI-M 94-014, Japan Atomic Energy Research Institute* (1994).
- [208] Y. Makita, A. Takahashi, and Y. Oyama, "Compilation of benchmark results for fusion related nuclear data," *Tech. Rep. KAERI 98-024, Korea Atomic Energy Research Institute* (1998).
- [209] A. Milocco, A. Trkov, and I. Kodeli, "The OKTAVIAN TOF experiments in SINBAD: Evaluation of the experimental uncertainties," *Annals Nucl. Energy* **37**, 443 (2010).
- [210] "The PETALE experimental programme." EPFL, Switzerland, [Online] Available at <https://www.epfl.ch/labs/lrs/research-programs/experimental-eng/petale-eng/>.
- [211] L. Templin(editor), "Reactor physics constants," *Tech. Rep. 5800, Argonne National Laboratory* (1963).
- [212] A. Negret, M. Sin, C. Borcea, R. Capote, P. Dessagne, M. Kerveno, N. Nankov, A. Olacel, A. J. M. Plompen, and C. Rouki, "Cross-section measurements for the $^{57}\text{Fe}(n, n\gamma)^{57}\text{Fe}$ and $^{57}\text{Fe}(n, 2n\gamma)^{56}\text{Fe}$ reactions," *Phys. Rev. C* **96**, 024620 (2017).
- [213] M.-L. Mauborgne, R. Radtke, C. Stoller, and F. Haranger, "Impact of the ENDF/B-VIII.0 library on modeling nuclear tools for oil exploration," *EPJ Web Conf.* **239**, 20007 (2020).